

ABSTRACT

Title of dissertation: THE SEARCH FOR
SUPERMASSIVE BLACK HOLE BINARIES
IN THE TIME DOMAIN

Tingting Liu
Doctor of Philosophy, 2018

Dissertation directed by: Professor Suvi Gezari
Department of Astronomy

Supermassive black hole binaries (SMBHBs) are expected due to galaxy mergers and the ubiquity of central supermassive black holes (SMBHs) in galaxies, but direct evidence for close-separation SMBHBs has been elusive. This thesis presents my search for SMBHBs in the optical time domain, *i.e.* by searching for their optical variability signatures. It is a novel approach that can potentially yield SMBHBs in close, sub-pc orbits, a population of SMBH pairs or binaries that can not be directly imaged or resolved by current telescopes or techniques. Further, searches in the optical time domain are sensitive to SMBHBs in the low-frequency gravitational wave-emitting regime, opening up the possibility of studying them in the era of multi-messenger astronomy.

I developed a custom pipeline to systematically search in the Pan-STARRS1 Medium Deep Survey (PS1 MDS) for periodically varying quasars, which have been predicted as the manifestations of SMBHBs at close separations. I constructed a spectroscopically-complete sample of SMBHB candidates using observations with

the Gemini Telescope or the Discovery Channel Telescope and measured their black hole masses and redshifts. I also followed up the candidates with a dedicated monitoring program on the Las Cumbres Observatory telescopes, in order to put their periodicity to the test and identify false positives that are due to the stochastic variability of regular quasars that do not host SMBHBs. I set up the expectations for a true periodic signal by modeling normal quasar variability and showed that evidence for a true signal should strengthen over a longer temporal baseline. I then used the expectations as a guide and applied a range of statistical criteria to select more robust candidates from PS1 MDS. From this down-selected sample, I was able to determine an upper limit on the SMBHB rate. I also discussed the search for SMBHBs in the era of the Large Synoptic Survey Telescope and SMBHB candidates as possible gravitational wave sources for the pulsar timing arrays.

THE SEARCH FOR SUPERMASSIVE BLACK HOLE BINARIES IN THE TIME DOMAIN

by

Tingting Liu

Dissertation submitted to the Faculty of the Graduate School of the
University of Maryland, College Park in partial fulfillment
of the requirements for the degree of
Doctor of Philosophy
2018

Advisory Committee:

Professor Suvi Gezari, Chair/Advisor

Professor M. Coleman Miller

Professor Richard Mushotzky

Professor Scott C. Noble

Professor Peter Shawhan, Dean's Representative

© Copyright by
Tingting Liu
2018

Preface

Chapter 2 is published as Liu, T. et al. 2015, The Astrophysical Journal Letters, 803, L16;

Chapter 3 is published as Liu, T. et al. 2016, The Astrophysical Journal, 833, 6;

Chapter 4 is published as Liu, T., Gezari, S., & Miller, M.C. 2018, The Astrophysical Journal Letters, 859, L12; and

Chapter 5 is to be submitted as “Supermassive Black Hole Binary Candidates from the Pan-STARRS1 Medium Deep Survey” to The Astrophysical Journal.

Acknowledgments

I owe my gratitude first and foremost to Dr. Suvi Gezari, who has supervised my thesis research.

I have also had the honor and pleasure to work with Dr. Cole Miller on the work presented in Chapter 4.

I am also grateful to the other members of my thesis committee, Dr. Richard Mushotzky, Dr. Scott Noble, and Dr. Peter Shawhan; I could not have assembled a better committee.

The work presented in this thesis made extensive use of the following observing facilities: the Panoramic Survey Telescope and Rapid Response System (Pan-STARRS), operated by the Institute for Astronomy, the University of Hawaii; the Gemini Telescope and Las Cumbres Observatory telescopes, through the National Optical Astronomy Observatory; and the Discovery Channel Telescope at the Lowell Observatory. This thesis research was partially supported by the National Science Foundation.

Table of Contents

| | |
|---|-----|
| Preface | ii |
| Acknowledgements | iii |
| List of Tables | vii |
| List of Figures | ix |
| List of Abbreviations | xi |
| 1 Introduction | 1 |
| 1.1 Supermassive Black Hole Binaries | 1 |
| 1.1.1 SMBHBs as the Products of Galaxy Mergers | 1 |
| 1.1.2 Dual AGNs and the Spectroscopic Search for Close-Separation SMBHBs | 3 |
| 1.1.3 The SMBHB Candidate OJ 287 | 8 |
| 1.1.4 SMBHBs as the Sirens of Low-frequency Gravitational Waves | 10 |
| 1.2 Theoretically Predicted Variability Signatures of an SMBHB | 13 |
| 1.2.1 Modulated Mass Accretion as the Cause of Periodicity | 13 |
| 1.2.2 Doppler Boosting as the Cause of Periodicity | 17 |
| 1.3 The Search for SMBHBs | 18 |
| 1.3.1 The Detectability of SMBHBs in a Time Domain Survey | 18 |
| 1.3.2 Systematically Searching for Periodically Varying Quasars | 20 |
| 1.4 Quasar Variability and the Challenges of Searching for Periodic Quasars | 24 |
| 1.4.1 Optical Variability of Quasars | 24 |
| 1.4.2 Red Noise Contamination of the SMBHB Candidate Sample | 28 |
| 2 A Periodically Varying Luminous Quasar at $z = 2$ from the Pan-STARRS1 Medium Deep Survey: A Candidate Supermassive Black Hole Binary in the Gravitational Wave-Driven Regime | 33 |
| 2.1 Introduction | 33 |
| 2.2 Theoretical Predictions | 36 |
| 2.3 Pan-STARRS1 Medium Deep Survey | 37 |

| | | |
|-------|--|-----|
| 2.4 | Ensemble Photometry | 37 |
| 2.5 | Selecting Periodic Quasar Candidates | 39 |
| 2.6 | Periodic Quasar Candidate PSO J334.2028+01.4075 | 40 |
| 2.7 | Physical Interpretation | 42 |
| 2.8 | Discussion and Conclusions | 43 |
| 3 | A Systematic Search for Periodically Varying Quasars in Pan-STARRS1: An Extended Baseline Test in Medium Deep Survey Field MD09 | 49 |
| 3.1 | Introduction | 49 |
| 3.2 | The Pan-STARRS1 Medium Deep Survey | 53 |
| 3.3 | Methods | 55 |
| 3.3.1 | Sample Selection | 55 |
| 3.3.2 | Variability Selection | 58 |
| 3.3.3 | Selection Bias | 60 |
| 3.3.4 | Selecting Periodic Quasar Candidates | 63 |
| 3.4 | Extended Baseline Photometry | 65 |
| 3.4.1 | Follow-up Imaging | 67 |
| 3.4.2 | Pre-PS1 Archival Photometry | 69 |
| 3.4.3 | Testing the Persistence of Periodicity with Extended Baseline Photometry | 70 |
| 3.5 | Black Hole Mass Estimates and Inferred Binary Parameters | 72 |
| 3.6 | Summary and Conclusions | 75 |
| 4 | Did ASAS-SN Kill the Supermassive Black Hole Binary Candidate PG 1302–102? | 93 |
| 4.1 | Introduction | 93 |
| 4.2 | Extended Light Curve from ASAS-SN | 95 |
| 4.3 | Expectations for a True Periodic Signal | 97 |
| 4.4 | Extended Baseline Analyses of PG 1302 | 100 |
| 4.5 | Conclusions | 103 |
| 5 | Supermassive Black Hole Binary Candidates from the Pan-STARRS1 Medium Deep Survey | 110 |
| 5.1 | Introduction | 110 |
| 5.2 | The Pan-STARRS1 Medium Deep Survey | 114 |
| 5.3 | Methods | 115 |
| 5.3.1 | Quasar and Variability Selection | 115 |
| 5.3.2 | Searching for Periodicity | 118 |
| 5.4 | Results | 118 |
| 5.4.1 | Periodic Quasar Candidates from MDS | 118 |
| 5.4.2 | Spectroscopy and Black Hole Mass | 120 |
| 5.5 | Extended Baseline Photometry | 125 |
| 5.6 | Reevaluating Periodic Candidates Using a Maximum Likelihood Method | 129 |
| 5.7 | Discussion | 149 |
| 5.7.1 | The Detection Rate of SMBHBs | 149 |

| | | |
|-------|--|-----|
| 5.7.2 | Implications for Gravitational Wave Astrophysics in the PTA Regime | 152 |
| 5.7.3 | Periodic Quasar Detections in the LSST Era | 153 |
| 5.7.4 | Probing the SED Properties of SMBHBs | 157 |
| 5.8 | Summary and Conclusions | 158 |
| 6 | Conclusions and Future Work | 182 |
| 6.1 | What Would be a Convincing Detection of Periodicity? | 183 |
| 6.2 | Can We Find Robust Periodic Candidates with Extended-baseline Imaging? | 185 |
| 6.3 | Can We Search for Evidence for Periodicity in the X-rays? | 187 |
| 6.4 | Can We Search for Complementary Evidence for an SMBHB? | 189 |
| | Bibliography | 198 |

List of Tables

| | | |
|------|---|-----|
| 1.1 | Summary of Systematic Searches for Periodically Varying Quasars . . | 24 |
| 3.1 | PS1 Quality Flags Used in the Query | 58 |
| 3.2 | QLF Model Values Used | 60 |
| 3.3 | MD09 by the Numbers | 66 |
| 3.4 | PS1 Mean Magnitudes and Variability Amplitudes of Periodic Quasar Candidates | 66 |
| 3.5 | Extended Baseline Photometry of Periodic Quasar Candidates | 87 |
| 3.6 | SDSS to PS1 Filter Offsets from Synthetic Quasar Magnitudes | 88 |
| 3.7 | Detected Periods and Significance Factors of Periodogram-selected Candidates | 89 |
| 3.8 | Spectroscopic Information and Inferred Binary Parameters of Peri- odic Quasar Candidates | 90 |
| 4.1 | Maximum Likelihoods for the Simulated DRW+periodic Light Curve | 107 |
| 4.2 | Damped Random Walk Parameter Ranges Sampled by MCMC | 108 |
| 4.3 | Broken Power-law Parameter Ranges Sampled by MCMC | 109 |
| 5.1 | Medium Deep Field Centers | 116 |
| 5.2 | Medium Deep Fields by the Numbers (MD01-MD02) | 131 |
| 5.3 | Medium Deep Fields by the Numbers (MD03-MD04) | 132 |
| 5.4 | Medium Deep Fields by the Numbers (MD05-MD06) | 133 |
| 5.5 | Medium Deep Fields by the Numbers (MD07-MD08) | 134 |
| 5.6 | Medium Deep Fields by the Numbers (MD09-MD10) | 135 |
| 5.7 | Period, Significance Factors, and Number of Cycles of Periodic Can- didates (MD01-MD04) | 136 |
| 5.8 | Period, Significance Factors, and Number of Cycles of Periodic Can- didates (MD05-MD10) | 137 |
| 5.9 | PS1 Mean Magnitudes and Variability Amplitudes of Periodic Quasar Candidates (MD01-05) | 138 |
| 5.10 | PS1 Mean Magnitudes and Variability Amplitudes of Periodic Quasar Candidates (MD06-10) | 139 |
| 5.11 | Spectroscopic Follow-ups | 140 |

| | |
|--|-----|
| 5.12 Spectroscopic Measurements and Inferred Binary Parameters (MD01-04) | 141 |
| 5.13 Spectroscopic Measurements and Inferred Binary Parameters (MD05-10) | 142 |
| 5.14 Extended Baseline Monitoring of Candidates (MD01-MD04) | 145 |
| 5.15 Extended Baseline Monitoring of Candidates (MD05-MD10) | 146 |
| 5.16 Re-analyses Using the Maximum Likelihood Method under the DRW Model (MD01-MD04) | 147 |
| 5.17 Re-analyses Using the Maximum Likelihood Method under the DRW Model (MD05-MD10) | 148 |
| 5.18 Re-analyses Using the Maximum Likelihood Method under the BPL Model (MD01-MD04) | 160 |
| 5.19 Re-analyses Using the Maximum Likelihood Method under the BPL Model (MD05-MD10) | 161 |
| 5.20 Comparing PS1 MDS and LSST Capabilities | 163 |
| 5.21 Parameters Used in Figure 5.15 | 165 |
| 5.22 The SED of PSO J185 | 167 |

List of Figures

| | | |
|------|---|-----|
| 1.1 | The VLBA image of CSO 0402+379 | 6 |
| 1.2 | The V-band Light Curve and the Binary Model of OJ 287 | 10 |
| 1.3 | Simulations of a Binary-Disk System | 15 |
| 1.4 | The \dot{M} Variation as a Function of Time | 16 |
| 1.5 | The Detectability of SMBHBs as Periodic Quasars in a Time Domain Survey | 19 |
| 1.6 | The Light Curve of the SMBHB Candidate PG 1302–102. | 22 |
| 1.7 | Light Curves Simulated From the Damped Random Walk Model | 27 |
| 2.1 | Color–Color Diagrams Used to Select Point Sources in MD09 | 45 |
| 2.2 | Sinusoidal Fit to the PS1 Light Curves of PSO J334.2028+01.4075 . . | 46 |
| 2.3 | LS Periodogram of PSO J334.2028+01.4075 | 47 |
| 2.4 | The Archival CRTS Light Curve of PSO J334.2028+01.4075 | 48 |
| 3.1 | Comparing the Light Curves of the Periodic Quasar Candidate PSO J334.2028+1.4075 From PV1 and PV2. | 78 |
| 3.2 | Color Diagrams of Cross-matched Stars and Quasars | 79 |
| 3.3 | The Observed Scatter of the Light Curve as a Function of Magnitude | 80 |
| 3.4 | Magnitude Error vs. Magnitude in the g_{P1} Filter | 81 |
| 3.5 | The Number Fraction of Our MD09 Quasars that Vary at the $> \sigma_{\text{int}}$ Level | 82 |
| 3.6 | The g_{P1} Band Apparent Magnitude Distribution of Our MD09 Quasar Sample | 83 |
| 3.7 | Selection Bias | 84 |
| 3.8 | The LS Periodograms of PS1 MD09 Candidates | 85 |
| 3.9 | The Light Curves of PS1 MD09 Candidates | 86 |
| 3.10 | Spectra of PS1 MD9 Candidates | 91 |
| 3.11 | Comparing with the Periodic Candidates from Graham et al. (2015b) and Charisi et al. (2016) | 92 |
| 4.1 | Combined Light Curve of PG 1302-102 | 105 |
| 4.2 | A Simulated DRW+periodic Light Curve | 106 |

| | | |
|------|---|-----|
| 5.1 | The Number of Detections for a Random Sample of $\sim 27,000$ Objects in MDS | 115 |
| 5.2 | The Color Diagram of Quasars in PS1 MDS | 117 |
| 5.3 | The Mean g Band Magnitude Distribution of Periodic Candidates | 119 |
| 5.4 | The Distribution of the Observed Periods | 120 |
| 5.5 | The Variability Amplitudes of Candidates | 121 |
| 5.6 | The Distribution of the Rest-frame Periods | 124 |
| 5.7 | The Black Hole Mass Distribution of Candidates | 125 |
| 5.8 | The Redshift Distribution of Candidates | 126 |
| 5.9 | The Parameter Space Probed by PS1 MDS and LSST | 143 |
| 5.10 | The Number of Cycles | 144 |
| 5.11 | The Magnitude Distribution of Candidates | 150 |
| 5.12 | The Cumulative Number of SMBHB Candidates | 162 |
| 5.13 | Gravitational Wave Strain Amplitudes of SMBHB Candidates | 163 |
| 5.14 | Detection Capabilities of the LSST | 164 |
| 5.15 | GW Frequencies and Strain Amplitudes Explored by the LSST | 166 |
| 5.16 | The SED of PSO J185 | 168 |
| 5.17 | The PS1-only and Extended Light Curve of PSO J185 | 169 |
| 5.18 | The SDSS Spectrum of PSO J185 | 170 |
| 5.19 | The LS Periodogram of PSO J185 | 170 |
| 5.20 | The PS1-only and Extended Light Curves of Periodic Candidates from PS1 MDS | 171 |
| 5.21 | Figure 5.20 Continued | 172 |
| 5.22 | Figure 5.21 Continued | 173 |
| 5.23 | Figure 5.22 Continued | 174 |
| 5.24 | Figure 5.23 Continued | 175 |
| 5.25 | Figure 5.24 Continued | 176 |
| 5.26 | Figure 5.25 Continued | 177 |
| 5.27 | SDSS Spectra of PS1 MDS Candidates | 178 |
| 5.28 | Figure 5.27 Continued | 179 |
| 5.29 | Figure 5.28 Continued | 180 |
| 5.30 | Figure 5.29 Continued | 181 |

List of Abbreviations

| | |
|---------|--|
| ACS | the Advanced Camera for Surveys |
| AGN | active galactic nucleus/nuclei |
| AIC | Akaike information criterion |
| ASAS-SN | All-sky Automated Survey for Supernovae |
| BAT | Burst Alert Telescope |
| BPL | broken power-law |
| CFHT | Canada-France-Hawaii Telescope |
| CRTS | Catalina Real-time Transient Survey |
| CSO | compact symmetric object |
| CSS | Catalina Sky Survey |
| CW | continuous wave |
| DCT | Discovery Channel Telescope |
| DRW | damped random walk |
| EM | electromagnetic |
| EPTA | European Pulsar Timing Array |
| FOV | field of view |
| FWHM | full-width at half-maximum |
| GALEX | Galaxy Evolution Explorer |
| GR | general relativity |
| GW | gravitational wave |
| GWB | gravitational wave background |
| HST | Hubble Space Telescope |
| IfA | Institute for Astronomy |
| IPP | Image Processing Pipeline |
| IPTA | International Pulsar Timing Array |
| iPTF | Intermediate Palomar Transient Factory |
| LCO | Las Cumbres Observatory |
| LEDE | luminosity evolution and density evolution |
| LINEAR | Lincoln Near-Earth Asteroid Research |
| LISA | Laser Interferometer Space Antenna |

| | |
|------------|--|
| LMI | Large Monolithic Imager |
| LS | Lomb-Scargle |
| LSST | Large Synoptic Survey Telescope |
| MCMC | Markov Chain Monte Carlo |
| MDS | Medium Deep Survey |
| MHD | magnetohydrodynamic |
| MJD | Modified Julian Date |
| MSP | millisecond pulsar |
| NANOGrav | North American Nanohertz Observatory for Gravitational Waves |
| NuSTAR | Nuclear Spectroscopic Telescope Array |
| Pan-STARRS | Panoramic Survey Telescope and Rapid Response System |
| PLE | pure luminosity evolution |
| PPTA | Parkes Pulsar Timing Array |
| PSD | power spectral density |
| PSF | point spread function |
| PSI | Pan-STARRS Science Interface |
| PTA | pulsar timing array |
| PTF | Palomar Transient Factory |
| PV1 | Processing Version 1 |
| QLF | quasar luminosity function |
| SDSS | Sloan Digital Sky Survey |
| SED | spectral energy distribution |
| SF | Structure Function |
| SKA | Square Kilometre Array |
| SMBH | supermassive black hole |
| SMBHB | supermassive black hole binary |
| SVM | support vector machine |
| TOA | time of arrival |
| ULIRG | ultraluminous infrared galaxy |
| UV | ultraviolet |
| VLBA | Very Long Baseline Array |
| VLBI | very long baseline interferometry |

XRT X-ray Telescope

ZTF Zwicky Transient Facility

Chapter 1: Introduction

1.1 Supermassive Black Hole Binaries

1.1.1 SMBHBs as the Products of Galaxy Mergers

Supermassive black holes (SMBHs) with masses between $10^6 - 10^9 M_\odot$ appear to be ubiquitous in the center of massive galaxies (*e.g.* reviews by [Ferrarese & Ford 2005](#); [Kormendy & Ho 2013](#); [Kormendy & Richstone 1995](#)). Their masses are tightly correlated with host galaxy properties such as the stellar velocity dispersion of the bulge, bulge luminosity, and bulge stellar mass, suggesting that the evolution of the SMBHs is closely linked to that of the galaxies (*e.g.* [Gültekin et al. 2009](#); [McConnell & Ma 2013](#)).

In the paradigm of structure formation in the standard Λ CDM cosmology (*e.g.* [White & Rees 1978](#)), galaxies merge with each other and grow into larger units. During the merger of galaxies, the SMBHs are expected to settle to the center of the newly-merged system, eventually forming a supermassive black hole binary (SMBHB) ([Begelman et al., 1980](#)). This process is first driven by dynamical friction, which efficiently drags the SMBHs to the center of the merger remnant on a timescale of $\sim 10^8$ years. After dynamical friction becomes inefficient at \sim parsec

(pc) scales, the SMBHs can further lose energy and angular momentum through three-body interaction with stars in the so-called “loss cone”: the star encountering the SMBHs is “slingshot” out of the system, carrying an amount of energy with it. The decrease in the semimajor axis of the SMBHs is a function of the velocity dispersion and the density of the isotropic background of stars and a hardening rate, and therefore this process is efficient for a fixed stellar background.

However, the loss cone is gradually depleted of stars, but the binary separation is still ~ 100 times larger than the separation where gravitational wave (GW) radiation can take over so that the binary coalesces within a Hubble time (the age of the Universe). Without replenishment of the loss cone, or other mechanisms, the binary will forever stall at a \sim parsec separation. This gives rise to the “final parsec problem” (Milosavljević & Merritt, 2003) and is most severe in spherical galaxies. However, recent N-body simulations show that in non-spherical galaxies (especially triaxial galaxies), there is a larger phase space of stellar orbits which can keep the loss cone filled, so that the timescale of the stellar hardening stage can be comfortably less than \sim Gigayear (Gyr) (*e.g.* Vasiliev et al. 2015). The final parsec problem as the barrier to SMBHB formation therefore can be alleviated.

After forming a close orbit ($a < 0.1$ pc), the SMBHs are now embedded in a circumbinary gas disk. The evolution of the binary is in two phases: at larger separations, the binary exchanges angular momentum with the disk through the accretion of mass and gravitational torques (*e.g.* Tang et al. 2017); at close enough separations (centi to milli-parsec scales), GW emission dominates the orbital decay, which rapidly drives the binary to coalesce. It is at this stage that the electromag-

netic variability signatures have been theoretically predicted (they are summarized in Section 1.2), signatures for which this thesis is dedicated to searching.

1.1.2 Dual AGNs and the Spectroscopic Search for Close-Separation SMBHBs

Observational evidence for the galaxy merger scenario described above is pairs of SMBHs not yet gravitationally bound to each other. These SMBHs at \sim kpc separations are called dual SMBHs and are progenitors of SMBHBs. If gas is funneled to the center of the galaxy merger remnant in a gas-rich merger and actively accreted by the black hole(s), the dual SMBHs would appear as offset or dual active galactic nuclei (AGNs). In the local universe, the two active nuclei separated by \sim kpc can be imaged directly. A prototype of such systems is the ultraluminous infrared galaxy (ULIRG) NGC 6240. It shows two nuclei separated by $1''.8$ (640 pc) with an unusual, disturbed morphology (*e.g.* Fried & Schulz 1983), and high spatial resolution X-ray imaging with *Chandra* indicates that both nuclei are AGNs (rather than star-forming or starburst regions) (Komossa et al., 2003).

However, while more kpc-separation dual AGNs have been uncovered serendipitously (*e.g.* Comerford et al. 2009a) or via hard X-ray imaging (*e.g.* Koss et al. 2011), identifying dual AGNs in large numbers remained difficult, and a new and systematic approach was proposed to identify more candidates: if both SMBHs are active as AGNs, the galaxy spectrum should display two sets of narrow emission lines (*e.g.* [OIII]) that are offset from the stellar absorption lines of the host galaxy

by a few hundred km s^{-1} (Comerford et al., 2009b). This technique has been applied to search for dual AGNs in the DEEP2 Galaxy Redshift Survey (Comerford et al., 2009b) and the Sloan Digital Sky Survey (SDSS) (Liu et al., 2010; Smith et al., 2010; Wang et al., 2009), and it has provided a larger sample of candidates for follow-up studies.

For example, integral-field spectroscopy of one of the Type-1 AGNs with double-peaked [OIII] profiles from the Smith et al. (2010) sample, SDSS J150243.1+111557 (hereafter SDSS J1502), shows that the lines are separated by 657 km s^{-1} , and high spatial resolution adaptive optics observations in the near-IR indicate that it has two nuclei separated by 7.4 kpc (Fu et al., 2012). The object was later resolved by the Expanded Very Large Array (Fu et al., 2011) into two radio components: a primary “J1502P” and a secondary “J1502S”; both components are steep-spectrum sources which indicate synchrotron emission. The radio luminosity of SDSS J1502 is inconsistent with that of star-forming galaxies, indicating that it is instead powered by AGN activity. Its X-ray luminosity and radio-to-X-ray luminosity ratio further support the discovery that SDSS J1502 is a dual AGN (Fu et al., 2011). Interestingly, very long baseline interferometry (VLBI) observations of SDSS J1502 with the European VLBI Network further resolved the secondary J1502S into two components (J1502SE and J1502SW) separated by 26 milliarcseconds (mas), or a projected distance of $\sim 138 \text{ pc}$ ($z = 0.39$) (Deane et al., 2014), making it one of the closest-separation *resolved* binary or dual AGNs discovered to date and surpassed only by the radio galaxy CSO 0402+379¹.

¹More recently, Kharb et al. (2017) reported an SMBHB candidate at the center of NGC 7674,

CSO 0402+379 was first identified by [Maness et al. \(2004\)](#) via Very Long Baseline Array (VLBA; an interferometer that consists of ten radio telescopes) as a compact symmetric object (CSO), a class of radio sources that are compact (< 1 kpc) in size and have emission on both sides of the central engine. However, several features of 0402+379 are atypical of CSOs; in particular, the object has a large-scale jet structure, and the two parsec-scale components (C1 and C2) are flat-spectrum sources. Both cores also appear to be variable, and possible motion of C2 is also detected ([Maness et al., 2004](#)). [Maness et al. \(2004\)](#) proposed several interpretations of this puzzling source, one of them being that C1 and C2 are two members of an SMBHB system. VLBA observations by [Rodriguez et al. \(2006\)](#) confirmed the jets and the two compact components seen previously in [Maness et al. \(2004\)](#) and that C2 is located between the jets, while C1 is offset from C2 by 7 pc ($z = 0.055$). They also measured the motion and the flux variability over a 15-yr baseline: both components increased in flux, while the lobes showed no clear variability; relative position measurements show that C2 appears to be moving towards C1 (however, the significance of the detection cannot be claimed), and both lobes are moving away from C2 ([Rodriguez et al., 2006](#)).

[Bansal et al. \(2017\)](#) further constrain the orbits of C1 and C2 from proper motion measurements and infer an orbital period of 3×10^4 years and a black hole mass of $1.5 \times 10^{10} M_{\odot}$. However, given the separation and the constraint on the black hole mass, the merger timescale of the binary due to gravitational radiation is

where they detected two cores separated by 0.65 mas, or 0.35 pc ($z = 0.029$). However, the cores have not been confirmed as AGNs.

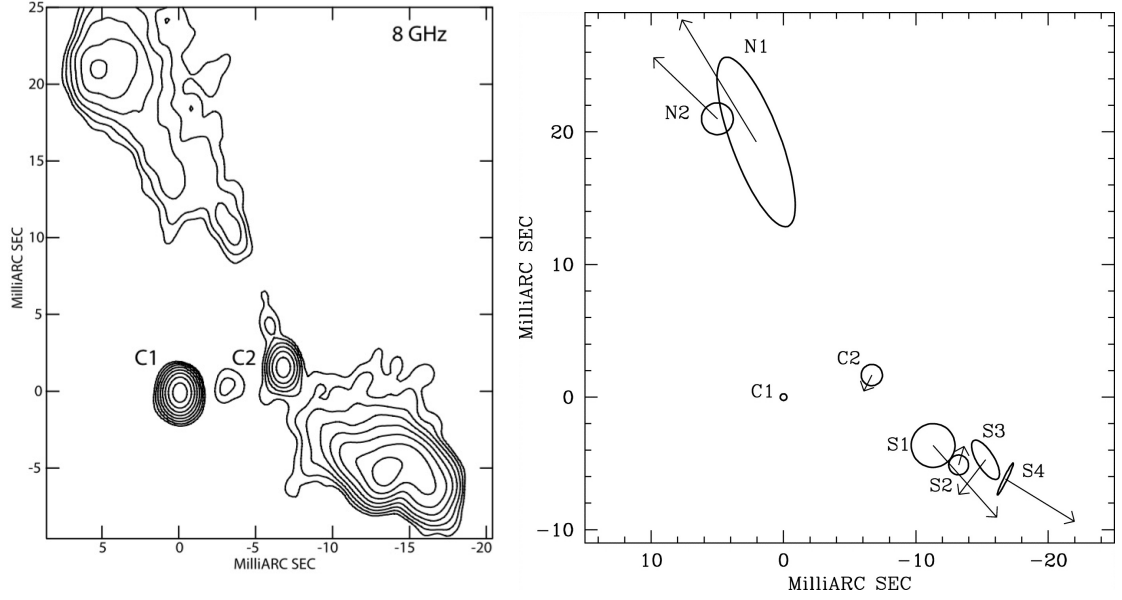


Figure 1.1: Left: the VLBA image of CSO 0402+379 at 8 GHz that shows the two compact components and the lobes. Right: the motion of each component relative to C1. (Both figures from [Rodriguez et al. \(2006\)](#))

$t_{\text{merger}} = 5.8 \times 10^6 \text{ yr} \left(\frac{a}{0.01 \text{ pc}} \right)^4 \left(\frac{10^8 M_{\odot}}{M_1} \right)^3 \frac{M_1^2}{M_2(M_1 + M_2)} \sim 10^{12} \text{ years}$ ([Peters, 1964](#)) — much longer than a Hubble time. Therefore, while it is already a gravitationally-bound binary at $< 10 \text{ pc}$, energy and angular momentum losses due to GW emission at this separation are negligible.

At closer, sub-parsec separations, SMBHBs cannot be spatially resolved by current telescopes, and indirect techniques are therefore required to search for them. If one of the SMBHBs is active, the broad line emitted by virialized gas bound to the SMBH may be shifted from its normal wavelength due to the SMBH's Keplerian velocity, and therefore offset broad lines could be signs of SMBHBs (or recoiling SMBHBs). Motivated by this physical picture, [Eracleous et al. \(2012\)](#) have system-

atically searched for quasars in SDSS whose $H\beta$ lines are offset from the rest-frame of the quasar by $> 1,000 \text{ km s}^{-1}$. For an observed (therefore, projected) velocity offset $u \sim 10^3 \text{ km/s}$ and a black hole mass $\sim 10^8 M_\odot$, the binary orbital period is $P = 2652 M_8 (\frac{\sin i \sin \phi}{(1+q)u_3})^3 \text{ yr}$, and the binary separation is $a = 0.432 M_8 (\frac{\sin i \sin \phi}{(1+q)u_3})^2 \text{ pc}$, where $M_8 = M_{\text{tot}}/10^8 M_\odot$, $u_3 = u/10^3 \text{ km s}^{-1}$, i is the inclination of the orbit, and ϕ is the orbital phase. Among the 15,900 SDSS quasars at $z < 0.9$, 88 met their selection criteria.

Further, the evidence for a binary would be stronger if the line is shifted during the time span of several observations over a baseline of a few years. In the study by [Eracleous et al. \(2012\)](#), the intervals between the original SDSS epochs and the follow-up observations are 5 – 10 years, which allow them to probe a velocity change of 100 – 200 km/s. Using a cross-correlation analysis, [Eracleous et al. \(2012\)](#) compute the change in χ^2 by shifting one of the spectra by small steps and are able to measure significant (at the 99 % level) shifts of the offset $H\beta$ lines in 14 quasars.

[Runnoe et al. \(2015\)](#) followed up the 88 quasars with $H\beta$ broad line offsets in [Eracleous et al. \(2012\)](#) so that many of them have three or more epochs of spectroscopy over a ~ 12 -yr baseline. In [Runnoe et al. \(2017\)](#), they measure the line velocity offset at each epoch relative to the first-epoch SDSS spectrum using the χ^2 cross-correlation method in [Eracleous et al. \(2012\)](#), and construct a radial velocity curve that shows the velocity offset at different epochs. For the 29 objects with at least three epochs of spectroscopy and in which they are able to reliably measure the velocity shifts (*i.e.* no significant line profile shape changes), they are able to set lower limits on the black hole masses by exploring the shortest periods of the

hypothesized SMBHBs that the velocity curves can tolerate. If the minimum black hole mass inferred is unphysically large, then the original hypothesis — that the system is an SMBHB — must have been false. Those minimum periods are decades to centuries, and the minimum black hole masses inferred from their method range from $4.7 \times 10^4 - 3.8 \times 10^8 M_\odot$, which are consistent with SMBH masses, and they are therefore not yet able to rule out the binary hypothesis for any of the candidates in their sample.

At yet closer separations ($\lesssim 0.01$ pc), the broad emission lines are no longer distinctly associated with one black hole, line profile becomes more complex, and velocity shifts are no longer good possible indicators of the orbital motion of the binary (Shen & Loeb, 2010). However, these SMBHBs have periods $P \sim 10$ years, which opens up the possibility of detecting them via periodic variability in their light curves. More excitingly, these SMBHBs emit gravitational waves (GWs) at frequencies between $f_{\text{GW}} \sim 10^{-7} - 10^{-9}$ Hz and can be probed by a pulsar timing array (Foster & Backer, 1990) in addition to via their electromagnetic signatures (Section 1.1.4).

1.1.3 The SMBHB Candidate OJ 287

The strongest SMBHB candidate identified via its optical variability is the blazar OJ 287. It has been monitored since the late-nineteenth century, and despite the poorer temporal sampling at earlier times, it was realized that outbursts in its light curve occur at a quasi-regular interval of $P_{\text{obs}} \sim 12$ years. It was proposed

in 1988 that these quasi-periodic bursts suggest that OJ 287 is an SMBHB system with an orbital period of $P_{\text{rest}} \approx 9$ years in the rest frame ($z = 0.306$, $P_{\text{rest}} = \frac{P_{\text{obs}}}{1+z}$) (Sillanpaa et al., 1988). In this early binary model, Sillanpaa et al. (1988) proposed that as the secondary black hole crosses the accretion disk of the primary, it tidally perturbs the disk and causes an inflow of matter towards the black hole.

However, there were features in the light curve that were not explained by the 1988 model. In 1996, it was proposed that the secondary black hole orbits around the primary on a ~ 12 -year period (observed frame) and crosses its accretion disk twice per orbit, causing two impact flares (which are separated by one to two years) per 12 yr-period (Lehto & Valtonen, 1996). The impact times give a unique solution of the binary orbit, and parameters including the orbital period, binary eccentricity, and precession of the orbit were determined. In 2008, there were enough well-sampled and well-defined outbursts such that the orbital shrinkage due to gravitational radiation could be measured: without energy loss due to GWs, the September 2007 burst would have occurred 20 days later (Valtonen et al., 2008). It was also predicted that the next outburst would occur in early January 2016, which was indeed observed in December 2015 (Valtonen et al., 2016). The profile shape of the 2015 flare was modeled as an expanding bubble of hot plasma (Pihajoki, 2016), and coordinated polarimetric and X-ray observations also agreed with the thermal nature of the burst (Valtonen et al., 2016).

While the 1996 binary model of OJ 287 remains somewhat controversial and other models including the precession of the radio jet (*e.g.* Britzen et al. (2018)) have been proposed, OJ 287 is one of the best SMBHB candidates to date and a

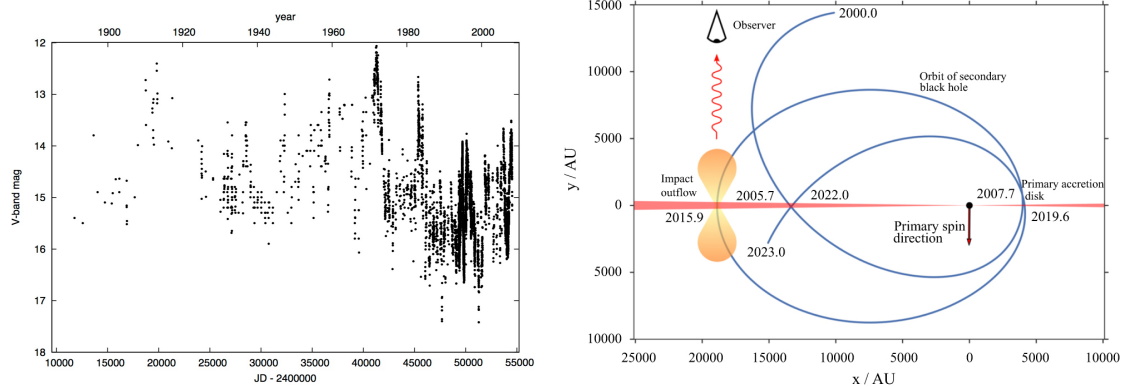


Figure 1.2: Left: the V-band light curve of the SMBHB candidate OJ 287 from ~ 1900 to ~ 2010 (Figure from [Valtonen et al. \(2008\)](#)). Right: the orbit of OJ 287 from 2000 – 2023 based on its binary model (Figure from [Valtonen et al. \(2016\)](#)).
potential target for the pulsar timing arrays ([Arzoumanian et al., 2014](#); [Babak et al., 2016](#); [Zhu et al., 2014](#)).

1.1.4 SMBHBs as the Sirens of Low-frequency Gravitational Waves

Pulsars are rotating, highly-magnetized neutron stars characterized by rapid, regular radio radiation. As the pulsars rotate, radio beams sweep across the direction of the Earth like lighthouse beacons and are detected as short pulses at regular intervals of milliseconds to seconds. The fastest-spinning pulsars are hence called millisecond pulsars (MSPs). They are thought to belong in binary systems and have been “recycled” through mass transfer from their binary companions, and they are characterized by particularly stable pulse periods.

The times of arrival (ToAs) of these pulses measured at the observatory are determined by factors including the pulsar spin and spin-down, radio waves propa-

gating in the interstellar medium, and a time standard. Measuring the precise ToAs of the pulses and fitting them to a timing model is a technique known as pulsar timing (*e.g.* [Edwards et al. 2006](#)). Deviations between the ToAs predicted by the timing model and the actually-measured ToAs are called “timing residuals” and are therefore due to effects that are not included in the timing model. In particular, [Sazhin \(1978\)](#) and [Detweiler \(1979\)](#) first realized that GWs would induce such “unexplained” timing residuals. So far, timing residuals of precision $\delta t \sim 1 \mu s$ have been achieved ([Arzoumanian et al., 2018](#); [Lentati et al., 2015](#); [Shannon et al., 2015](#)), and GWs are expected to induce timing residuals $\delta t_{\text{GW}} < 100 \text{ ns}$ (*e.g.* [Hobbs et al. 2010](#)).

Not only can timing residuals be induced by GWs, but they should also correlate as a function of the angular separations between pulsars. This distinctive correlation, known as the Hellings-Downs correlation ([Hellings & Downs, 1983](#)), distinguishes GW-induced residuals from those caused by systematic effects, and it requires a spatial distribution, or an “array”, of MSPs. There are currently three pulsar timing arrays (PTAs) in operation: the North American Nanohertz Observatory for Gravitational Waves (NANOGrav; [The NANOGrav Collaboration et al. 2015](#)), the European Pulsar Timing Array (EPTA; [Desvignes et al. 2016](#)), and the Parkes Pulsar Timing Array (PPTA; [Reardon et al. 2016](#)), and they have been observing MSPs since ~ 1990 at the cadence of once every few weeks. The lower end of the GW frequency band to which they are sensitive is therefore given by the current baseline of $\sim 10 - 15$ years, or $f_{\text{GW}} \sim 10^{-9} \text{ Hz}$, and the upper bound is limited by the observing cadence, hence $f_{\text{GW}} = \text{a few } \times 10^{-7} \text{ Hz}$ (*e.g.* [Hobbs et al. 2010](#)).

There are several sources of GWs that emit at these frequencies, and the ones that are most relevant to this thesis are SMBHBs with orbital periods of months to years. If individual SMBHBs are louder than the stochastic GW background — the superposition of signals from a population of SMBHBs — they may be resolved by the PTAs. [Sesana et al. \(2009\)](#) explored the detectability of individual SMBHBs and investigated the distribution of the binary parameters including GW frequency, chirp mass $M_{\text{ch}} = (M_1 M_2)^{3/5} / M_{\text{tot}}^{1/5}$ (where M_{tot} is the total mass of the binary), and redshift. They conclude that the loudest SMBHBs are massive ($M_{\text{ch}} > 10^8 M_{\odot}$) and at higher redshifts $z > 0.2$, and at least one resolvable source would induce a timing residual of $\delta t_{\text{GW}} \sim 10$ ns, assuming a five-year observation time. This is achievable with future PTA experiments but is below the upper limits of the current ones. Nevertheless, current experiments have put interesting constraints on SMBHBs ([Arzoumanian et al., 2014](#); [Babak et al., 2016](#); [Zhu et al., 2014](#)): the current most stringent limit ([Babak et al., 2016](#)) has put constraints on SMBHBs with $M_{\text{ch}} > 10^{10} M_{\odot}$ out to a luminosity distance of ~ 1 Gpc. The SMBHB candidates OJ 287 (Section 1.1.3) and PG 1302–102 (Section 1.3.2) are both below this limit and therefore cannot yet be ruled out. The most notable case of using PTA to constrain an SMBHB candidate is 3C66B, which was proposed as an SMBHB at $z = 0.02$ with a total mass $M = 5.4 \times 10^{10} M_{\odot}$, a period of 1.05 years, and a mass ratio of 0.1 ([Sudou et al., 2003](#)). The timing residual expected from these binary parameters is $\delta t_{\text{GW}} \sim 5 \mu\text{s}$, and therefore the signal would have been detected in the timing residual of PSR B1855+09 ($\delta t = 1.5 \mu\text{s}$) if 3C66B were a true SMBHB (with those parameters) ([Jenet et al., 2004](#)).

1.2 Theoretically Predicted Variability Signatures of an SMBHB

1.2.1 Modulated Mass Accretion as the Cause of Periodicity

As previously mentioned in Section 1.1.1, a circumbinary disk is expected to form around an SMBHB. Such binary-disk systems have been explored in two-dimensional (2D) or 3D hydrodynamical or magnetohydrodynamical (MHD) simulations for equal-mass binaries or binaries with a range of mass ratios (e.g. [Bowen et al. 2017, 2018](#); [D’Orazio et al. 2013](#); [Farris et al. 2014](#); [MacFadyen & Milosavljević 2008](#); [Noble et al. 2012](#); [Shi & Krolik 2015](#); [Shi et al. 2012](#); [Tang et al. 2018, 2017](#)). These studies find that the tidal torque of the binary clears and maintains a low-density gap (“cavity”) of a radius $\sim 2a$ (where a is the binary separation) between the binary and the circumbinary disk with material flowing into the cavity in two narrow streams and onto the black holes. The mass accretion rate measured for an individual black hole or the total accretion rate of the binary is strongly modulated by the binary orbital motion, resulting in periodic variation (or multiple periodicities) in the accretion rate (\dot{M}). The different simulations and their findings of the periodic behavior of the binary are briefly summarized as follows²:

In the 2D hydrodynamical simulation of an equal-mass binary with a circumbinary disk presented by [MacFadyen & Milosavljević \(2008\)](#), the mass accretion rate as measured at the inner boundary of the disk is modulated on the most prominent frequency $f = 2f_{\text{orb}}/9$ (where f_{orb} is the binary orbital frequency), accompanied by

²These simulations have adopted circular orbits.

a few harmonic frequencies. [D’Orazio et al. \(2013\)](#) and [Farris et al. \(2014\)](#) followed up on this work by exploring a range of mass ratios $q = M_2/M_1$ (the black hole mass ratio between the secondary and the primary) and investigated the dependence of mass accretion (and variability) on q . The choice of mass ratios is motivated by the wide distribution ($q \sim 0.1 - 1$) often assumed in galaxy merger models (e.g. [Volonteri et al. 2003](#)). Both studies find that significant modulation of mass accretion only occurs for less extreme mass ratios $q \gtrsim 0.1$; this can be understood by taking the limit of $q \rightarrow 0$: it therefore approaches a single black hole case and does not result in modulation by the binary orbital motion. [Farris et al. \(2014\)](#) also measured the mass accretion onto each BH (instead of through the inner boundary) and found that the accretion rate onto the secondary is larger than that onto the primary for all mass ratio cases: $(\dot{M}_2/M_2)/(\dot{M}_1/M_1) > 1$.

The first 3D MHD simulation of a binary-disk system was performed by [Shi et al. \(2012\)](#); it is therefore a more realistic description of the angular momentum exchange between the binary and the disk than previous hydro simulations. Similar to the MacFadyen & Milosavljevic simulation, which also includes an equal-mass binary, [Shi et al. \(2012\)](#) find two dominant frequencies that modulate \dot{M} : one at twice the binary orbital frequency, and the other at the orbital frequency of the “lump”, an overdensity of matter at the inner edge of the disk. However, because of the stronger internal stress due to MHD, it delivers more material into the cavity, and the accretion rate at the inner boundary is ~ 40 times larger than the previous hydro simulation.

Those simulations mentioned above keep the binary at a fixed orbit and adopt

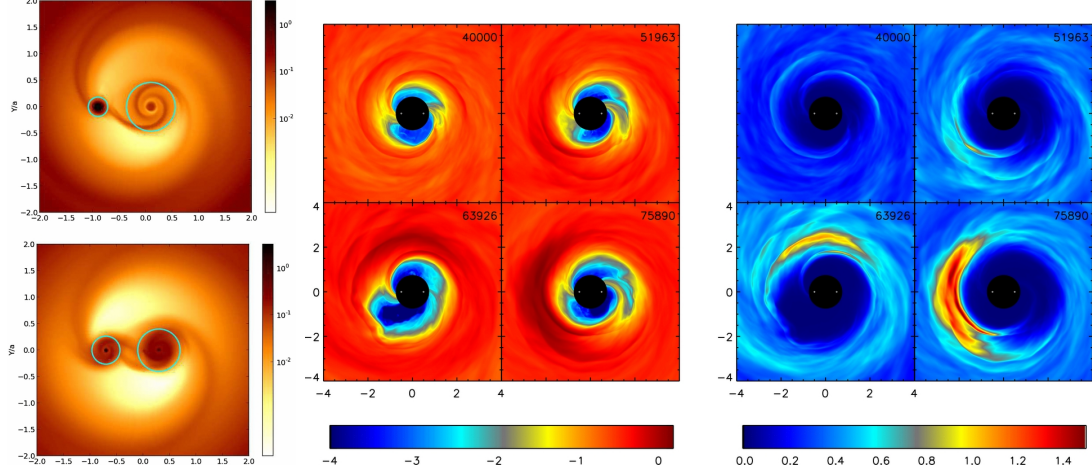


Figure 1.3: Left: a 2D hydrodynamical simulation of an SMBHB system with two different mass ratios. The time-averaged surface density profiles show the accretion disks around the individual (primary and secondary) black holes (“minidisks”), as well as the circumbinary disk around both black holes (Figure from [Farris et al. \(2014\)](#)). Center: a log-scale surface density profile from a MHD simulation of a binary. It shows the accretion streams flowing towards the binary at four different times in the simulation. Right: a linear-scale surface density profile from the same simulation. It emphasizes the time-evolution of the overdensity (“lump”) in the inner edge of the circumbinary disk. (Both figures from [Noble et al. \(2012\)](#))

Newtonian dynamics. Those assumptions are appropriate when the binary separation is farther apart, but will no longer suffice when the binary has evolved to a much closer separation (*e.g.* a few tens of gravitational radii) and the black holes are rapidly inspiraling due to gravitational wave radiation — this would require post-Newtonian ([Noble et al., 2012](#)) or a full general relativistic (GR) treatment ([Gold et al., 2014](#)). Those simulations find a similar disk structure and mass accretion rate

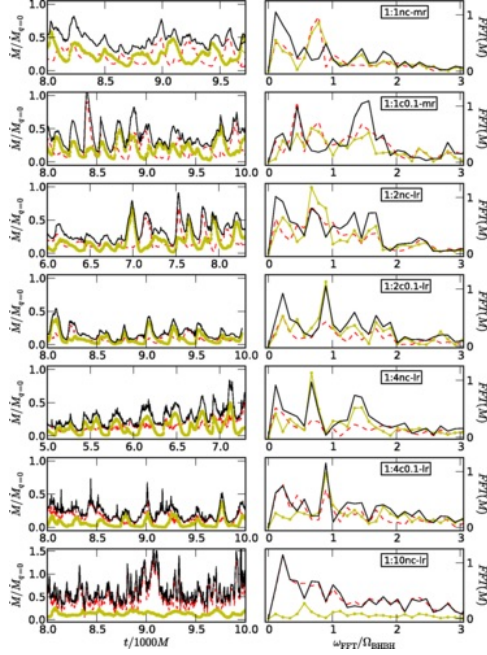


Figure 1.4: Left: the \dot{M} variation as a function of time, which depends on different mass ratios and details of the simulations. Right: the Fourier transform of each of the \dot{M} curves on the left. (Figure from [Gold et al. \(2014\)](#))

as the Newtonian case.

However, the interpretation of an observed variability period (or periods) may not be straightforward, as those simulations of different mass ratios have shown ([D’Orazio et al., 2013](#); [Gold et al., 2014](#)). It has also been pointed out that emission from the minidisks or circumbinary disk could also smear out the periodic signatures ([Gold et al., 2014](#); [Noble et al., 2012](#)), making it difficult to distinguish an SMBHB system from a conventional AGN. Despite these caveats, if \dot{M} is directly translated to EM radiation, these SMBHBs would manifest as luminous AGNs that show periodic variability in their photometric light curves, which have periods that are within a factor of a few of the orbital periods.

1.2.2 Doppler Boosting as the Cause of Periodicity

Another possible cause of periodic variability is the relativistic Doppler boosting of the emission from the minidisk, which is a model that was proposed by [D’Orazio et al. \(2015\)](#) to interpret the periodicity of the SMBHB candidate PG 1302–102 (Section 1.3.2). The velocity of the secondary black hole is $v_2 = (2\pi/1 + q)(GM_{\text{tot}}/4\pi^2 P)^{1/3}$, and for the binary parameters inferred for PG 1302–102, the velocity is moderately relativistic. Even if the minidisk radiates steadily, the radiation will be beamed towards the forward-moving direction of the secondary black hole. From the viewpoint of the observer on Earth, the apparent flux F is therefore modulated sinusoidally on the orbital frequency: $\Delta F_\nu/F_\nu = \pm(3-\alpha)v\cos(\phi/c)\sin(i)$, where α is the power-law slope of the quasar spectrum $F_\nu \propto \nu^\alpha$, $v\sin(i)$ is the line-of-sight velocity, and ϕ is the orbital phase angle. As can be seen from the equations above, this model requires that the black holes have unequal masses (q is small) and that the binary orbit is viewed not far from edge-on ($\sin(i)$ is large), so that the beaming effect is strong. However, one caveat is the presence of a circumbinary disk, which may obscure the binary due to the high inclination angle and make it difficult to observe this variability signature ([d’Ascoli et al., 2018](#)).

A corollary of the Doppler boost model is that variability amplitudes A in different bandpasses are directly related to the spectral slopes in the respective bands, *i.e.* $A_{\text{FUV}}/A_{\text{opt}} = (3 - \alpha_{\text{FUV}})/(3 - \alpha_{\text{opt}})$ and $A_{\text{NUV}}/A_{\text{opt}} = (3 - \alpha_{\text{NUV}})/(3 - \alpha_{\text{opt}})$. If the slopes can be measured from the far-UV and near-UV spectra of the source, the amplitude ratio would be useful supporting evidence for the Doppler

boost model of the putative binary (Charisi et al., 2018; D’Orazio et al., 2013).

1.3 The Search for SMBHBs

1.3.1 The Detectability of SMBHBs in a Time Domain Survey

If SMBHBs spend a significant fraction of their lifetimes at orbital separations that correspond to periods of months to years, they could be detected as a population of periodic quasars or AGNs in time domain surveys that repeatedly visit a large number of objects over a period of a few years. This was explored by Haiman et al. (2009). For a binary whose orbital decay is driven by GW emission, the decay timescale is given by $t_{\text{GW}} = -r/\dot{r} \propto r^4 \propto t_{\text{orb}}^{8/3}$ (for a fixed black hole mass; r and t_{orb} indicate the orbital radius and period, respectively), and the residence time that the binary spends at the orbit is then $t_{\text{res}} = t_{\text{GW}} \propto t_{\text{orb}}^{8/3}$. For a population of GW-driven SMBHBs, their number fraction should therefore be proportional to their residence times: $f_{\text{var}} = t_{\text{res}}/t_{\text{Q}}$, where t_{Q} is the “lifetime” that the binary is “active” as a quasar and is a few $\times 10^7$ years (Martini, 2004). Given the power-law dependence of t_{res} on t_{orb} , the prediction is that a statistical sample of periodic quasars should also follow a power-law relation:

$$f_{\text{var}} = N_{\text{orb}}/N_{\text{tot}} = (10^7 \text{yr}/t_{\text{Q}})[t_{\text{var}}/50.2(1+z)\text{weeks}]^{8/3} M_7^{-5/3} q_s^{-1}, \quad (1.1)$$

where $M_7 = M_{\text{BH}}/10^7 M_{\odot}$, $q_s = 4q/(1+q)^2$, and $t_{\text{var}} = t_{\text{orb}}(1+z)$. On the other hand, a population of SMBHBs that are at farther separations and are still in the

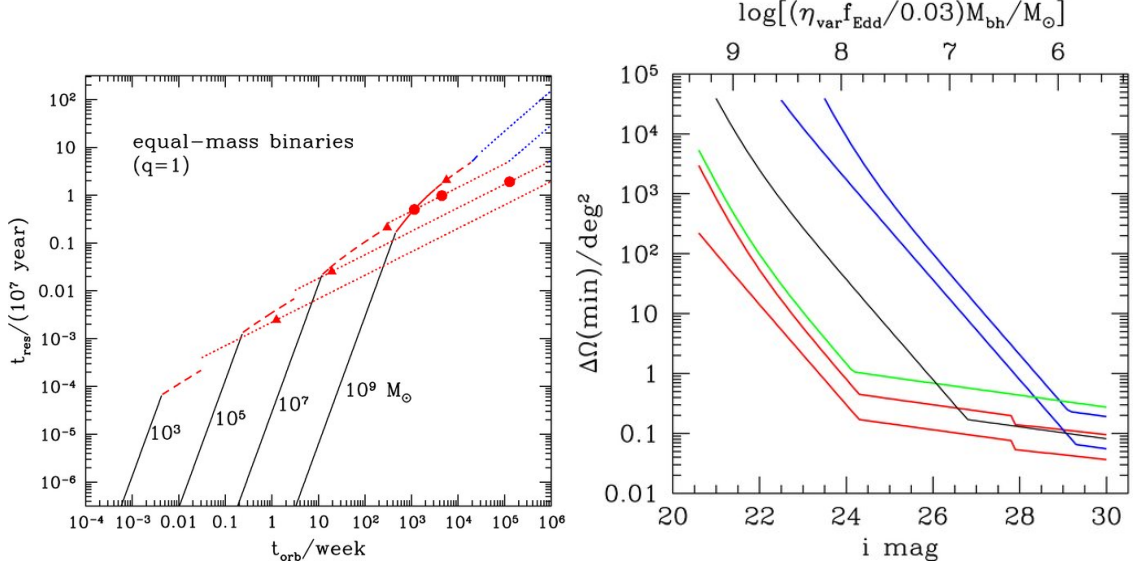


Figure 1.5: Left: The residence times of SMBHBs of different masses as a function of orbital periods. Right: the sky coverage and the limiting magnitude required to find a population of periodic quasars. The black line is calculated for the fiducial values in the text. (Both figures from [Haiman et al. \(2009\)](#))

gas-driven stage of orbital decay should have a flatter power-law scaling relation $f_{\text{var}} \propto t_{\text{orb}}^\alpha$, where $\alpha < 8/3$.

One may realize from Equation 1.1 that in a very large sample of quasars, SMBHBs that manifest as periodic sources may not be so rare; it is therefore possible to search for them in a large time domain survey. [Haiman et al. \(2009\)](#) calculated the required survey area and magnitude depth in order to detect a statistical sample of periodic sources by adopting a set of fiducial values, including a quasar lifetime of $t_Q = 10^7$ years, a mass ratio $q = 1$, an Eddington fraction $f_{\text{Edd}} = 0.3$, and a variability fraction $\eta_{\text{var}} = 0.1$, and predicted *e.g.* 20 sources varying at $t_{\text{var}} = 35$ weeks (the redshift of the sources is fixed at $z = 2$) in a survey with a sky coverage

of 100 deg^2 and a limiting magnitude of $i = 24 \text{ mag}$. According to Equation 1.1, the same survey volume would find *e.g.* $2^{8/3} \times 20 = 127$ sources varying at $t_{\text{var}} = 70$ weeks. There is also a trade-off between the survey area and the limiting magnitude of the survey: a shallower magnitude depth would require a larger survey area in order to probe the same sky volume. For a fixed black hole mass, this survey requirement also depends on the values of q , η_{var} , and f_{Edd} : a smaller q results in a longer t_{res} and therefore requires a smaller volume to find the same number of periodic quasars; increasing either η_{var} or f_{Edd} (or both parameters) would also lead to a smaller required survey volume.

More excitingly, an optical time domain survey with a baseline of a few years would be able to detect periods of a few months to a few years. For typical SMBH masses of $10^6 - 10^9 M_{\odot}$, these timescales correspond to binaries in the GW-driven regime of orbital evolution ($a \sim 10^{-3} \text{ pc}$ or $\sim 10^2$ gravitational radii r_g). A systematic search in a large-field optical time domain survey can therefore potentially find a population of close-separation SMBHBs in the GW-regime.

1.3.2 Systematically Searching for Periodically Varying Quasars

The predicted survey requirement by Haiman et al. (2009) is an excellent match to the sky volume probed by existing large surveys such as the Catalina Real-time Transient Survey (CRTS; Drake et al. 2009), the Palomar Transient Factory (PTF; Law et al. 2009), and the Pan-STARRS1 survey (PS1; Kaiser et al. 2010), and systematic searches for periodic quasars in those survey datasets have been made in

the past few years.

[Graham et al. \(2015b\)](#) performed a systematic search for periodic quasars in the CRTS, which operates three telescopes from both hemispheres, covering a sky area of $\sim 30,000 \text{ deg}^2$ to a magnitude depth of $V \sim 19 - 21.5 \text{ mag}$ (depending on the telescope) over a nine-year baseline. Their initial sample of quasars was first selected by cross-matching a catalog of spectroscopically-confirmed quasars with the CRTS data set. After applying the minimum sampling criterion and removing spurious detections, the final sample consists of 243,486 quasars.

[Graham et al. \(2015b\)](#) then applied a combination of wavelet transform and autocorrelation techniques to select candidates that display periodic behavior; they also required that the periodic variation persists for at least 1.5 cycles over the observational baseline. 111 candidates passed their selection criteria. To calculate the number of regular variable quasars that show periodicity by chance, they also simulated a comparable number of mock light curves characterized by the Damped Random Walk model (DRW; [Kelly et al. 2009](#); see Section 1.4.1 for a review of AGN variability and the DRW model); none of the simulated light curves passed their selection criteria.

The detection rate of [Graham et al. \(2015b\)](#) is roughly compatible with the predicted number of SMBHBs at low redshifts ([Volonteri et al., 2009](#)) and the fraction of binaries as a function of orbital period ([Haiman et al., 2009](#)). Assuming all periodic candidates are true SMBHBs, the inferred binary orbital separations would be in the milli- to centi-parsec regime, and their GW strain amplitudes are individually consistent with the current upper limit from the pulsar timing arrays.

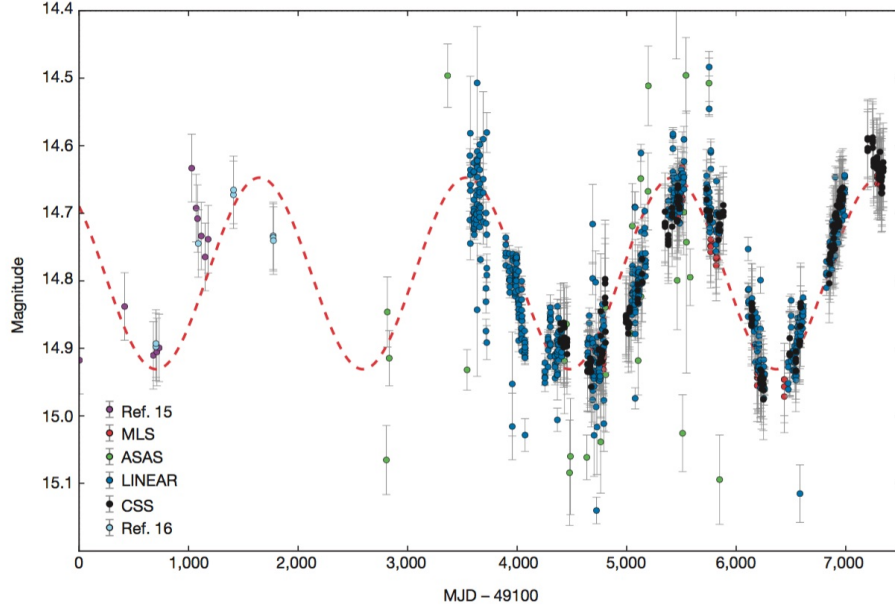


Figure 1.6: The combined light curve of the SMBHB candidate PG 1302–102 from LINEAR, CRTS, and the archival data. (Figure from [Graham et al. \(2015a\)](#))

The most significant candidate from the [Graham et al. \(2015b\)](#) sample of periodic candidates is PG 1302–102 ([Graham et al., 2015a](#)). It has a median magnitude of $V = 15$ mag and a variability amplitude of ~ 0.14 mag. It was covered by the CRTS and the Lincoln Near-Earth Asteroid Research (LINEAR) for a total of ~ 2 well-sampled cycles. Its light curve can be well-fitted to a sinusoid of a period $P = 1,884 \pm 88$ days and modeled by the relativistic Doppler boosting of the minidisk of the secondary black hole ([D’Orazio et al. 2015](#); Section 1.2.2).

[Charisi et al. \(2016\)](#) performed their systematic search in the PTF survey, which covered a total sky area of $\sim 8,000 \text{ deg}^2$ down to a magnitude depth $R \sim 20.5$ mag over a \sim four-year period. They cross-matched PTF sources with a catalog of spectroscopically-confirmed quasars and pre-processed the light curves by removing

outlier data points. They further binned the measurements on the same night and only selected light curves with dense temporal sampling ($N > 50$ in the R-band). The number of quasars in their sample is therefore 35,383.

They then searched for periodic signals using a generalized version of the Lomb-Scargle (LS) periodogram (Lomb, 1976; Scargle, 1982). The LS periodogram is a standard Fourier method for detecting periods in light curves with uneven sampling, and for a range of trial frequencies, the one where the periodogram power is maximum indicates a possible periodic signal at that frequency. As the null hypothesis of the LS periodogram is pure white noise, they also generated mock light curves modeled by the DRW process and compared their periodograms with those of selected candidates; a periodic quasar candidate from their sample is considered significant if its p -value $< 4 \times 10^{-5}$. 50 candidates satisfy this threshold and have more than 1.5 cycles of variation. They then obtained light curves of the candidates from the intermediate-PTF (iPTF, the extension of the PTF survey) and CRTS surveys and recalculate the p -values of the extended baseline light curves. 33 candidates have p -values $< 1 \times 10^{-3}$ and are considered significant by their analysis.

Periodic quasar candidates discovered in those surveys are summarized in Table 1.1. In comparison with the candidates selected by Graham et al. (2015b), the Charisi et al. (2016) search is more sensitive to shorter periods and fainter sources. In both searches, the distribution of binary residence times is most consistent with the expected distribution (Haiman et al. 2009; Section 1.3.1) if all candidates have the mass ratio $q = 0.01$, assuming all periodic quasar candidates from Charisi et al. (2016) host SMBHBs and 25% of the candidates from Graham et al. (2015b) host

Table 1.1: Summary of Systematic Searches for Periodically Varying Quasars

| Systematic Search | Survey | Initial Sample of Quasars | Number of (Significant) Periodic Candidates |
|---------------------------------------|--------|---------------------------|--|
| Graham et al. (2015b) | CRTS | 243,486 | 111 |
| Charisi et al. (2016) | PTF | 35,383 | 50 (33) |

SMBHBs ([Charisi et al., 2016](#)).

However, AGN variability is stochastic (see Section 1.4.1) and can easily mimic a periodic variation over a short baseline (see Section 1.4.2). Therefore, normal AGNs that do not host SMBHBs may contaminate a periodic sample and present a challenge for the search for robust SMBHB candidates via their optical variability. A significant part of this thesis presents the extended baseline monitoring of the periodic candidates from PS1 and a more rigorous method that selects a more robust sample of binary candidates.

1.4 Quasar Variability and the Challenges of Searching for Periodic Quasars

1.4.1 Optical Variability of Quasars

Active galactic nuclei (AGNs) and quasars are long known to be variable on timescales from hours to years and in wavelengths from X-ray to radio (*e.g.* review

by [Peterson \(2001\)](#) and review on variability of blazars by [Ulrich et al. \(1997\)](#)). While AGN variability has been measured since the age of photographic plates (*e.g.* [Matthews & Sandage 1963](#); [Sillanpaa et al. 1988](#)), modern, digital sky surveys have produced a large amount of photometric data and have transformed the study of the variable sky. Some examples of those surveys include the Sloan Digital Sky Survey (SDSS; [York et al. 2000](#)), the Catalina Real-time Transient Survey (CRTS; [Drake et al. 2009](#)), and Pan-STARRS1 (PS1; [Kaiser et al. 2010](#)), and some of the data from those surveys will appear in this thesis.

[Vanden Berk et al. \(2004\)](#) used a sample of $\sim 25,000$ spectroscopically-confirmed quasars from SDSS with two epochs of photometry in three bands and measured the dependence of variability on parameters such as luminosity, rest-frame wavelength, and the time lag between the epochs. It was the largest sample of variable quasars at that time. By measuring the structure function (SF), they find that the variability amplitude increases with time lag; they also find that quasars vary more at shorter rest wavelengths, and more luminous quasars are less variable. The Stripe 82 survey of SDSS, which repeatedly visited a narrow stripe of the sky, allowed one to move beyond few-epoch photometry and produced a large number of light curves, the measurements of the brightness as a function of time. This has enabled one to study individual variable quasars in greater quantitative detail. For example, [Sesar et al. \(2007\)](#) found that $\sim 90\%$ of the quasars in their Stripe 82 sample vary at the 0.03 mag level and 30 % vary at the > 0.1 mag level; the highly variable nature of quasars also make it as good a selection algorithm as the color-magnitude or color-color diagram.

The light curve variability of an AGN is stochastic and aperiodic (*e.g.* [Peterson 2001](#)), *i.e.* the variation appears to be random and does not repeat itself regularly. Motivated by the potential to study AGN physics via its variability, [Kelly et al. \(2009\)](#) modeled the AGN variability as a stochastic process of two parameters, the characteristic timescale and the variability amplitude. This is known as the Damped Random Walk (DRW) process, or an Ornstein-Uhlenbeck (O-U) process ([Gillespie, 1996](#)). The power spectral density (PSD), or how much power is at a certain frequency, of DRW is:

$$P(f) = \frac{2\sigma^2\tau^2}{1 + (2\pi\tau f)^2}, \quad (1.2)$$

where τ is the characteristic timescale and σ is the variability amplitude on short timescales. As one can see from Equation 1.2, the variability power decreases as f^{-2} at frequencies $f > (2\pi\tau)^{-1}$ and flattens towards white noise at lower frequencies. By modeling quasar light curves as the DRW process, [Kelly et al. \(2009\)](#) find that the characteristic timescale τ is correlated with black hole mass and luminosity of the quasar but the short-timescale variability amplitude σ is anti-correlated with those two physical parameters. The characteristic timescales, ranging between ~ 10 days to ~ 10 years, are consistent with the thermal or orbital timescale, and the success of DRW in fitting light curves also suggests that quasar variability is driven by stochastic processes, such as fluctuations in the disk caused by a turbulent magnetic field ([Kelly et al., 2009](#)).

The SF ensemble analysis of [Vanden Berk et al. \(2004\)](#) was based on the as-

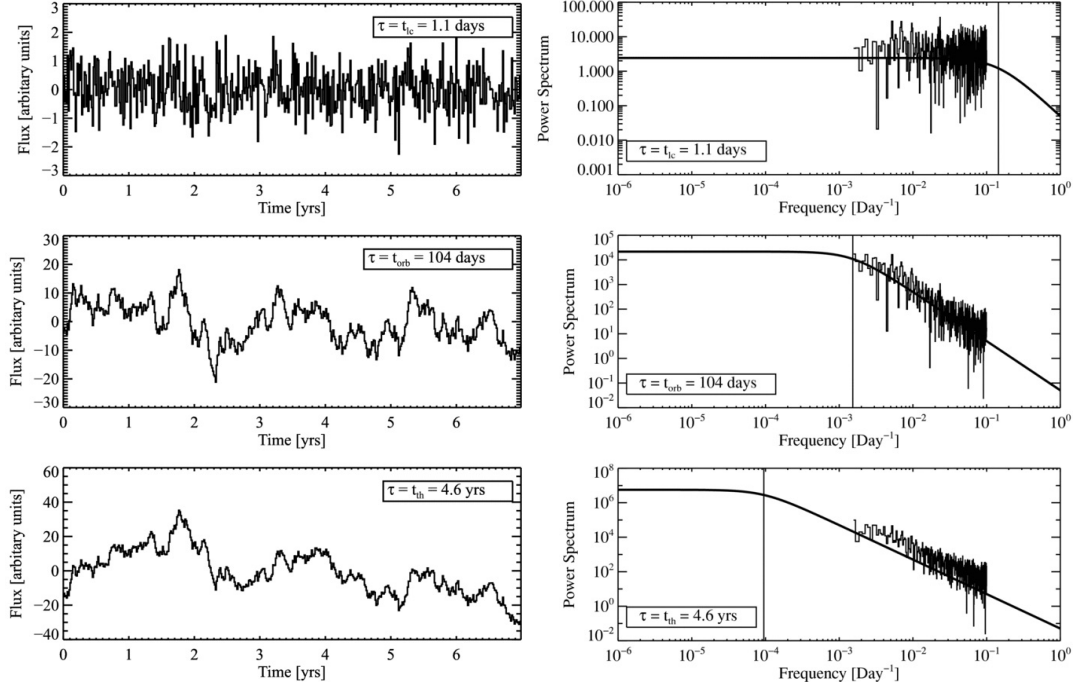


Figure 1.7: Left: light curves simulated from the Damped Random Walk model with different characteristic timescales. Right: the power spectra of the light curves on the left. (Both figures from [Kelly et al. \(2009\)](#))

sumption that a large statistical sample of quasars (each was observed at two epochs) would reveal the same properties as well-sampled light curves of individual quasars. In order to understand the individual and ensemble properties of quasar variability, [MacLeod et al. \(2010\)](#) applied the DRW model to $\sim 9,000$ spectroscopically-confirmed quasars in the SDSS Stripe 82 survey and confirmed previous results that DRW is a good model for quasar variability ([Kelly et al., 2009](#); [Kozłowski et al., 2010](#)). Since the structure function $SF \propto \Delta t^\beta$ (where Δt is the time lag) is equivalent to $P(f) \propto f^\alpha$, where $\alpha = -2\beta - 1$ ([Bauer et al., 2009](#)), the power-law slope $\beta = 0.5$ is therefore steeper than what was previously measured by [Vanden Berk](#)

et al. (2004) ($\beta = 0.3$).

Despite the success and popularity of the DRW model in describing AGN variability, recent studies have found deviations from the DRW model in their analyses of AGN light curves from ground-based surveys and high photometric precision light curves produced by *Kepler*, the exoplanet hunting mission. Two results from these studies (e.g. Aranzana et al. 2018; Caplar et al. 2017; Mushotzky et al. 2011; Smith et al. 2018a) are: (1) there is a variation of power-law PSD slopes; and (2) those slopes are in general steeper than $\alpha = -2$, the high frequency slope of the DRW model, and range between -2 and -3 (Aranzana et al., 2018; Smith et al., 2018a). Understanding the variability of normal quasars (*i.e.* single black hole-powered) therefore has farther-reaching implications than studying quasar accretion physics; it also affects our search for periodic quasars that could host SMBHBs and our estimation of their statistical significance, as I will discuss in Section 1.4.2 and throughout this thesis.

1.4.2 Red Noise Contamination of the SMBHB Candidate Sample

There have been ~ 200 SMBHB candidates reported based on their periodicity (see Section 1.3.2). However, normal AGN variability is stochastic, and the fluctuation of “red noise” can easily mimic a periodic variation over a few cycles, especially when the photometric uncertainty is large and the sampling is uneven. To demonstrate this, Vaughan et al. (2016) generated mock light curves under two different red noise models, a DRW model and a broken power law (BPL) PSD model;

the choice of the power-law slopes of the BPL model is based on the power spectrum analysis of Zw 229-15 (Edelson et al., 2014), and the break frequency f_{br} is scaled down from that of Zw 229-15 based on a $M_{\text{BH}} - f_{\text{br}}$ relation. They simulated 100,000 light curves under each model and looked for periodic candidates that have comparable goodness-of-fit as PG 1302-102 and a similar period range as the Graham et al. (2015b) periodic sample (Section 1.3.2). They find “periodic candidates” at a not-insignificant rate of one to two per 1,000 simulations under both models, and the period distribution of those false positives is similar to that of the Graham et al. (2015b) candidate (*i.e.* more candidates at longer periods), suggesting that one tends to find false periodicities with long periods. They also find that the rate of false periods is highly dependent on the choice of the power law slopes and the break frequency; for example, if the high-frequency slope is $\alpha = -3$ instead of -2 , the number of false positives increases by a factor of a few (Vaughan et al., 2016). Therefore, in a large time domain survey of $\sim 10^5$ quasars (*e.g.* the Graham et al. 2015b CRTS sample), the effect of red noise contamination cannot be ignored, and estimating the statistical significance of selected periodic candidates also requires a close inspection of normal quasar variability.

Fortunately, as Vaughan et al. (2016) suggested, the detected periodic candidates can be easily tested with further observations; in the long term (at least ~ 5 cycles), a true periodic signal should persist, while stochastic variability does not. I will put the periodic candidates from PS1 to the test with extended baseline imaging in this thesis (Chapters 3 - 5).

Sesana et al. (2017) tested the binary hypothesis of the periodic candidates

from [Graham et al. \(2015b\)](#) and [Charisi et al. \(2016\)](#) from the perspective of the pulsar timing arrays (PTAs). In order to build a gravitational wave background (GWB) from a population of SMBHBs, it first requires the knowledge of the chirp mass of each candidate. Since the black hole mass measured from the quasar spectrum is taken to be the total mass M_{tot} of the system, they assigned mass ratios q to candidates using three different mass ratio models: (1) the distribution of q is lognormal, peaking at $\log q = 0$ (but only for $q < 1$, by definition); this is motivated by the expected q distribution of SMBHBs formed in major galaxy mergers; (2) the distribution of q ranges from < 0.01 to 1; this distribution peaks at ~ 0.1 but has a minimum cut-off at $q = 0.05$; this is representative of the modulated mass accretion model, which requires a larger mass ratio (Section 1.2.1); (3) same as Model (2), but without the cut-off; this model is representative of the Doppler boosting case, which requires a small mass ratio (Section 1.2.2). Since the black hole mass M_{BH} estimates also have a systematic uncertainty of ~ 0.3 dex (*e.g.* [Shen et al. 2008](#)), they also consider two M_{BH} scenarios: one assumes the measurements are exact, and the other includes the uncertainties. They therefore built a GWB under six different models.

They then considered a number of effects due to incompleteness of the search, including: (1) only consider binary candidates at $z < 1.3$, at which the [Graham et al. \(2015b\)](#) periodic sample should be less incomplete; (2) include candidates at all redshifts; (3) correct for the incompleteness of sky coverage. Since interactions with stars and gas can add eccentricity to the binary and therefore reduce the GW signal at low frequencies, they have also considered this effect. After those considerations,

they find that the GWB inferred from the [Graham et al. \(2015b\)](#) sample is in tension with the PTA upper limits, *i.e.* the inferred amplitude is higher by at least a factor of a few than the current upper limits reported in [Shannon et al. \(2015\)](#), [Lentati et al. \(2015\)](#), and [Arzoumanian et al. \(2016\)](#), and the periodic sample from [Charisi et al. \(2016\)](#) similarly infers a much larger GWB amplitude. While the tension can be alleviated by *e.g.* fixing all mass ratios at $q = 0.01$ and assuming all black hole masses are overestimated, this study places a hard, independent constraint on the SMBHB samples, suggesting that many of the periodic candidates may be false positives. As they also find by calculating individual contributions from the binary candidates, only misidentifying a few loudest sources would have a large effect on the inferred GWB amplitude. Down-selecting a more robust sample of SMBHB candidates is therefore one of the main objectives of this thesis.

This thesis is organized as follows: Chapter [2](#) presents the most significant periodic candidate from our pilot study in MD09, one of the fields in the Pan-STARRS1 Medium Deep Survey (PS1 MDS). Chapter [3](#) presents a full analysis of the PS1 field MD09 and follows up the candidates using extended imaging with the Discovery Channel Telescope and archival data, in order to identify false positives that are due to the stochastic variability (“red noise”) of normal quasars that do not host SMBHBs. To further address the issue of red noise contamination of periodic candidate samples, I set up the expectations for a true periodic signal (in the presence of red noise) in Chapter [4](#) and re-analyze the well-known SMBHB candidate PG 1302–102 using an extended light curve and a more rigorous method. Those pieces in Chapter [2](#) - [4](#) are put together in Chapter [5](#), where I expand the

systematic search to all ten fields of PS1 MDS. Our more robust subsample of periodic quasar and SMBHB candidates from PS1 MDS can then be followed up with multi-wavelength observations in order to search for other electromagnetic signatures that could independently verify the binary hypothesis (Chapter 6).

Chapter 2: A Periodically Varying Luminous Quasar at $z = 2$ from the Pan-STARRS1 Medium Deep Survey: A Candidate Supermassive Black Hole Binary in the Gravitational Wave-Driven Regime

2.1 Introduction

The expectation for the existence of supermassive black hole binaries (SMBHBs) in galaxy nuclei is supported by two well-established properties of galaxies: (1) high spatial resolution observations of nearby galaxies have demonstrated that SMBHs are ubiquitous in the centers of galaxy bulges ([Magorrian et al., 1998](#)) with masses tightly correlated with the mass and structure of their host galaxies ([Ferrarese & Merritt, 2000](#); [Gebhardt et al., 2000](#); [Graham et al., 2001](#)), and (2) galaxies in a Λ CDM Universe build up their structure hierarchically through mergers (*e.g.* [Springel et al. 2005](#)). When two galaxies merge, their SMBHs will sink to the center through dynamical friction and through three-body interactions with stars and viscous exchange of angular momentum with circumbinary gas form a gravitationally bound binary that eventually coalesces due to the radiation of gravitational waves (GWs; [Begelman et al. 1980](#)).

Recent progress has been made in the detection of “dual active galactic nuclei (AGNs),” double active nuclei in assumed merged galaxy systems with kiloparsec-scale separations (Comerford et al., 2009b; Komossa et al., 2003). These dual AGNs, while a product of a galaxy merger, are not yet gravitationally bound, and thus are not necessarily fated to coalesce. A true SMBHB becomes gravitationally bound on the scale of parsecs, which, beyond our Local Group of galaxies, is well below the angular resolving power of the most powerful current, or even future, telescopes. However, several promising candidates have been identified indirectly via spectroscopy: quasars with offset and/or drifting broad-line peaks attributed to a broad-line region in orbit around an SMBH’s binary companion (Barrows et al., 2011; Boroson & Lauer, 2009; Dotti et al., 2009). However, alternative scenarios have been proposed that do not require an SMBHB, including double-peaked lines from a single accretion disk (Chornock et al., 2010).

A promising observational signature of SMBHBs is their variable accretion luminosity. One of the first sub-parsec SMBHB candidates, OJ 287, was identified by its variability behavior (Lehto & Valtonen, 1996). OJ 287 is a quasar that demonstrates regular optical outbursts on a timescale of 12 yr that has been modeled as the result of a secondary SMBH companion passing through the primary SMBH’s accretion disk (Valtonen et al., 2008). Such a configuration should be rare since the secondary BH’s orbital axis must be highly misaligned with the primary BH’s accretion disk axis in order for it to pass through its disk. A more generic signature of an SMBHB is likely to be related to accretion through its circumbinary disk.

In a gas-rich galaxy merger, strong gravitational torques drive gas inward,

triggering both star formation and BH accretion (Hopkins et al., 2006). In particular, hydrodynamical simulations of circumbinary disks show that accretion via “hot streams” onto the BHs is strongly modulated by the binary’s orbital motion for mass ratios of $0.05 < q \leq 1$ (D’Orazio et al., 2013; Gold et al., 2014; MacFadyen & Milosavljević, 2008; Noble et al., 2012; Shi et al., 2012). Simulations (D’Orazio et al., 2013; Farris et al., 2015) also detect a $t \sim 6 t_{\text{orb}}$ timescale originating from a surface density “lump” just outside the central cavity of the circumbinary disk, which is a persistent but secularly evolving feature.

While working on our paper, we became aware of the report of PG 1302–102, a periodically variable quasar discovered by the Catalina Real-Time Transient Survey (CRTS; Graham et al. 2015b). It is a 15 magnitude quasar at $z = 0.2784$, varying at the 0.14 mag level with a period of 5.2 ± 0.2 yr, with good sampling over 1.8 cycles and extended archival data going back 20 yr. Their physical interpretation for its variability is an SMBHB ($\log(M/M_{\odot}) \sim 8.5$, $a \sim 0.01$ pc), its luminosity being modulated due to either a precessing jet or an overdensity (“hot spot”) in the inner edge of its circumbinary disk.

In this Letter, we present our most significant detection from the systematic search for periodically varying quasars in the Pan-STARRS1 Medium Deep Survey (PS1 MDS) field MD09. PSO J334.2028+01.4075 is a radio-loud quasar at $z = 2.060$ with archival spectroscopy from FQBS and extended baseline photometry from CRTS. The 8.5 yr baseline of the PS1+CRTS light curve is well described by a simple sinusoid, consistent with theoretical simulations for the modulated accretion rate in a $0.05 < q < 0.25$ mass-ratio SMBHB. We use the rest-frame period and

virial black hole mass estimate to infer an orbital separation of the binary that is in the GW-driven regime.

2.2 Theoretical Predictions

The dynamics of a gravitationally bound SMBHB system can be described by Kepler’s third law:

$$t_{\text{orb}} = 0.88 \text{ yr} \left(\frac{M}{10^7 M_{\odot}} \right) \left(\frac{a}{10^3 R_s} \right)^{3/2}, \quad (2.1)$$

where R_s is the Schwarzschild radius, $R_s = \frac{2GM}{c^2}$; a is the separation between the BHs; and M is the total mass of the system. Haiman *et al.* calculate the minimum survey area to detect a statistically significant sample of quasars powered by SMBHBs as a function of variable magnitude depth, assuming reasonable values for the quasar luminosity function, quasar lifetime ($t_Q = 10^7$ yr), the Eddington fraction ($f_{\text{Edd}} = 0.3$), and the fractional variability amplitude ($\Delta f/f = 0.1$) (Haiman et al., 2009). The variability detection threshold we have achieved in MD09 (Section 2.4) corresponds to a $\Delta f/f > 0.1$ sensitivity for point sources brighter than $m \sim 21$ mag, and thus a variable magnitude of 23.5 mag. At this depth, Haiman et al. (2009) require an area of $\sim 100 \text{ deg}^2$ to yield a sample of over 100 SMBHBs (Haiman et al., 2009); an excellent match to the area of PS1 MDS (80 deg^2). Furthermore, the baseline (4.2 yr) and cadence (3 days) of PS1 MDS make us sensitive to timescales for which BHs (with $M > 10^7 M_{\odot}$) are in the GW-driven regime of orbital decay.

2.3 Pan-STARRS1 Medium Deep Survey

The Panoramic Survey Telescope and Rapid Response System (Pan-STARRS) is a wide-field imaging system designed for dedicated survey observations on a 1.8m telescope on Haleakala, Hawaii, with a 1.4 Gigapixel camera and a 7 deg^2 field of view (Kaiser et al., 2010). The PS1 telescope is operated by the Institute for Astronomy (IfA) at the University of Hawaii and has just completed over 4 yr of operation in 2014 March. We present data from the Medium Deep Survey (MDS), a deep, multi-epoch survey of 10 circular fields distributed across the sky, each $\sim 8 \text{ deg}^2$ in size, whose daily observing cadence in five filters is excellent for studying persistent variable sources, including quasars. The PS1 MDS cadence of observation cycles through the g_{P1} , r_{P1} , i_{P1} , and z_{P1} bands every three nights, with observations in the y_{P1} band close to the full Moon. Due to the poorer time sampling of the y_{P1} observations, we do not use them in this analysis.

2.4 Ensemble Photometry

We began our systematic search for SMBHB candidates among color-selected quasars in the PS1 MD09 field. This is the first MD field that was made available to the PS1 Science Collaboration in the Pan-STARRS Science Interface (PSI) online database. In order to maximize our sensitivity to intrinsic variability, we first applied the technique of differential ensemble photometry. This technique is able to correct for local systematic errors due to variable atmospheric conditions by comparing a

target object with nearby non-variable stars (Bhatti et al., 2010; Honeycutt, 1992). We created a color-selected reference sample and quasar sample by cross-matching point sources ($m < 23$ mag) in the MD09 field with a custom catalog extracted from full-survey deep stacks from PS1 MDS in the g_{P1} , r_{P1} , i_{P1} , z_{P1} , and y_{P1} bands, as well as from observations with the Canada–France–Hawaii Telescope (CFHT) in the u band (S. Heinis et al. 2015, in preparation). We converted all magnitudes to the SDSS photometric system (Tonry et al., 2012b) to take advantage of the SDSS color selection of stars and quasars already available in the literature (Schmidt et al., 2010; Sesar et al., 2007). Figure 2.1 shows the color-color diagrams of the point sources in MD09 selected as quasars and non-variable stars. This query resulted in 8158 reference stars and 316 quasars, each with an average of 350 detections in four filters.

We modified the ensemble photometry software developed by Bhatti et al. (2010) for SDSS to the PS1 data format and ran it on the reference stars. In Figure 2.1 (bottom right panel), we plot the “corrected” magnitude error as a function of mean magnitude compared with the “raw” values before ensemble photometry. The ensemble photometry reduces the measured errors significantly, lowering the error floor from 0.045 to 0.025 mag, and resulting in a 2σ variability threshold of 0.05 mag on the bright end to 0.34 mag on the faint end.

2.5 Selecting Periodic Quasar Candidates

We then applied ensemble photometry to the 316 color-selected quasars and flagged quasars as variable based on their magnitude error relative to their neighbors of a similar brightness; we set 2σ as our criterion for variability and required a variability flag in at least two filters. This selection yielded 168 variable quasars in MD09. Among these color-selected variable quasars, we searched for potential periodic signatures using the Lomb–Scargle (LS) periodogram, a Fourier analysis technique of unevenly spaced data with noise (Horne & Baliunas, 1986; Lomb, 1976; Scargle, 1982). For N_0 data points in the time series spanning a total length of T in units of MJD, we sampled the periodogram at the number of recommended independent frequencies (N_i) from Horne & Baliunas (1986), from $1/T$ to $N_0/(2T)$ (which would be the Nyquist frequency if data were evenly sampled), resulting in a frequency resolution in the periodogram of $\Delta f = (N_0/2 - 1)/(TN_i) \sim 2 \times 10^{-4} \text{ d}^{-1}$. When identifying periodic sources, we took advantage of the redundancy of PS1 MDS monitoring in four filters (g_{P1} r_{P1} i_{P1} z_{P1}), each with a slightly different observing cadence due to weather and scheduling constraints to help filter out false detections from aliasing by requiring that periodogram peaks be coherent across multiple filters; 40 of the 168 variable quasars survived this test.

2.6 Periodic Quasar Candidate PSO J334.2028+01.4075

Among the candidate periodic quasars from our periodogram analysis, here we focus on our most significant detection, PSO J334.2028+01.4075 (J2000). In Figure 2.3, we show its periodogram in four PS1 filters, with the strongest peak marked with a dashed line. We fold each filter light curve on this period (Figure 2.2), and measure the scatter of the residuals from the best-fit sine curve (σ_r). The error of the periodogram peak frequency (δf) and the signal-to-noise ratio of the peak power (ξ) can then be calculated from σ_r and the amplitude of the signal A_0 (Horne & Baliunas, 1986) as $\delta f = \frac{3\sigma_r}{4\sqrt{N_0}TA_0}$ (which gives us an error on the detected period of $\delta P = \delta f/f^2$) and $\xi \equiv A_0^2/(2\sigma_r^2)$, respectively.

The resulting average period across all four filters is $P = 541.8 \pm 15.3$ days, with the highest signal-to-noise ratio in the g_{P1} filter with $\xi = 3.19$, and periodogram peaks in all four filters well above a 1.5×10^{-23} false-alarm probability (corresponding to 10σ) plotted with a dotted line in Figure 2.3. The PS1 data cover 2.6 cycles, just shy of the “rule of thumb” number of cycles (three) for a periodic variation to be apparent to the eye (Press, 1978). From our Monte Carlo simulations of 1000 stochastic Damped Random Walk (Kelly et al., 2009) light curves, we find a false periodic detection rate of 6.3% using our selection criteria from Section 2.5. We further disfavor a false alarm from stochastic quasar variability since the 0.6% of the simulations that successfully mimic the periodic timescale of our candidate have short-timescale variances a factor of ~ 2 larger than expected for the quasar’s luminosity and inferred black hole mass (Section 2.7). Note that there is a secondary

peak in the g_{P1} and r_{P1} periodograms that, if real and not an artifact from the PS1 data sampling, is at twice the primary peak frequency, a signature of $0.05 < q < 0.25$ mass-ratio SMBHBs, which show an accretion rate modulation most closely described by a simple sinusoid (D’Orazio et al., 2013). The amplitude of PSO J334.2028+01.4075’s sinusoidal modulation increases with decreasing wavelength, consistent with the exponential dependence on wavelength found in previous quasar variability studies (*e.g.* MacLeod et al. 2010; Vanden Berk et al. 2004).

PSO J334.2028+01.4075 is a radio-loud quasar (FBQS J221648.7+012427) with an archival spectrum from the FIRST Bright Quasar Survey (Becker et al., 2001). We are also fortunate that this candidate has an archival V-band light curve from CRTS (Drake et al., 2009), which we use to test the persistence of the periodic variation over an extended baseline of 8.5 yr (corresponding to 5.7 cycles). To compare to the CRTS light curve, we convert the PS1 g_{P1} -band light curves to the SDSS system (Tonry et al., 2012b) and then to the Johnson V magnitude using the photometric transformation for quasars from Jester et al. (2005) and an average $g_{P1}-r_{P1} = +0.10$ mag. We had to apply an additional offset of -0.17 mag to the pseudo- V PS1 magnitudes in order to match the average of the CRTS V -band data. Though the photometric errors are relatively large, the CRTS measurements are consistent with those of PS1 during their overlap (Figure 2.4), and have residuals over the entire CRTS baseline from the PS1-fitted sinusoidal model that are Gaussian with a $\sigma = 0.17$ mag that is comparable to the mean photometric error of 0.18 mag.

2.7 Physical Interpretation

We use the width of the quasar’s $C\text{ IV}$ line and its nearby continuum luminosity to make a virial estimate of the black hole mass from [Vestergaard & Peterson \(2006\)](#):

$$\log\left(\frac{M_{\text{BH}}}{M_{\odot}}\right) = \log\left[\left(\frac{FWHM(CIV)}{1000\text{km/s}}\right)^2 \left(\frac{\lambda L_{\lambda}}{10^{44}\text{erg/s}}\right)^{0.53}\right] + 6.66 \quad (2.2)$$

where $\lambda = 1350\text{ \AA}$. The FBQS spectrum, though not publicly available in an electronic format, was measured with a ruler to determine $F_{\lambda,\text{obs}}(1350\text{\AA} (1+z)) \sim 8.5 \times 10^{-17} \text{ ergs s}^{-1}\text{cm}^{-2} \text{ \AA}^{-1}$, and $FWHM(CIV \lambda 1550) \sim 200\text{ \AA}$. The CIV line is symmetric in shape, and its width corresponds to a velocity in the rest-frame of $\sim 12,650 \text{ km s}^{-1}$. We correct for a Galactic extinction of $E(B - V) = 0.0406 \text{ mag}$ ([Schlafly & Finkbeiner, 2011](#)), using the extinction law from [Cardelli et al. \(1989\)](#), to find $L_{\lambda,\text{em}}(1350\text{\AA}) = 4\pi d_L^2 F_{\lambda,\text{obs}} 10^{A_{\lambda}/2.5} (1+z) \sim 9.5 \times 10^{42} \text{ erg s}^{-1}\text{\AA}^{-1}$, where d_L is the luminosity distance assuming $H_0 = 70 \text{ km/s/Mpc}$, $\Omega_m = 0.3$, $\Omega_{\Lambda} = 0.7$, and $k = 0$, and $A_{\lambda} = 0.1790$. This results in a black hole mass of $\log\left(\frac{M_{\text{BH}}}{M_{\odot}}\right) = 9.97$, with a scatter from the uncertainty in the relation of 0.5dex. Applying a mean quasar bolometric correction at 1350\AA of $BC=3.81$ from [Richards et al. \(2006a\)](#), one gets a bolometric luminosity of $L_{\text{bol}} = \lambda L_{\lambda} BC = 4.9 \times 10^{46} \text{ erg s}^{-1}$. Note that this object is also radio loud, with a radio luminosity at the rest-frame frequency of 5 GHz of $\log(L_R(\text{erg s}^{-1})) = 32.8$ from [Becker et al. \(2001\)](#).

Assuming the rest-frame period $P_{\text{rest}} = P_{\text{obs}}/(1+z)$ is on the order of the orbital timescale of the SMBHB, with a caveat that in addition to a strong dependence on mass ratio, there are a range of theoretical predictions for translating P_{rest} to

t_{orb} (*e.g.* MacLeod et al. 2010; Vanden Berk et al. 2004), we then calculate the orbital separation of the binary to be $7_{-4}^{+8}R_s$ ($\sim 0.006_{-0.003}^{+0.007}$ pc), securely placing it in the gravitationally bound regime of a physically viable SMBHB system — a circumbinary accretion disk system capable of maintaining a central cavity, stable to gravitational fragmentation, and in the regime of orbital decay driven by GWs (*e.g.* D’Orazio et al. 2013; Haiman et al. 2009; Kocsis et al. 2012). Also note that since the viscous time scales as r^2 , one could expect to be able to detect modulations in the accretion rate fed by the streams in the circumbinary disk cavity, without being washed out by viscous processes in the “minidisks” around each BH (Roedig et al., 2014). Remarkably, the rest-frame inspiral time for the binary is $t_{\text{insp}} = \frac{5}{256} \frac{c^5}{G^3} \frac{a^4}{M^2 \mu} = 7.0 \text{ yr} (a/7R_s)^4 (M/10^{9.97} M_\odot)^{-3}$ for $q = 0.25$, where $\mu \equiv \frac{M_1 M_2}{M_1 + M_2}$, opening up the possibility for detecting the decay of the orbital period (\dot{P}) with future monitoring, as well as providing a promising target for direct GW detection for pulsar timing arrays (Sesana et al., 2009).

2.8 Discussion and Conclusions

We present the most statistically significant periodically variable quasar candidate from our search in PS1 MD09, PSO J334.2028+01.4075, a radio-loud quasar at $z = 2.060$. We combine an estimate of its black hole mass with its variability timescale (assuming $P_{\text{rest}} \sim t_{\text{orb}}$) to find orbital parameters consistent with model predictions of a stable accreting SMBHB system with a $0.05 < q < 0.25$ in the GW-driven regime (Haiman et al., 2009).

The redshift of this SMBHB candidate coincides with the peak epoch for SMBHB mergers (Volonteri et al., 2003), and its large mass ($M \approx 10^{10} M_{\odot}$) makes it favorable for detection in the GW-driven regime, due to the strong dependence on M of the residence time at a given orbital separation in units of R_s (Haiman et al., 2009). Like the CRTS SMBHB candidate PG 1302–102 reported by Graham et al. (2015a), our SMBHB candidate is also a radio-loud quasar. However, given the shorter rest-frame period of our candidate of 0.5 yr (versus 4 yr in PG 1302–102), it is even more unlikely for its variability to be driven by jet precession, either originating from a single SMBH (Lu & Zhou, 2005) or a binary SMBH (Lobanov & Roland, 2005).

This pilot program in PS1 MD09 is a promising start to our systematic search for periodic variability signatures of SMBHBs amongst the expected ≈ 1000 variable quasars in the full ~ 80 deg² PS1 MDS. At the start of the next decade (~ 2023), the Large Synoptic Survey Telescope (LSST) (Ivezic et al., 2008) will probe a volume several thousand times larger than PS1 MDS, yielding tens of millions of quasars, and potentially thousands of SMBHBs periodically varying on the timescale of years, fated to coalesce.

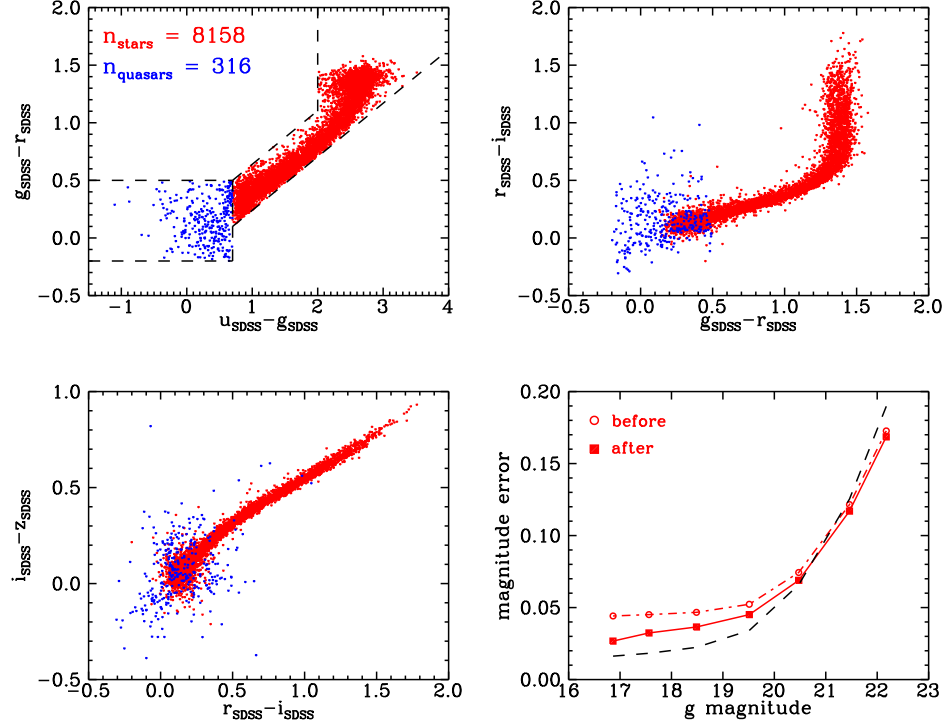


Figure 2.1: Color-color diagrams used to select point sources in MD09 for the 8158 point sources in the reference star sample (red) and 316 point sources in the quasar sample (blue). Photometry is measured from the CFHT+PS1 catalog and converted to the SDSS system. Dashed lines show the color selection boundaries. The stellar color-color selection box was chosen to avoid RR Lyrae stars, which are intrinsically variable. Bottom right panel: observed standard deviation of the reference sample of non-variable stars before and after applying the technique of ensemble photometry (open circles and filled squares, respectively), compared to the Poisson error expected from the reported PS1 flux errors (black dashed lines).

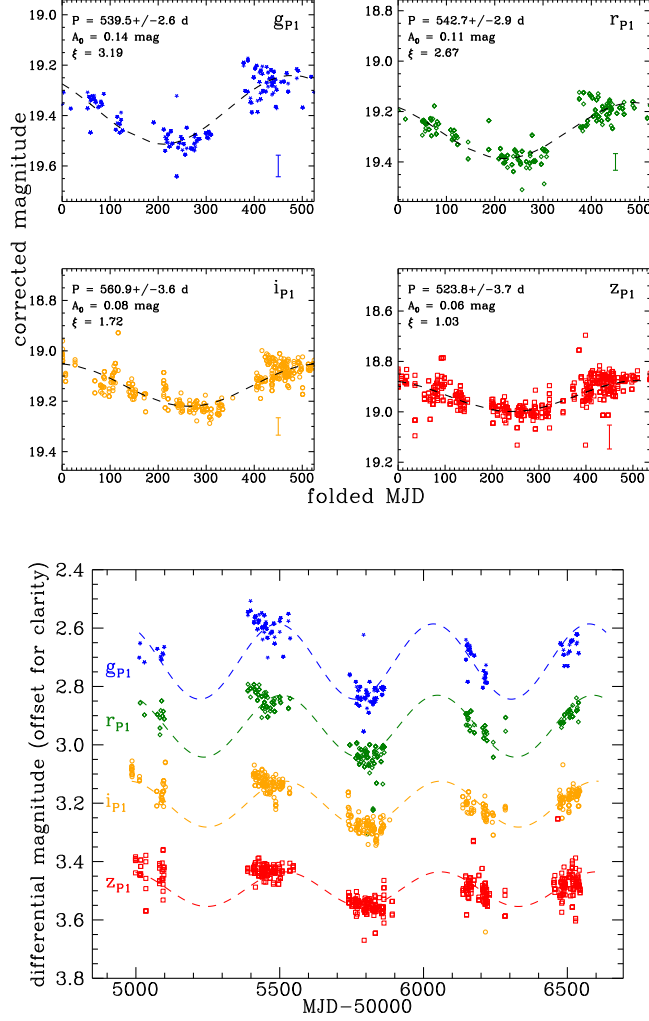


Figure 2.2: Upper panels: sinusoidal fit to the folded PS1 light curve of PSO J334.2028+01.4075 in four filters, with the error bar indicating the typical photometric error for an object of similar brightness in that filter. The period corresponding to the peak of the periodogram and its error bar, the amplitude of the fitted sine wave, and the signal-to-noise ratio of the peak power are each labeled. Lower panel: sinusoidal fit plotted over the complete PS1 light curves in the g_{P1} r_{P1} i_{P1} and z_{P1} bands. The data used to create this figure are available.

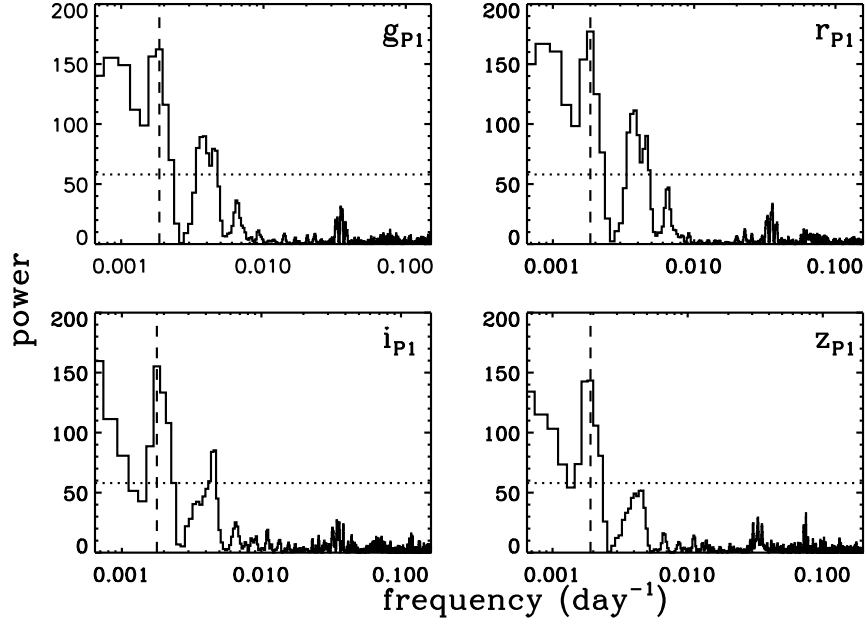


Figure 2.3: Our automated LS periodogram routine selects periodically variable candidates by requiring that the strongest peak is detected at the same frequency in at least three filters. This quasar candidate, PSO J334.2028+01.4075, was selected through this method and had the periodogram peak with the highest signal-to-noise ratio of all of our candidates. The dashed lines mark the strongest peak in each filter. The dotted line corresponds to a false-alarm probability of 1.5×10^{-23} , or 10σ .

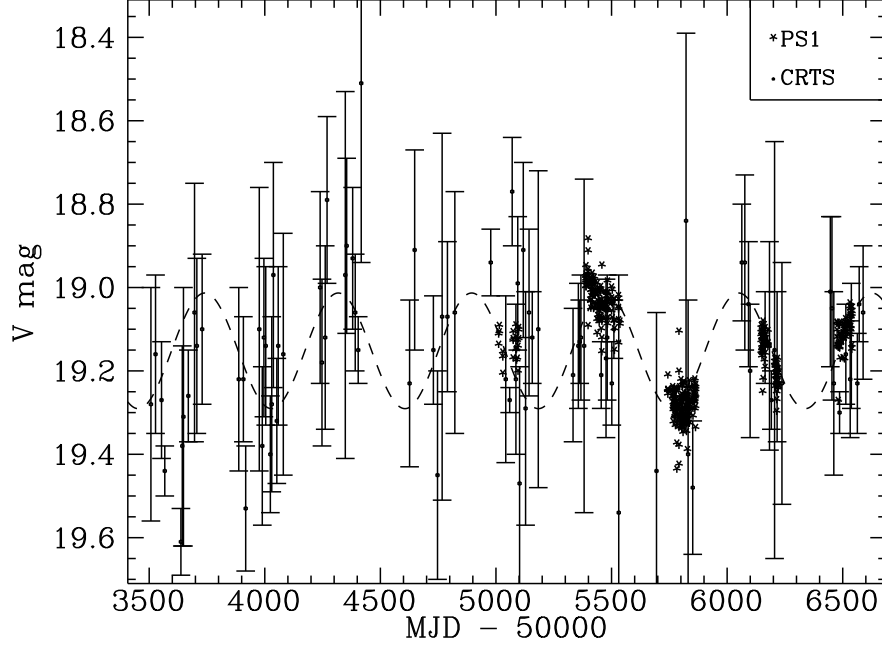


Figure 2.4: PS1 light curve (asterisks) converted to the V band to compare to the archival CRTS light curve (dots with error bars). The CRTS data points are binned in one-day intervals, with the error bars measured from the standard deviation in the bin and not including data points with a photometric error greater than 0.25 mag or nights with less than three measurements. This results in 34/113 nights of data being thrown out. The CRTS measurements are overall consistent with the PS1 light curve and the sine fit to the PS1 light curve (dashed curve).

Chapter 3: A Systematic Search for Periodically Varying Quasars in Pan-STARRS1: An Extended Baseline Test in Medium Deep Survey Field MD09

3.1 Introduction

Supermassive black holes (SMBHs) appear to be at the centers of most, perhaps all, massive galaxies (*e.g.* [Kormendy & Richstone 1995](#)). Thus, when two massive galaxies merge in the Λ CDM Universe, it is expected that their nuclei will form a supermassive black hole binary (SMBHB; *e.g.* [Springel et al. 2005](#)). As the binary coalesces, the early stage of its orbital decay is driven by exchanging angular momentum with the circumbinary gas disk through viscosity; at smaller separations ($a < 1$ pc), its orbital decay becomes more dominated by gravitational wave (GW) radiation (*e.g.* [Begelman et al. 1980](#)).

However, sub-parsec separation SMBHBs at cosmological distances are too compact to resolve with current, or even future, telescopes. Indirect searches so far, therefore, have been focused on spectroscopy, looking for offset broad lines that suggest two broad line emission regions, each likely associated with each black hole in the binary system ([Boroson & Lauer, 2009](#)), or offset or shifted peak of the broad

line region (*e.g.* [Dotti et al. 2009](#); [Eracleous et al. 2012](#)).

Another observational aspect of SMBHBs, however, was much under-exploited until recently — their potential optical variability. One of the first sub-parsec SMBHB candidates identified via its variability was OJ 287 ([Sillanpaa et al., 1988](#)), which showed quasi-periodic optical outbursts at intervals of 12 years, with the physical interpretation of the burst being the secondary black hole passing through the accretion disk of the primary (*e.g.* [Lehto & Valtonen 1996](#); [Valtonen et al. 2011, 2008](#)). More recently, another sub-parsec SMBHB candidate, PG 1302–102 ([Graham et al., 2015a](#)), was discovered by the Catalina Real-time Transient Survey (CRTS; [Drake et al. 2009](#)). Its V -band light curve can be fitted to a sinusoidal function with period of 1,884 days and amplitude of 0.14 mag. A physical interpretation of PG 1302–102’s periodic variability is relativistic Doppler boosting ([D’Orazio et al., 2015](#)): in this scenario, where the luminosity is dominated by the steadily accreting secondary black hole and the system is viewed at a high inclination angle, emission from the minidisk of the secondary is Doppler-boosted as the black hole orbits at a moderately relativistic speed (along the line of sight).

Another possible scenario that could give rise to periodic variability is modulated mass accretion in the system. Simulations of an SMBHB embedded in a circumbinary disk show that although the binary tidal torque clears and maintains a low gas density cavity at radius $< 2a$ (where a is the binary separation), materials can penetrate the cavity through a pair of streams and be accreted onto the binary. These simulations have the similar results that for a mass ratio $0.01 < q < 1$ — as expected in the merger of two massive galaxies — mass accretion through

the circumbinary disk is strongly modulated as a result of the binary’s orbital motion within the circumbinary disk, including two-dimensional (2D) hydrodynamical (MacFadyen & Milosavljević, 2008), 3D Newtonian magnetohydrodynamical (MHD; Shi et al. 2012) and Post-Newtonian MHD (Noble et al., 2012) for an equal mass binary, and general relativistic (GR) MHD (Gold et al., 2014) and 2D hydrodynamical simulations (D’Orazio et al., 2013) for various mass ratios. In these simulations, the accretion rate varies on a time scale that is on the order of the binary orbital time scale, which is in turn a function of the total black hole mass and orbital separation by virtue of Kepler’s law. Assuming that luminosity tracks mass accretion of the circumbinary disk, the former should then vary as the latter varies. For a typical black hole mass of $10^7 M_\odot$ and typical separation $10^3 R_s$, the orbital period is on the order of \sim year, an observationally feasible time scale for current time-domain surveys: $t_{\text{orb}} = 0.88 \text{ yr} \left(\frac{M}{10^7 M_\odot} \right) \left(\frac{a}{10^3 R_s} \right)^{3/2}$ (where R_s is the Schwarzschild radius: $R_s = 2GM/c^2$).

These theoretically explored variability signatures of an SMBHB, as well as encouraging predictions for the detection rates of periodically varying quasars from SMBHBs in a cosmological context (Haiman et al., 2009), motivated several recent systematic searches in large optical time-domain surveys with a temporal baseline of several years — Graham et al. (2015a,b), with the CRTS; Charisi et al. (2016), with Palomar Transient Factory (PTF) and additional data from intermediate-PTF and CRTS; Zheng et al. (2016), with the Sloan Digital Sky Survey (SDSS) and CRTS; and Liu et al. (2015), with the Pan-STARRS1 Medium Deep Survey (MDS).

In our pilot study (Liu et al. 2015, hereafter L15), we performed a systematic

search for SMBHB candidates in MDS’s MD09 field and reported our first significant detection of such a candidate, PSO J334.2028+1.4075. As reported in L15, PSO J334.2028+1.4075 has a coherent period of $P = 542 \pm 15$ days in g_{P1} r_{P1} i_{P1} z_{P1} filters, corresponding to almost 3 cycles of variation that is well fitted to a sinusoidal function. It also has an archival V -band light curve from CRTS (Drake et al., 2009). Even though the photometric precisions are not comparable, the CRTS light curve is consistent (in the residual sense) with the PS1 only (PV1) sinusoidal fit over ~ 9 years, or ~ 6 cycles. It is also a radio loud quasar ($R = \log(f_{5\text{GHz}}/f_{2500\text{\AA}}) = 2.30$; Becker et al. 2001) from the VLA FIRST catalog (FIRST J221648.6+012427; White et al. 1997).

Since then, we have repeated our analysis of MD09 with data Processing Version 2 (PV2) which was made available late-2014 and includes extra data from the final phase of the PS1 survey (Figure 3.1). We find three periodic quasar candidates that satisfy our selection criteria: a coherent period in at least three filters, an S/N for a sinusoidal fit of > 3 in at least one filter, and a variation over at least 1.5 cycles. In addition, we use extended baseline data (from archival and new monitoring observations) to test the persistence of our periodic candidates over 5 – 12 cycles. Recently, it has been pointed out by Vaughan et al. (2016) that the intrinsic red noise (increasing power at lower frequencies) characteristic of quasar variability can easily mimic periodic variability over a small number of cycles, and they emphasize the importance of demonstrating persistence of periodicity over > 5 cycles.

This paper thus presents our detailed analysis with MD09 PV2 and is organized as follows. In Section 3.2 we introduce the time domain data set used in this study:

MD09 from the Pan-STARRS1 MDS. In Section 3.3 we describe our methods of variability selection and periodicity search; we also discuss our biases in selecting variable active galactic nuclei (AGNs) in a flux-limited survey like PS1 MDS. In Section 3.4, we test the persistence of the candidates’ periodicity with archival light curves and follow-up imaging. In Section 3.5, we measure the black hole mass of binary candidates and calculate their inferred binary parameters. Finally, in Section 3.6, we conclude with implications for searches for periodic quasars in a large time-domain survey. Throughout this paper, we adopt cosmological parameters for a flat universe: $\Omega_m = 0.3$, $\Omega_\lambda = 0.7$, $H_0 = 70$ km/s/Mpc.

3.2 The Pan-STARRS1 Medium Deep Survey

The Panoramic Survey Telescope and Rapid Response System (Pan-STARRS; Kaiser et al. 2010) is a multi-filter imaging system designed for sky surveys on a 1.8 m telescope on the summit of Haleakala in Maui, Hawaii, with a 1.4 gigapixel camera and a 7 deg² field of view. The Pan-STARRS1 (PS1) telescope is operated by the Institute for Astronomy (IfA) at the University of Hawaii and completed its 4.2 years of operation in the spring of 2014. $\sim 25\%$ of the PS1 telescope time was spent on the MDS, a deep, time domain survey of 10 circular fields distributed across the sky, totaling ~ 80 deg², chosen for their overlap with extragalactic legacy survey fields that have multi-wavelength corollary data. The PS1 MDS cadence typically cycles through the g_{P1} , r_{P1} , i_{P1} , and z_{P1} bands every three nights during the 6–8 months when the field is visible, observing in g_{P1} and r_{P1} on the same night and in

the y_{P1} band close to the full Moon (though y band observations were not used in our study due to the poorer sampling). Nightly observations consist of eight 113 s ($g_{P1} r_{P1}$) or 240 s ($i_{P1} z_{P1} y_{P1}$) exposures (Tonry et al., 2012a); over the course of MDS, each object is observed ~ 300 times to a 5σ (*i.e.* where $\Sigma = 0.217$ mag in Figure 3.3) limiting magnitude of ~ 22.5 mag in $g_{P1} r_{P1} i_{P1}$ and ~ 22.0 mag in z_{P1} in a single exposure. Individual exposures can be combined into nightly stacks or full-survey-depth “deep” stacks, to reach much deeper limits of ~ 23.5 mag and ~ 25 mag, respectively (in the g_{P1} , r_{P1} , and i_{P1} bands).

The PS1 photometric calibration includes a combination of “absolute” calibration, which translates the number of photons detected to the physical unit of magnitude, and “relative” calibration, which removes variations due to the telescope system and atmosphere over the course of the survey. The PS1 absolute photometric calibration is accomplished by observing photometric standard stars from HST’s Calspec catalog (Tonry et al., 2012b), as part of the Image Processing Pipeline (IPP; Magnier 2006). The relative calibration is based on the algorithm of Padmanabhan et al. (2008) which is known as “Ubercalibration” (Ubercal). The PS1 Ubercal (Schlafly et al., 2012) uses multiple observations of the same non-intrinsically variable sources on photometric nights and demands that the observed magnitude does not change over time and thereby minimizes variations in the zero point. PS1 data are further calibrated through “Relphot” (Magnier et al., 2013), which solves for an additional zero point offset for each exposure, using the Ubercal solutions as a starting point.

In L15, we employed a similar technique adapted from Bhatti et al. (2010)

(“ensemble photometry”; [Honeycutt 1992](#)) which implements the **ENSEMBLE**¹ software package in our attempt to achieve precision photometry with MDS. We constructed an “ensemble” of point sources near each target object in a $\sim 0.1 \text{ deg} \times \sim 0.1 \text{ deg}$ field and ran the algorithm iteratively to obtain a least-squares solution that *locally* reduces the scatter for all observations of each source over the course of the survey. However, since the PS1 data products had already been Ubercaled, the overall improvement in our control sample of stars in L15 or our re-analysis with PV2 was not significant enough to justify this time-intensive procedure; thus we do not apply the method of ensemble photometry in the analysis presented in this paper.

3.3 Methods

3.3.1 Sample Selection

We first extracted from the PS1 Science Archive all sources from MD09 that matched the following criteria: 1) they are point sources selected as deep stack $\text{mag}_{\text{psf}} - \text{mag}_{\text{Kron}} < 0$ ² that have a good point spread function (PSF) quality factor from the IPP (**psfQF** > 0.85), 2) they have **stackPSFMag** < 23 mag, 3) they have at least five detections in each filter, and 4) masks were applied to exclude bad and poor detections (Table 3.1). The query resulted in $\sim 40,000$ point sources, for which we get PSF magnitudes, each with an average of ~ 300 detections in each of the

¹<http://spiff.rit.edu/ensemble/>

²Since the Kron radius captures more flux from an extended source than the PSF profile, while for a point source its Kron magnitude should be close to its PSF magnitude.

four filters.

For our color-selection of quasars and stars, we use a catalog of Kron magnitudes extracted from deep stack images in the g_{P1} , r_{P1} , i_{P1} , z_{P1} , y_{P1} bands from PS1 MDS as well as in the u_{CFHT} band from the Canada-France-Hawaii Telescope (CFHT) (Heinis et al. 2016b, hereafter the PS1×CFHT catalog). We use the PS1×CFHT catalog star/galaxy classification, which was determined using a machine learning method of support vector machine (SVM) that was trained on an HST/ACS sample of stars and galaxies and has a completeness of 88.5% for stars $i_{P1} < 21$ mag, or 97.4% of all objects down to $i_{P1} = 24.5$ mag (Heinis et al., 2016a). We then cross-match (using a $1''$ radius) our PS1 Science Archive point sources with point sources in the PS1×CFHT catalog with $r_{P1} < 23$ mag (where the star/galaxy separation is the most reliable), and within a 1.59 deg radius from the center of the MD09 field (to avoid edge effects).

For the $\sim 15,000$ cross-matched point sources, we then converted their CFHT u^3 and PS1 $g r i z$ (Tonry et al., 2012b) band magnitude to the SDSS magnitude system

$$u_{SDSS} = (u_{CFHT} - 0.241 g_{SDSS})/0.759$$

$$g_{SDSS} = 0.014 + 0.162 (g_{P1} - r_{P1}) + g_{P1}$$

$$r_{SDSS} = -0.001 + 0.011 (g_{P1} - r_{P1}) + r_{P1}$$

$$i_{SDSS} = -0.004 + 0.020 (g_{P1} - r_{P1}) + i_{P1}$$

³<http://www.cadc-ccda.hia-ihp.nrc-cnrc.gc.ca/en/megapipe/docs/filt.html>

$$z_{\text{SDSS}} = 0.013 - 0.050 (g_{\text{P1}} - r_{\text{P1}}) + z_{\text{P1}} \quad ,$$

and selected those that have the following quasar colors for their clean separation from stars (Sesar et al., 2007):

$$\begin{aligned} u_{\text{SDSS}} - g_{\text{SDSS}} &< 0.7 \\ -0.2 &< g_{\text{SDSS}} - r_{\text{SDSS}} < 0.5 \quad . \end{aligned}$$

We also select stars for our control sample, carefully avoiding the region occupied by RR Lyrae variables ($u_{\text{SDSS}} - g_{\text{SDSS}} \sim 1.15$; Sesar et al. 2007). The color diagrams of selected quasars and stars are shown in Figure 3.2. In order to obtain our variability detection limit (Section 3.3.2), we plot their error vs. magnitude relation for our star sample in Figure 3.3 and fit the binned relation in each filter to a parabola:

$$\sigma(g) = 2.64372 - 0.293112 g + 0.00818841 g^2 \quad (3.1)$$

$$\sigma(r) = 2.39328 - 0.267030 r + 0.00749830 r^2 \quad (3.2)$$

$$\sigma(i) = 2.13028 - 0.237271 i + 0.00666299 i^2 \quad (3.3)$$

$$\sigma(z) = 2.77188 - 0.309921 z + 0.00874017 z^2 \quad . \quad (3.4)$$

Table 3.1: PS1 Quality Flags Used in the Query

| Flag Name | Flag Name |
|-----------------|------------------|
| FAIL | POOR |
| PAIR | SATSTAR |
| BLEND | BADPSF |
| DEFECT | SATURATED |
| CR_LIMIT | EXT_LIMIT |
| MOMENTS_FAILURE | SKY_FAILURE |
| SKYVAR_FAILURE | BELOW_MOMENTS_SN |
| BLEND_FIT | SIZE_SKIPPED |
| PEAK_ON_SPIKE | PEAK_ON_GHOST |
| PEAK_OFF_CHIP | |

3.3.2 Variability Selection

To select intrinsic variables from our quasar sample, we perform a variability selection in such way that systematic effects local to the field are minimized: we plot the magnitude error in terms of standard deviation of the light curve as a function of magnitude for each object within $\Delta\text{R.A.} = 0.5$ deg and $\Delta\text{decl.} = 0.5$ deg from each color-selected quasar. Each of these “ensembles” contains ~ 1000 point sources. We calculate the median value for each magnitude bin, while avoiding the bins with less than five stars, and interpolate linearly between the bin centers. The intrinsic vari-

ables have a significantly higher magnitude scatter than stars of the same brightness and thus appear as outliers that deviate from the error vs. magnitude trend established by the majority of objects. We iteratively remove variables from the linear interpolation, and after three iterations, those that passed the final 2σ detection threshold (have at least twice the magnitude error than the linear interpolation) are tagged as variables (Figure 3.4). Our piece-wise interpolation method is adapted from the variability selection procedure in **ENSEMBLE** and gives better results than the parabolic fitting method in the previous version that was applied in our analysis in L15.

Of the 670 quasars processed through this stage, we flag variables independently in each filter, and further require a variability flag in at least two filters. To compare our quasar sample with previous studies, we calculate their intrinsic variability σ_{int} by putting in quadrature the standard deviation of the light curve Σ and the photometric error σ : $\sigma_{\text{int}} = \sqrt{\Sigma^2 - \sigma^2}$ (Sesar et al., 2007) for $\Sigma > \sigma$ and $\sigma_{\text{int}} = 0$ otherwise, where σ is the magnitude-dependent photometric error from Equation 3.1–3.4. We find the number fraction of quasars varying at the $> \sigma_{\text{int}}$ level qualitatively agrees with the results from SDSS Stripe 82 (S82) quasars in Sesar et al. (2007) at $\sigma_{\text{int}} > 0.06$ mag, where $\sim 60\%$ of quasars vary at or above that level, compared to a control sample of stars for which the fraction is $< 5\%$ (Figure 3.5). The lower quasar variability fraction that we find for smaller variability amplitudes is likely due to our factor of ~ 2 larger photometric errors compared to S82 ($\sigma(g) > 0.04$ mag vs. $\sigma(g) > 0.018$ mag).

Table 3.2: QLF Model Values Used in Equation 3.5 – 3.8

| QLF Model | α | β | M_i^* | k_1 | k_2 | $\log(\Phi^*)$ |
|--------------------------|----------|---------|---------|--------|--------|----------------|
| PLE ($0.3 < z < 2.2$) | -1.16 | -3.37 | -22.85 | 1.241 | -0.249 | -5.96 |
| LEDE ($2.2 < z < 3.0$) | -1.29 | -3.51 | -26.57 | -0.689 | -0.809 | -5.93 |

3.3.3 Selection Bias

To investigate the possible biases in our variability selection in a flux-limited survey, we simulated ~ 9000 quasars whose population is derived from the quasar luminosity function (QLF). The QLF is defined as the number of quasars per co-moving volume per unit magnitude and is described by a broken power law:

$$\Phi(M, z) = \frac{\Phi^*}{10^{0.4(\alpha+1)[M-M^*(z)]} + 10^{0.4(\beta+1)[M-M^*(z)]}} \quad , \quad (3.5)$$

where M_* is the characteristic break absolute magnitude, and α and β are the slopes of the QLF at the faint end and bright end, respectively. At lower redshifts ($0.3 < z < 2.2$), the QLF is described by a pure luminosity evolution (PLE) model, where the characteristic number density Φ^* remains constant while M^* evolves with redshift quadratically (in i band):

$$M_i^*(z) = M_i^*(z=0) - 2.5(k_1 z + k_2 z^2) \quad . \quad (3.6)$$

At higher redshifts ($z > 2.2$), it is necessary to model the QLF as the results of luminosity evolution and density evolution (LEDE), where Φ^* and M^* evolve

independently with redshift:

$$\log \Phi^*(z) = \log \Phi^*(z = 2.2) - c_1(z - 2.2) \quad (3.7)$$

$$M_i^*(z) = M_i^*(z = 2.2) - c_2(z - 2.2) \quad . \quad (3.8)$$

We adopt the values for the constants (Table 3.2) given in [Ross et al. 2013](#), which expanded the redshift range in previous QLF studies (*e.g.* [Richards et al. 2006b](#)) to $0.3 < z < 3.5$.

In each redshift bin of size 0.4 from $z = 0.3 - 3.0$, we integrate over the absolute magnitude range ($-14 < M_i < -30$ mag, $\Delta M_i = 1$ mag) and use the cosmology calculator by [Wright \(2006\)](#) to calculate the co-moving volume of each shell from z . From this quasar redshift distribution, we then populate each absolute magnitude bin for each redshift according to the $\Phi(M, z)$. To convert absolute magnitudes at different redshifts to the observed frame, it is necessary to apply the K correction: $m = M_{z=2} + \text{distance modulus} + K(z)$, where we adopt the values for $K(z)$ from [Richards et al. \(2006b\)](#). We also converted the absolute magnitude at $z = 2$ in the QLF to $z = 0$: $M_{z=0} = M_{z=2} + 0.596$, assuming a constant quasar spectral power law index of $\alpha = -0.5$ ([Richards et al., 2006b](#)).

With a distribution of quasars in redshifts and absolute magnitudes, we then adopt the empirical relations from [Heinis et al. \(2016b\)](#) to calculate the expected variability amplitude given the quasar's (rest frame) absolute magnitude. Using difference imaging of ~ 1000 variability selected AGNs from PS1 MDS, [Heinis et al. \(2016b\)](#) measured the anti-correlation between fractional flux variability and the

AGN luminosity in the g_{P1} r_{P1} i_{P1} z_{P1} bands, and here we convert their relations to the magnitude space:

$$\log \left(\frac{\Delta f}{f} \right)_g = 0.17 M_g + 3.40 \quad (3.9)$$

$$\log \left(\frac{\Delta f}{f} \right)_r = 0.18 M_r + 3.64 \quad (3.10)$$

$$\log \left(\frac{\Delta f}{f} \right)_i = 0.20 M_i + 4.02 \quad (3.11)$$

$$\log \left(\frac{\Delta f}{f} \right)_z = 0.20 M_z + 4.07 \quad , \quad (3.12)$$

where $\log(\Delta f/f)$ was measured from the maximum flux on the difference images over the course of PS1 MDS, and the absolute magnitude M of the AGN was derived from SED fitting (Heinis et al., 2016b).

We calculate the expected fractional flux variability $\log(\Delta f/f)$ from Equations 3.9 – 3.12 and convert to Δm : $\Delta m = 2.5 \log[1 + 10^{\log(\Delta f/f)}]$. Finally, we scale up to the expected variability amplitude in its rest frame wavelength using the relation from Vanden Berk et al. (2004): $v(\lambda) = 0.616 \exp(-\lambda_{\text{rest}}/988\text{\AA}) + 0.164$ (where v is variability amplitude measured in terms of “structure function,” also in units of magnitude). To estimate the variability detection threshold for simulated quasars, we calculate the expected photometric errors σ for a given quasar’s apparent magnitudes m in the four PS1 filters from Equations 3.1 – 3.4. We adopt average quasar colors of $g_{\text{P1}} - r_{\text{P1}} = 0.14$ mag, $r_{\text{P1}} - i_{\text{P1}} = 0.15$ mag, and $i_{\text{P1}} - z_{\text{P1}} = 0.08$ mag from our sample of PS1×CFHT quasars in Figure 3.2 as a proxy for our color selection. Note that this color box is a valid assumption for quasars at $z < 3$ (Richards et al., 2002). Next, we apply the same magnitude cut as our PS1 quasar

sample ($r < 23$ mag). And finally, we assume that $\Sigma = 0.023 + 0.27 \Delta m$, the average empirical relation we found for our MD09 variable quasar sample, and using the same variability selection criteria as described in Section 3.3.2, a quasar varying at $\Sigma > 2\sigma$ level in any and at least two filters is flagged in our simulation as a variable.

The redshift, absolute magnitude, and apparent magnitude distributions of the “variable” simulated quasars are compared with the “visible” simulated quasars ($m < 23$ mag) in Figure 3.7. Among the 924 “visible” quasars ($m < 23$ mag), and assuming all obey the Heinis et al. (2016b) relation, 106 (or 11.5%) are selected as “variables,” comparable to the observed variable quasar fraction of 15.5% we find in the MD09 sample (see Table 3.3), while both the “visible” and “variable” samples have similar apparent magnitude distributions with MD09 quasars (Figure 3.6). We find that in a sample of normal quasars or AGNs, our 2σ variability selection is biased toward brighter quasars ($m < 21$ mag) at lower redshifts ($z < 1$), with a relatively flat distribution in luminosity ($-21 \text{ mag} > M > -27 \text{ mag}$). Understanding this selection bias will be important in calculating the volume density of SMBHB candidates in our final sample.

3.3.4 Selecting Periodic Quasar Candidates

We then began to search for potential periodic signatures using the Lomb-Scargle (LS) periodogram, a Fourier analysis technique for unevenly spaced data with noise (Horne & Baliunas, 1986; Lomb, 1976; Scargle, 1982). For N_0 data points in the time series spanning a total length of T in unit of days, we sampled

the periodogram at N_i independent frequencies (Horne & Baliunas, 1986) from $1/T$ to $N_0/(2T)$ (which would be the Nyquist frequency if data were evenly sampled); the resolution of the periodogram is thus $\Delta f = (N_0/2 - 1)/(TN_i)$. Plotting power as a function of f for all test frequencies, the dominant peak at frequency f or period $P = 1/f$ then signals a significant variation at that frequency or period.

When identifying periodic sources from their periodogram peaks, we also took advantage of the redundancy of PS1 MDS monitoring in four filters (g, r, i, z), each with a slightly different observing cadence due to weather and technical downtime, to help filter out false detections by requiring periodogram peaks are coherently detected (within a 10% error) in at least three filters. In each filter, the error of the peak due to noise can further be calculated as $\Delta f = 3\sigma_r/(4\sqrt{N_0}TA_0)$ (Horne & Baliunas, 1986; Kovacs, 1981) — where we calculate A_0 as the best-fit sinusoidal amplitude of the light curve phase-folded on the averaged period \bar{P} and σ_r as the standard deviation of residuals after subtracting the signal from the light curve — which gives us an error on the detected period: $\delta P = \delta f/f^2$. The total uncertainty of the detected period is calculated by putting the theoretical and measured errors in quadrature: $(\Delta P)^2 = (\sqrt{\sum \delta P_i^2}/4)^2 + \sum (P_i - \bar{P})^2/(N - 1)$ where $i = 1 \dots N$ is the index of the coherent filter.

We calculate the S/N ratio of the sinusoidal fit as $\xi = A_0^2/(2\sigma_r^2)$, where σ_r is the standard deviation of the model-fit residuals (Horne & Baliunas, 1986). We mask any outliers that deviate from the mean by more than 4.5σ and require that candidates have $\xi > 3$ in at least one filter. Finally we require at least 1.5 cycles of variation, in accordance with similar studies (Charisi et al., 2016; Graham

et al., 2015b); this limit on the maximum allowed period is also justified since spurious periods are oftentimes found on a timescale close to the total data length (MacLeod et al., 2010). Our selection leaves three candidate periodic quasars in MD09 (Table 3.3). Their periodograms in g_{P1} r_{P1} i_{P1} z_{P1} are shown in Figure 3.8, and their complete PS1 light curves are presented in Figure 3.9. Note that in all three periodograms, variability power increases with lower frequency, which is a characteristic of red noise and a cause for concern in searching for periodicity. It is thus important to understand the false-alarm rate due to red noise and further test the sinusoidal model with extended baseline data (see discussion in Section 3.4.3).

3.4 Extended Baseline Photometry

Historically, there have been claims of (quasi-) periodicity on a number of AGNs, but they failed to withstand re-analyses or follow-up observations (see *e.g.* review by Vaughan & Uttley 2006). In the case of searching for light curve periodicity with a Fourier method, a finite temporal baseline makes the observer highly susceptible to “red noise leak” (see *e.g.* review by Press 1978 on red noise), where low frequency variations are transferred to the sampled high frequencies for objects with “red” power spectra of increasing power at low frequencies, such as AGNs and X-ray binaries.

Fortunately, all three of our candidates have extended baseline photometry, either from the archival database or our ongoing imaging campaign (Table 3.5), giving us an advantage of testing the persistence of their periodic behavior by extending

the baseline to $\sim 2 - 3$ times the length of PS1 MDS with comparable photometric precision.

Table 3.3: MD09 by the Numbers

| Category | Number |
|--|--------|
| PS1 point sources | 40,488 |
| PS1 \times CFHT quasars | 670 |
| PS1 \times CFHT variable quasars | 104 |
| Variable quasars with coherent periodogram peaks | 77 |
| Candidates with $\xi > 3.0$ in at least one filter | 6 |
| Candidates with $N_{\text{cycle}} > 1.5$ | 3 |

Table 3.4: PS1 Mean Magnitudes and Variability Amplitudes of Periodic Quasar Candidates

| PS1 Designation | m (g,r,i,z) | A_0 (g,r,i,z) |
|----------------------|------------------------------|--------------------------|
| PSO J333.0298+0.9687 | (21.42, 20.94, 20.96, 20.95) | (0.68, 0.51, 0.53, 0.39) |
| PSO J333.9832+1.0242 | (18.97, 18.85, 18.79, 18.57) | (0.11, 0.10, 0.09, 0.07) |
| PSO J334.2028+1.4075 | (19.38, 19.28, 19.14, 18.94) | (0.13, 0.11, 0.08, 0.06) |

3.4.1 Follow-up Imaging

We have an on-going observing program at the Discovery Channel Telescope (DCT) in Happy Jack, Arizona, to further monitor candidate PSO J334.2028+1.4075 with its Large Monolithic Imager (LMI) in g_{SDSS} r_{SDSS} i_{SDSS} z_{SDSS} filters (Table 3.5). Here we present data from four observing runs on UT 2015 May 28, 2015 September 17 and 19, 2016 May 15, and 2016 July 10.

Each observation had five exposures (taken in a dither pattern) in each filter on UT 2015 May 28 ($5 \times 50\text{s}$), UT 2015 September 17 (g_{SDSS} r_{SDSS} i_{SDSS} , $5 \times 50\text{s}$) and 19 (z_{SDSS} , $5 \times 50\text{s}$), UT 2016 May 15 ($5 \times 100\text{s}$), and UT 2016 July 10 ($5 \times 100\text{s}$). The images were reduced with standard IRAF routines, astrometry-corrected with SCAMP (Bertin, 2006), and co-added with Swarp (Bertin et al., 2002). For z_{SDSS} band images which are affected by fringe patterns, we constructed a master fringe map from all z band images (with different telescope pointings) taken on one night using the IDL function `create_fringes` (Snodgrass & Carry, 2013). Combining with a series of “control pairs” which mark the positions of adjacent bright and dark fringes in the map, we then subtracted a scaled fringe map from the image using the IDL function `remove_fringes` (Snodgrass & Carry, 2013).

Using SExtractor (Bertin & Arnouts, 1996), we performed aperture photometry on the co-added image, with the aperture radius used in each filter being the typical full-width at half-maximum (FWHM) of the image and produced a catalog of detections in the LMI’s $12'.3 \times 12'.3$ field of view. We then cross-matched the catalog using a $1''$ radius with all the point sources (`type = “star”`) that are within

a 6' radius from the target quasar with clean photometry (`clean` = 1) from the SDSS catalog. We excluded very bright objects ($m < 16$ mag) to avoid saturated detections on the LMI images, and on the cloudy night (UT 20150917) and on all z band images, we also constrained the fitting to the locus where $m < 21$ mag. We iteratively removed outliers that systematically deviate from the residual fit by more than 0.2 mag (for $m < 22$ mag only) and fitted a linear function to the PSF magnitude `psfMag` vs. the `SExtractor` instrumental magnitude `mag_aper` relation (we exclude the target quasar, which is variable, from fitting). Each residual plot was also visually inspected to confirm a good fit.

The magnitude error was calculated by taking the standard deviation of the residuals in the $\Delta m = 0.5$ mag vicinity of the target quasar. Finally, we converted the LMI photometric data to the PS1 magnitude for direct comparison with the light curves from MDS.

In their quasar variability study, [Morganson et al. \(2014\)](#) pointed out there are non-zero, albeit small, offsets for quasars after converting to PS1 magnitudes from the SDSS system. They adopt a third-order polynomial (derived for main sequence stars) to convert from SDSS to PS1 and add an additional average offset to correct for the color-dependent difference between the magnitudes. Since the [Tonry et al. \(2012b\)](#) filter transformations were also derived for stars (from synthetic magnitudes of stellar SEDs), we have the following options to correct between the SDSS and PS1 magnitudes in our light curves: (1) adopt the [Tonry et al. \(2012b\)](#) relation without any additional offset or correction; (2) adopt the [Morganson et al. \(2014\)](#) filter offsets; (3) calculate redshift-dependent synthetic magnitudes (and thus

offsets) from a composite quasar spectrum, where we redshift the composite quasar spectrum from [Vanden Berk et al. \(2001\)](#) to the respective redshift of the candidate quasar and convolve it with the SDSS and PS1 filter sensitivity curves (airmass = 1.3 and 1.2, respectively) to calculate the synthetic magnitude in the respective bandpass and therefore the $m_{\text{P1}} - m_{\text{SDSS}}$ filter offset for each target.

Even though we eventually adopted our redshift-dependent synthetic quasar correction as the most generic method, we note that the difference between the conversion equations are small (~ 0.01 mag), and, for quasars varying at the > 0.1 mag level, as our candidates are, the different choices of filter conversion are unlikely to significantly change our conclusions with regard to the persistence of the variation.

3.4.2 Pre-PS1 Archival Photometry

We retrieved pre-PS1 archival SDSS S82 PSF light curves in g_{SDSS} r_{SDSS} i_{SDSS} z_{SDSS} from SDSS-III DR12 ([Alam et al., 2015](#)). The S82 magnitudes were converted to the PS1 system (Section 3.4.1) before being “stitched” to the PS1 light curves. The resulting PS1+SDSS light curves are shown in Figure 3.9.

Candidate PSO J334.2028+1.4075 also has a Galaxy Evolution Explorer (*GALEX*) Time Domain Survey ([Gezari et al., 2013](#)) light curve available in the NUV band ($\lambda_{\text{eff}} = 2316\text{\AA}$) ≈ 1 year before the start of PS1 MDS. We superimpose on the NUV light curve a sinusoid of the same period and phase as in the PS1 light curves and scale up the sinusoidal amplitude of the g_{P1} band ($\lambda_{\text{eff}} = 4810\text{\AA}$) by the observed exponential relation of variability amplitude as a function of (rest-frame) wavelength

for quasars from [Vanden Berk et al. \(2004\)](#) (see Section 3.3.3). The model is visually consistent with the larger variability amplitude of the NUV light curve (Figure 3.9). (The ordinate offset of the sinusoid is chosen such that it matches the mean magnitude of the NUV light curve.)

In explaining the observed periodic variability of the CRTS candidate PG 1302–102, [D’Orazio et al. \(2015\)](#) derived the expected variability amplitude ratio between the *GALEX* FUV and NUV and the CRTS *V*-band from spectral slopes, a corollary of their Doppler boosting model. However, we have shown, in addition to numerous previous studies (*e.g.* [Gezari et al. 2013](#); [Heinis et al. 2016b](#); [MacLeod et al. 2010](#); [Vanden Berk et al. 2004](#)) that a larger variability amplitude at shorter wavelengths is commonly observed in quasars and AGNs, and Doppler boosting is not unique in explaining the phenomenon.

3.4.3 Testing the Persistence of Periodicity with Extended Baseline Photometry

We recalculated the S/N parameter ξ for the extended light curves by forcing the same \bar{P} detected in PS1 only light curves (Table 3.7). Though all candidates still have high significance values ($\xi(g) \sim 3$) and the extended data have variation amplitudes similar to their model sinusoidal amplitudes (Table 3.4), the extended light curves do not agree with the extrapolation of their respective “PS1 only” sinusoidal models and the periodic oscillations are not persistent.

The three candidates were selected by first calculating their significance with

respect to the null hypothesis of white noise (*i.e.* constant power over frequencies) (Section 3.3.4). Previous systematic searches also assumed the null hypothesis of damped random walk noise (DRW; Kelly et al. 2009) to calculate the false-alarm rate and thus statistical significance of their selected binary candidates (Graham et al. 2015b; L15; Charisi et al. 2016). (However, we note that the extended data in Charisi et al. (2016) show that their DRW simulations underestimate the false-alarm rate) The DRW null hypothesis is motivated by results from quasar light curve analyses which demonstrate that the DRW model is a good description of normal quasar variability (Kelly et al., 2009; MacLeod et al., 2010). The power spectrum of the DRW process is $P(f) = 2\sigma^2\tau^2/[1 + (2\pi\tau f)^2]$ – where σ^2 is the short-timescale variance and τ corresponds to the characteristic timescale — it has a power law slope of -2 at high frequencies ($f > (2\pi\tau)^{-1}$) and flattens to 0 at low frequencies, analogous to the X-ray power spectrum of AGNs and X-ray binaries in the “low hard” state (*e.g.* review by McHardy 2010, pp 203-32).

However, regardless of the model chosen for the power spectrum of quasar variability to evaluate the significance of the period detection, we are fundamentally limited by the several-year temporal baseline of current time domain surveys. Vaughan et al. (2016) show that mock light curves generated from both DRW and a broken power law power spectrum cannot be distinguished from a periodic signal over ~ 2 cycles, especially when adding photometric noise and down-sampling the light curve to the actual observing cadence. Fortunately, a periodic candidate can be favored or disfavored by observing it for a longer period of time (for a total of >5 cycles, ideally with better sampling and photometric precision), as Vaughan et al.

(2016) have suggested and as we have demonstrated in this paper.

3.5 Black Hole Mass Estimates and Inferred Binary Parameters

In order to measure the total black hole mass of the system (M_{BH}) and derive parameters under the binary model, we extracted the archival SDSS spectrum of candidate PSO J333.9833+1.0242. We were also able to acquire spectroscopic observations of the other two candidates from DCT or the Gemini-South Telescope: the spectrum of PSO J333.0298+0.9687 was obtained in 2015 Quarter 3 with DCT’s DeVeney spectrograph with 300 g/mm grating and 1” slit for an exposure time of 1400 s. The data were reduced with the standard IRAF routines. A Gemini GMOS-S long-slit spectrum was obtained for PSO J334.2028+1.4075 in the 2015A Semester (Program ID: GS-2015A-Q-17. PI: T. Liu) with R400 grating and 0”.75 slit for a total exposure time of 720 s. The Gemini spectrum was reduced with the Gemini IRAF package.

In both spectra acquired, we clearly captured the broad Mg II line, allowing us to use a combination of the broad line velocity and luminosity of the nearby continuum to estimate black hole mass of the system from McLure & Dunlop (2004):

$$\log \left(\frac{M_{\text{BH}}}{M_{\odot}} \right) = 3.2 \left(\frac{\lambda L_{\lambda}}{10^{44} \text{ ergs s}^{-1}} \right)^{0.62} \left(\frac{\text{FWHM}(\text{MgII})}{\text{km s}^{-1}} \right)^2. \quad (3.13)$$

In order to measure the Mg II broad line width for the black hole mass estimate, we based our line fitting process on the prescription given by Vestergaard & Wilkes (2001), in order to subtract the iron pseudo-continuum emission that contam-

inates in the vicinity of the Mg II 2800Å line: we first broadened the iron template presented in [Vestergaard & Wilkes \(2001\)](#) by convolving with a series of Gaussian kernels in an incremental step of 250 km/s, such that $1000 \text{ km/s} < \text{FWHM}_{\text{QSO}} < 12000 \text{ km/s}$. Then, in a fitting window of [2250,2650]Å where iron emission is conspicuous ([Forster et al., 2001](#)), we compare the FWHM=2000 km/s template with the spectrum (from which a power law continuum was already subtracted) and iteratively determined a scale factor. We then compared the series of scaled and broadened templates with the spectrum to determine the best-fit FWHM_{QSO} .

After fitting for the iron emission and subtracting from the spectrum, a Gaussian was then fitted to the Mg II broad line for the fitting range [2700,2900]Å, whose FWHM is subsequently substituted into Equation 3.13. Any uncleaned sky lines were excluded from the fitting process, and the final continuum and iron-fitted spectrum was visually inspected to ensure the fitting is satisfactory (Figure 3.10). Unfortunately, part of the Gemini spectrum (PSO J334.2028+1.4075) was affected by a misbehaving amplifier over the wavelength range where iron pseudo-continuum emission is strong. We had to mask the affected region and were not able to obtain a good fit of the iron emission; instead we only fit a power law continuum to the spectrum.

In the spectrum, we measured the continuum flux density at $\lambda = 3000\text{Å}$ ($f_\lambda(3000 \text{ Å})$) from the continuum fitting and corrected for Galactic extinction using the dust map from [Schlafly & Finkbeiner \(2011\)](#) and the extinction curve from [Cardelli et al. \(1989\)](#). With the redshift measured from the spectrum, we were then able to translate flux into luminosity $\lambda L_\lambda = \lambda 4\pi D_L^2 f_\lambda (1+z)$ and calculate the total

black hole mass.

Though candidate PSO J333.9833+1.0242 has a measured black hole mass from Shen et al. (2008), we applied the same line fitting and mass measurement routine to its SDSS spectrum to obtain a self-consistent measurement. We estimate $\log(M_{\text{BH}}/M_{\odot}) = 9.5 \pm 0.4$, consistent with the black hole mass of $\log(M_{\text{BH}}/M_{\odot}) \approx 9.8$ from Shen et al. (2008).

For PSO J334.2028+1.4075, we measured black hole mass $\log(M_{\text{BH}}/M_{\odot}) = 9.1$ (with an error of 0.4 dex associated with the black hole mass estimator Mg II; McLure & Jarvis 2002); it is lower than $\log(M_{\text{BH}}/M_{\odot}) = 9.97 \pm 0.5$ quoted in L15 — which was estimated from C IV (Vestergaard & Peterson, 2006) and was not measured from an electronic spectrum — but consistent with the previous black hole mass, considering the large scatter between the Mg II and C IV-based methods ($\log(M_{\text{MgII}}/M_{\text{CIV}}) = -0.06$ dex, with a dispersion of 0.34 dex; Shen et al. 2008).

Having obtained the black hole masses, we convert the observed variability period to the rest frame of the presumed binary: $t_{\text{var}} = t_{\text{orb}}(1 + z)$ and directly calculate binary orbital separation from Kepler’s third law for a circular binary orbit:

$$\frac{t_{\text{orb}}^2}{a^3} = \frac{4\pi^2}{GM} \quad , \quad (3.14)$$

where t_{orb} is the rest-frame binary orbital period, a is the orbital separation, and M is the total mass of the system. The candidates’ continuum flux density, Mg II line width, black hole mass, redshift, rest frame variability period t_{rest} , and inferred

binary orbital separation a are tabulated in Table 3.8.

Even though the three periodic quasar candidates from our search in PS1 MD09 have been disfavored by our extended baseline analysis, we compare their observed period and inferred binary separation with search results from two other time domain surveys in Figure 3.11: CRTS (Graham et al., 2015b) and PTF (Charisi et al., 2016). Assuming the typical CRTS baseline of 9 years, all but seven of the 111 candidates claimed by Graham et al. (2015b) have variations of less than 3 cycles (they require a minimum number of 1.5 cycles in their search), an insufficient data length for a robust periodicity detection according to Vaughan et al. (2016) (see our discussion in Section 3.4.3). As for the 50 candidates from PTF (Charisi et al., 2016), although the majority (82%) of the candidates have more than 3 cycles of variation, a large fraction of them have observed periods clustered around one year (42% of their candidates have periods between 300 – 400 days), a potential sign of the aliasing effect of periodograms due to seasonal sampling (MacLeod et al., 2010), even though their DRW simulations were down-sampled to the observing cadence to account for this effect.

3.6 Summary and Conclusions

Periodic variability in quasars on the timescales of months to years has been theoretically predicted as a signature of an SMBHB. Recent simulations show that in triaxial galaxies (*e.g.* Vasiliev et al. 2015), the “final parsec problem” (*e.g.* review by Milosavljević & Merritt 2003) is no longer an insurmountable problem that stalls

binary evolution at $a > 1$ pc separations and that binaries can evolve into the GW-dominated regime ($a < 10^{-3}$ pc) within a few Gyrs. A systematic search for periodic quasars in a large synoptic survey thus provides a novel method to search for SMBHBs in the final phase of their evolution and can potentially yield GW sources in the nano-Hz frequency regime which is accessible to pulsar timing arrays (PTAs) including NANOGrav (McLaughlin, 2013) and the Parkes Pulsar Timing Array (Hobbs, 2013).

Our systematic search in the Pan-STARRS1 (PS1) MD09 field resulted in three periodic quasar candidates, from an initial sample of ~ 700 color-selected quasars, that are apparently periodic over the PS1 baseline of 4 years. We further tested the persistence of their periodicity with archival light curves from SDSS Stripe 82 and followed up with imaging with the DCT. Archival *GALEX* photometry also confirms a larger amplitude of variation at shorter wavelengths, consistent with previous quasar variability studies. These extended-baseline data with photometric precision comparable to that of PS1 disfavor a simple sinusoidal model for the three candidates over an extended baseline of $\sim 5 - 12$ cycles. This corresponds to a detection rate of < 1 out of 670 quasars ($< 1.5 \times 10^{-3}$), which is still compatible with the theoretically predicted sub-parsec binary quasar fraction of $< 10^{-3}$ out to $z = 1$ from cosmological SMBH merger simulations (Volonteri et al., 2009). The detection rate per area (< 1 in 5 deg^2) is also in agreement with the theoretical prediction of 100 quasars per 1000 deg^2 of search area (or 0.5 periodic quasars in 5 deg^2) from Haiman et al. (2009) for a flux-limited survey of quasars with $m_i < 22.5$ mag. Our ongoing search over all 10 PS1 MDS fields, together with using nightly stacked

images in the future which are ~ 1 mag deeper, should increase our sensitivity to true SMBHBs by a factor of 100, and yield tens of promising SMBHB candidates for extended baseline monitoring and multiwavelength studies.

In comparison to other SMBHB searches, we note that there are two binary candidates with double broad-line features from a sample of $\sim 17,500$ SDSS quasars (or a detection rate of $\approx 10^{-4}$) for $z < 0.7$ (Boroson & Lauer, 2009), consistent with the predicted SMBHB rate of $\sim 10^{-4}$ ($z < 0.7$) from Volonteri et al. (2009). We also note that Graham et al. (2015b) imply a similar detection rate to our study of $68/\sim 75,000 \sim 0.9 \times 10^{-3}$ (for quasars $z < 1$), and Charisi et al. (2016) find a detection rate of $\approx 1.4 \times 10^{-3}$ for $z < 3$ (or 0.9×10^{-3} for the sub-sample that remained significant after their re-analysis with extended data); however, see our discussions in Section 3.4.3 and the relevant parts in Section 3.5 on the robustness of those claimed candidates.

We have demonstrated the power of an extended baseline in testing periodic quasar candidates in surveys whose temporal baselines (covering only $1.5 - 4$ cycles) are susceptible to false detections from red noise characteristic of normal quasar variability. Fortunately, for most of the periodic quasar candidates discovered in recent optical time domain surveys, continued monitoring over the next few years can robustly test the persistence of the periodicity over a necessary number of cycles (> 5) to filter out false alarms, and verify strong SMBHB candidates for direct detection in GWs by PTAs.

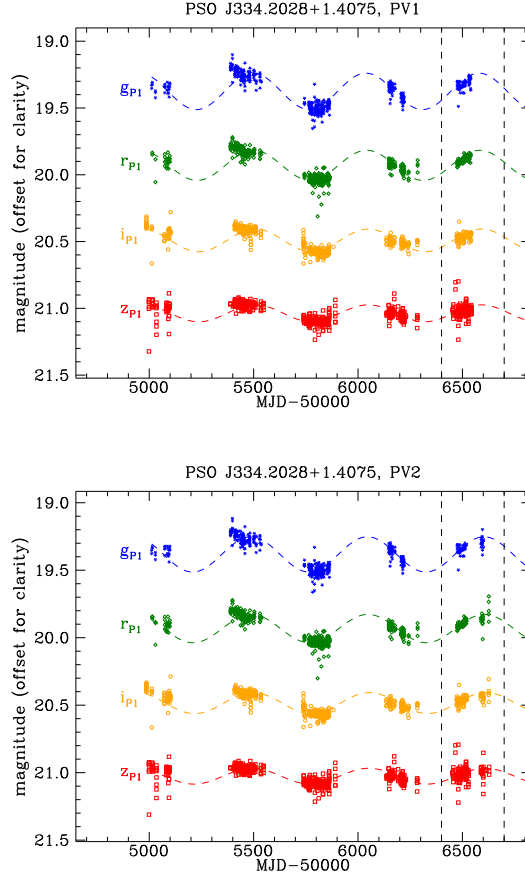


Figure 3.1: In L15, we analyzed the periodic quasar candidate PSO J334.2028+1.4075 based on its light curves in PV1 (upper panel), while its analysis in this paper is based on its light curves from PV2 (lower panel). We note the extra data from the last phase of PS1 MDS are included in PV2 (dashed box), while our conclusions from our new analysis on its significance as a periodic quasar candidate did not change. 4.5σ outliers in g and z filters in both versions have been clipped. The dashed lines are a sinusoid of $P = 558$ days (see text for details).

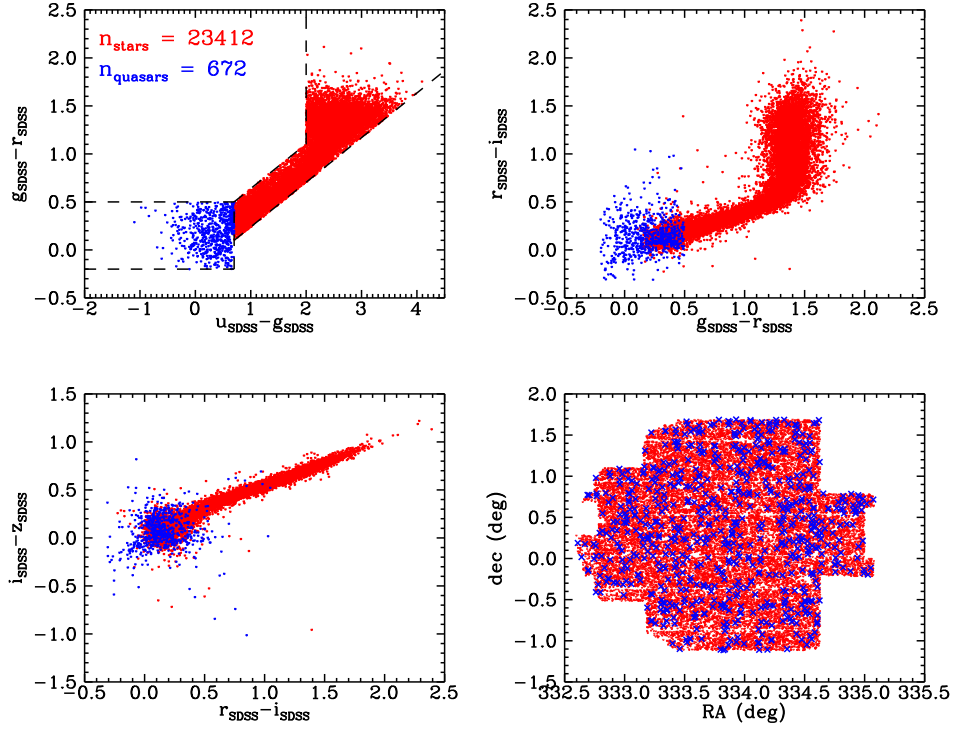


Figure 3.2: First three panels: cross-matched stars and quasars are selected by their SDSS colors (converted from u_{CFHT} g_{P1} r_{P1} i_{P1} z_{P1}). In the upper left panel, the regions occupied by quasars (blue) and stars (red) are represented by dashed boxes, and the stellar region does not include RR Lyrae variables. Bottom right panel: spatial map of all stars and quasars (red dots and blue crosses, respectively) in MD09 that have cross-matches in the PS1 \times CFHT catalog. The deep stack photometry (Heinis et al., 2016b) was performed with each PS1 “sky cell” as the smallest unit (each MD field is divided into 10×10 such rectangular regions), hence the rectangular shape. The actual search area is smaller than the total area of MD09 field and is about 5 deg^2 .

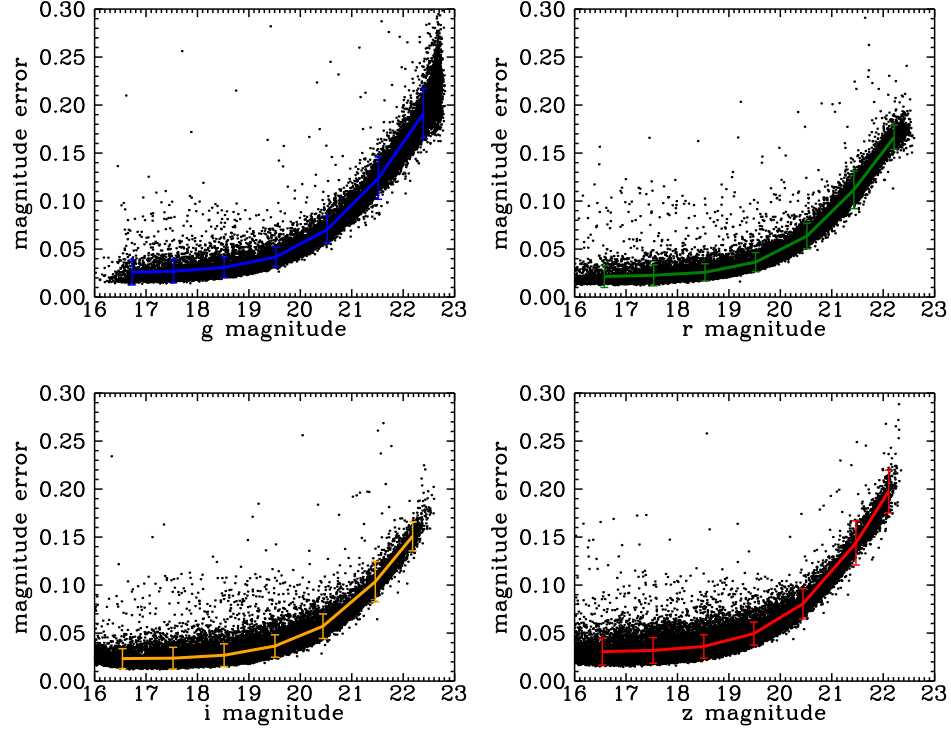


Figure 3.3: For our sample of stars, we plot the observed scatter (standard deviation of the light curve) as a function of magnitude and fit the binned relation to a parabola (Equations 3.1–3.4). We have masked outliers at the 4.5σ level in our scatter plot, and they are excluded from the binned scatter vs. magnitude relation. The relations are similar in the four filters (~ 0.03 mag at the bright end and rising to ~ 0.15 mag at the faint end), and the size of the error bars is less than 20 mmag, reflecting the stability of the PS1 system over the course of the survey and zero-point variations mainly due to the atmosphere (Schlafly et al., 2012).

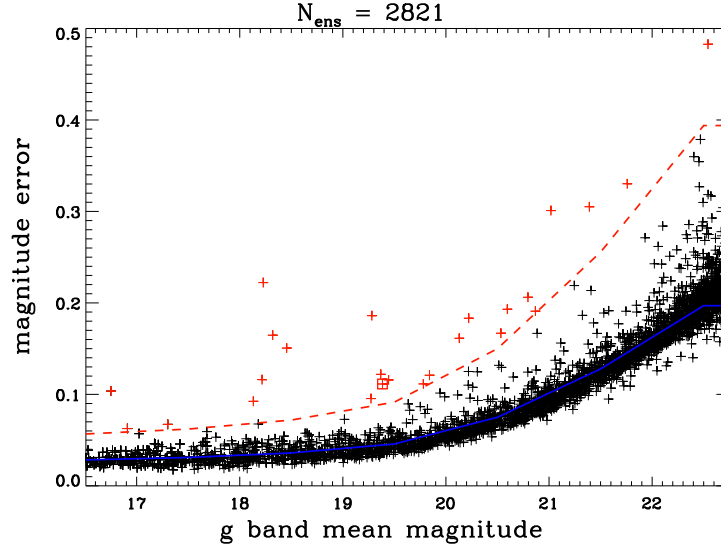


Figure 3.4: Magnitude error (light curve standard deviation) vs. magnitude in the g_{P1} filter for all the objects in one “ensemble” (crosses). The majority of the 2821 sources in the ensemble are non-variable, and their error vs magnitude relation (black crosses) can be represented as a piece-wise linear function (blue solid line), and any objects varying above the 2σ level (red dashed line) are excluded (red crosses). After three iterations, the target quasar of this ensemble (marked with an additional red square) is selected as a variable from this ensemble.

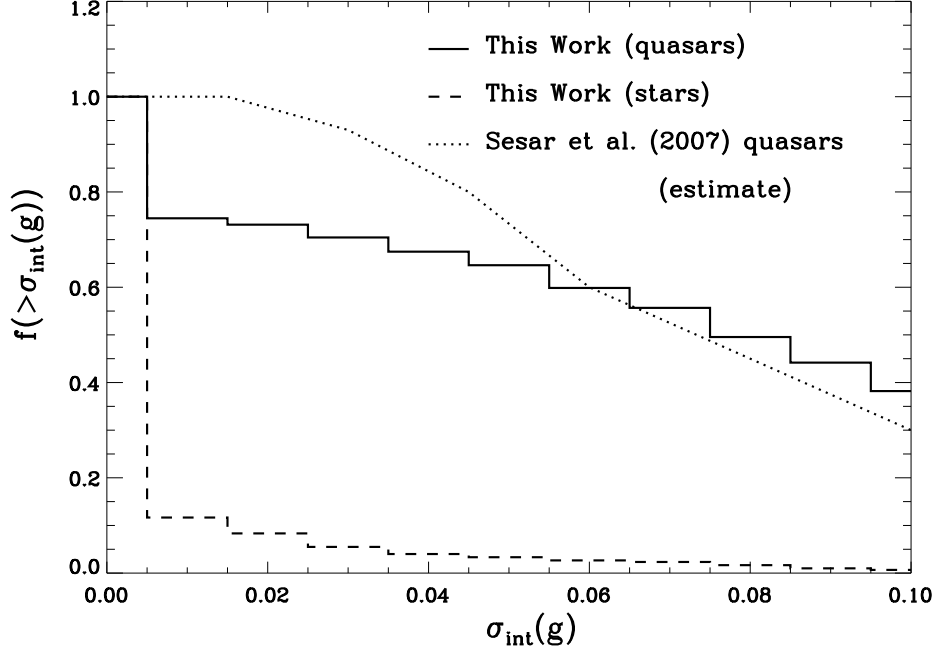


Figure 3.5: The number fraction of our MD09 quasars that vary more than σ_{int} (bin size = 0.01 mag) in the g_{P1} band (solid histogram) decreases with increasing intrinsic variability, and is in agreement with results from SDSS Stripe 82 quasars (Sesar et al., 2007) for $\sigma_{\text{int}} > 0.06$ mag. The variability fraction of a control sample of stars is shown in the dashed histogram. Plotted with a dotted line are number fractions estimated from Sesar et al. (2007) which were derived from their sample of spectroscopically confirmed quasars.

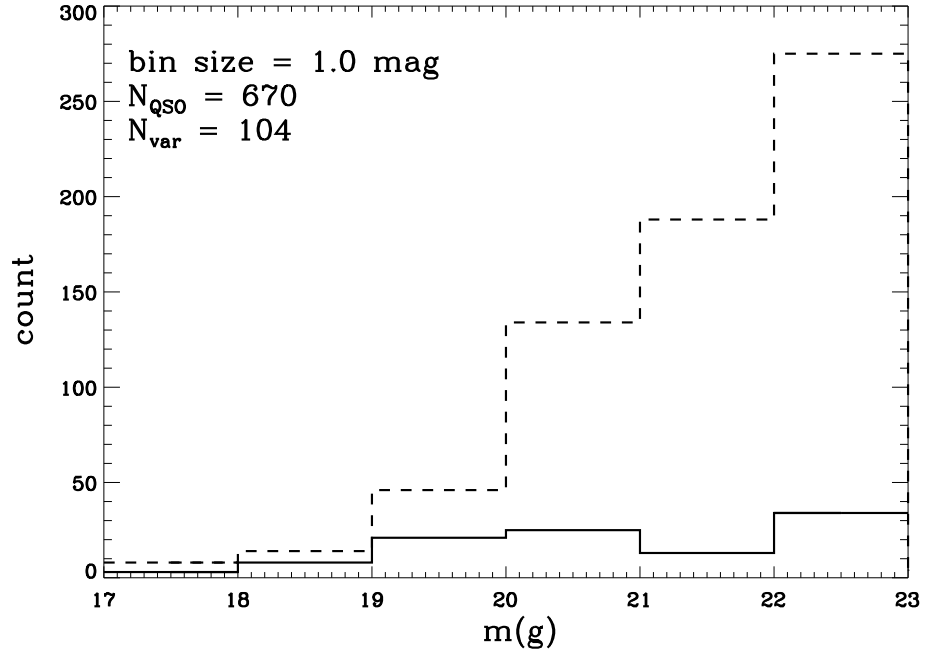


Figure 3.6: The g_{P1} band apparent magnitude distribution of our MD09 quasar sample. The full PS1 \times CFHT quasar sample (dashed histogram; $N_{\text{QSO}} = 670$) is similar to the distribution derived from quasar luminosity function (Section 3.3.3), and our variability selection (solid histogram; $N_{\text{var}} = 104$).

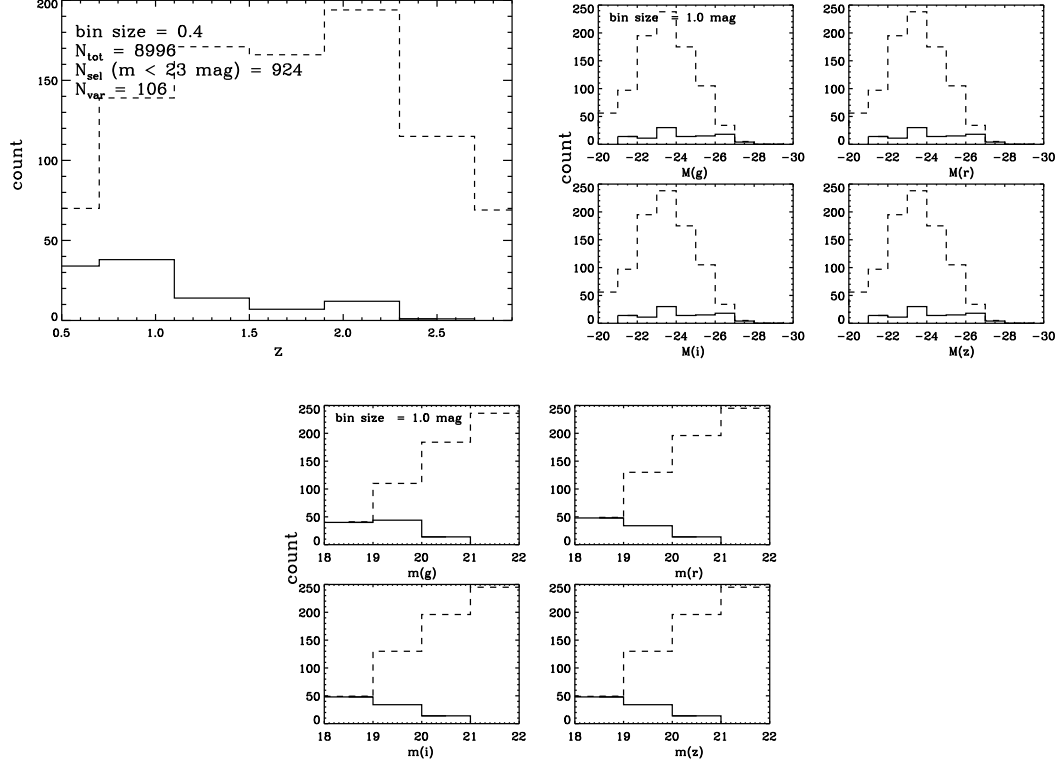


Figure 3.7: To simulate the detectability of quasars by our selection criteria whose variability amplitude obeys the empirical relations of normal AGN variability found in [Heinis et al. \(2016b\)](#), we draw ~ 9000 quasars from the redshift and absolute magnitude distributions derived from the quasar luminosity function in [Ross et al. \(2013\)](#) (full distribution not included). Among the “visible” quasars ($m < 23$ mag; dashed histogram), our variability selection is biased toward lower luminosity (and thus in general more variable) quasars at lower redshifts (solid histogram).

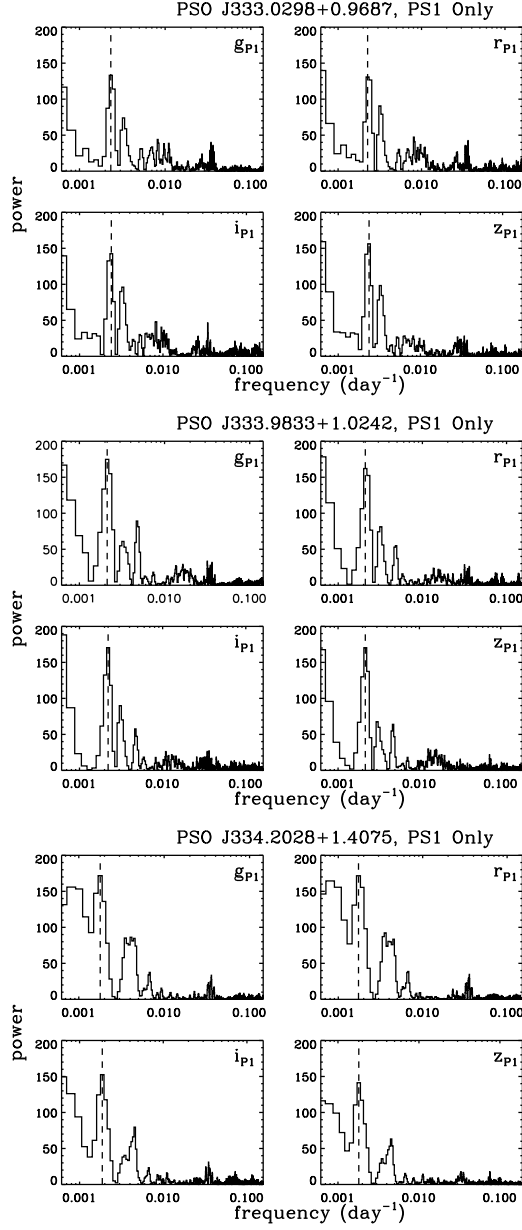


Figure 3.8: As part of our periodic quasar selection, we ran the Lomb-Scargle periodogram on PS1 light curves and selected the sources that have a coherent period detected in all four filters with high significant factors. In each set of panels, the coherent peak was marked with a dashed line in each filter.

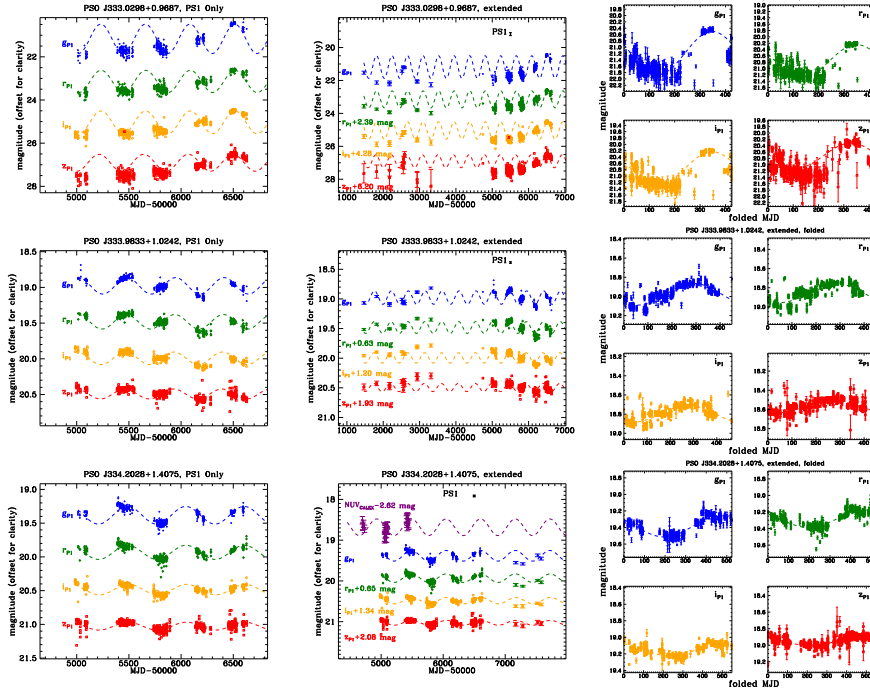


Figure 3.9: Left panels: PS1-only light curves in the g_{P1} r_{P1} i_{P1} z_{P1} filters. Light curves are offset for clarity. The light curves in different filters are fitted to sinusoidal functions of the same period (\bar{P}) and phase and of their respective best-fit amplitudes (dashed lines). The PS1 photometric error bars are omitted for clarity; instead, the typical photometric error is indicated in the “extended” panel. Middle panels: In the extended baseline light curves are fitted to sinusoidal functions of the same “PS1 only” period with the phase and amplitude being free parameters. S82 light curves and LMI data (taken in SDSS filters) have been converted to the PS1 photometric system. Light curves are also offset for clarity. For candidate PSO J334.2028+1.4075, its Galaxy Evolution Explorer (*GALEX*) UV light curve is also included, and we superimpose on it sinusoids of the scaled-up amplitude (purple) (see text for details). Right panels: the extended baseline light curves are folded on the same period as the first two panels and fitted to sinusoidal functions.

Table 3.5: Extended Baseline Photometry of Periodic Quasar Candidates

| PS1 Designation | Archival | Follow-up | UT Date of Follow-up Observations |
|----------------------|----------|--------------------|--|
| PSO J333.0298+0.9687 | SDSS | – | – |
| PSO J333.9832+1.0242 | SDSS | – | – |
| PSO J334.2028+1.4075 | GALEX | DCT15Q2/Q3/16Q2/Q3 | 2015 May 28, 2015 September 17, 2015 September 19 2016 May 15, 2016 July 10 |

The column is empty if no follow-up imaging program is presented in the analysis.

Table 3.6: SDSS to PS1 Filter Offsets from Synthetic Quasar Magnitudes

| PS1 Designation | z | $g_{\text{SDSS}}-r_{\text{SDSS}}$ | $g_{\text{P1}}-g_{\text{SDSS}}$ | $r_{\text{P1}}-r_{\text{SDSS}}$ | $i_{\text{P1}}-i_{\text{SDSS}}$ | $z_{\text{P1}}-z_{\text{SDSS}}$ |
|----------------------|-------|-----------------------------------|---------------------------------|---------------------------------|---------------------------------|---------------------------------|
| PSO J333.0298+0.9687 | 1.284 | 0.2842 | -0.0197 | 0.0087 | -0.0005 | 0.0087 |
| PSO J333.9832+1.0242 | 2.234 | 0.1033 | 0.0052 | 0.0090 | -0.0108 | -0.0032 |
| PSO J334.2028+1.4075 | 2.070 | 0.1170 | -0.0127 | 0.0094 | -0.0060 | -0.0002 |

8

z is the spectroscopic redshift of the candidate. The SDSS colors $g-r$ and SDSS to PS1 magnitude offsets $m_{\text{P1}}-m_{\text{SDSS}}$ are calculated from synthetic magnitudes by convolving the composite quasar spectrum with the respective filter. The offset is then added to each LMI magnitude.

Table 3.7: Detected Period and Significance Factors of Periodogram-Selected Candidates

| PS1 Designation | $\bar{P} \pm \Delta P$ (day) | ξ (g,r,i,z) | N_{cycle} | ξ (g,r,i,z) | N_{cycle} |
|----------------------|------------------------------|--------------------------|--------------------|--------------------------|--------------------|
| PSO J333.0298+0.9687 | 428±12 | (3.54, 2.82, 2.75, 1.09) | 3.8 | (2.96, 2.48, 2.42, 0.98) | 12.1 |
| PSO J333.9833+1.0242 | 465±11 | (3.93, 2.58, 2.16, 1.34) | 3.5 | (2.84, 1.99, 1.61, 1.07) | 11.1 |
| PSO J334.2028+1.4075 | 558±19 | (3.84, 2.74, 1.80, 0.91) | 2.8 | (3.33, 2.42, 1.66, 0.90) | 4.6 |

The PS1+LMI light curve of PSO J334.2028+1.4075 totals a time span that corresponds to 4.6 cycles of sinusoidal variation ($P = 558$ days). The extended light curves span 5.2 cycles if the *GALEX* UV data are also taken into account.

Table 3.8: Spectroscopic Information and Inferred Binary Parameters of Periodic Quasar Candidates

| PS1 Designation | Spectroscopy | f_{λ} (3000 Å) [erg s ⁻¹ cm ⁻² Å ⁻¹] | FWHM(Mg II) [km s ⁻¹] | $\log (M_{\text{BH}}/M_{\odot})$ | z | t_{rest} [day] | a [pc] | a [R _s] |
|----------------------|--------------|---|--------------------------------------|----------------------------------|-------|----------------------------|-------------|--------------------------|
| PSO J333.0298+0.9687 | DCT15Q3 | 2.4×10^{-17} | 8851 | 9.2 ± 0.4 | 1.284 | 244.3 | 0.004 | 28 |
| PSO J333.9833+1.0242 | SDSS | 4.2×10^{-17} | 6157 | 9.5 ± 0.4 | 2.234 | 144.0 | 0.003 | 13 |
| PSO J334.2028+1.4075 | GS15A | 1.9×10^{-17} | 5492 | 9.1 ± 0.4 | 2.070 | 181.8 | 0.003 | 28 |

Since the three candidates are no longer significant periodic candidates with the extended baseline, the binary model is disfavored, and therefore we only show their binary parameters for comparison with other systematic searches.

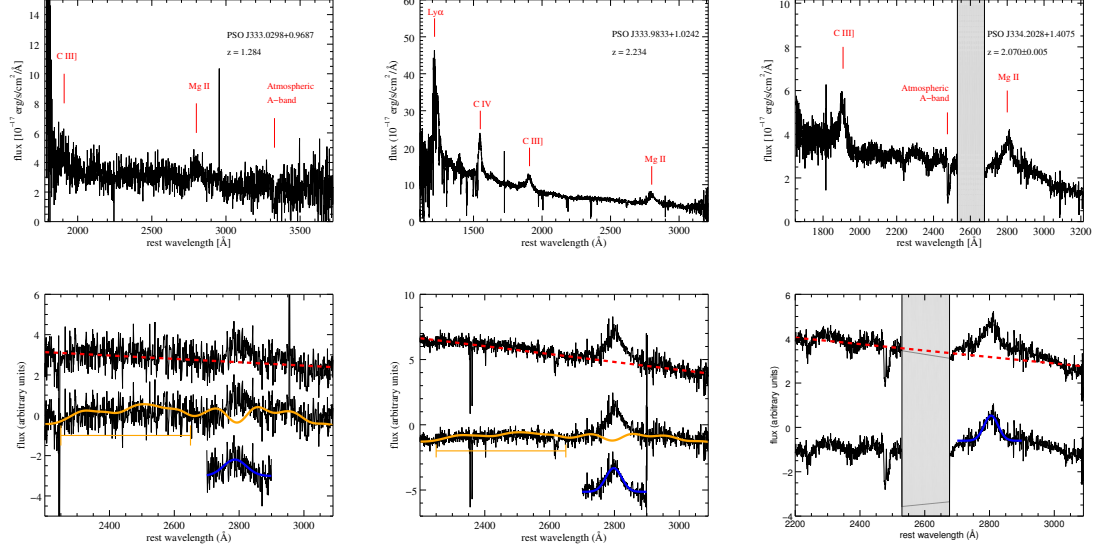


Figure 3.10: Top panels: MD09 candidate spectra from DCT/DeVeny, SDSS, and Gemini-South. Prominent emission features and the telluric absorption line at $7600 - 7630 \text{ \AA}$ (observed wavelength) are marked with red tick marks. Bottom panels: we show the procedure by which we measure the Mg II line width: we fit and subtract the power law continuum (red dashed line) and iron emission in a spectral window (orange lines) and fit the Mg II line to a Gaussian (blue line).

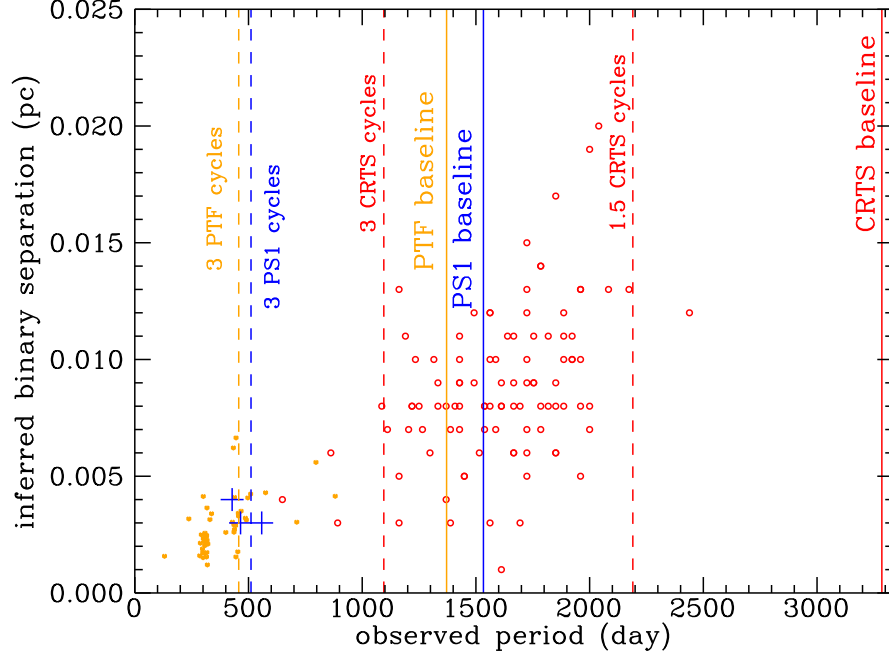


Figure 3.11: The blue plus signs mark our three periodic quasar candidates in PS1 MD09, which we classify as false alarms after failing the test of persistence over an extended baseline. The blue lines mark, from left to right, the length that corresponds to 3 cycles of variation over the MDS baseline and the 4.2-year MDS baseline. The 111 candidates from a systematic search in CRTS ([Graham et al., 2015b](#)) are in red circles. Red lines represent 3 CRTS cycles, 1.5 CRTS cycles (the minimum number of cycles required in their search), and the CRTS survey baseline (assuming the typical length of 9 years). The 50 candidates from PTF ([Charisi et al., 2016](#)) are in orange dots. Orange lines mark 3 PTF cycles and the PTF baseline (assuming the typical length of 3.8 years).

Chapter 4: Did ASAS-SN Kill the Supermassive Black Hole Binary Candidate PG 1302–102?

4.1 Introduction

Periodic light curve variability of quasars has been predicted as an observational signature of supermassive black hole binaries (SMBHBs) at sub-parsec separations, due to modulated mass accretion onto the binary (*e.g.* [D’Orazio et al. 2013](#); [Farris et al. 2014](#); [Gold et al. 2014](#)), or relativistic Doppler boosting of the emission of the secondary black hole minidisk ([D’Orazio et al., 2015](#)). This predicted signature has motivated several systematic searches for periodically varying quasars in large time domain surveys, including [Graham et al. \(2015a,b\)](#) (hereafter G15), [Liu et al. \(2015, 2016\)](#), and [Charisi et al. \(2016\)](#), and spurred a number of recent claims of (quasi-)periodicity (and binarity) that were discovered serendipitously or in previously well-known active galactic nuclei (AGN)¹ (*e.g.* [Dorn-Wallenstein et al. 2017](#); [Kovačević et al. 2018](#)). G15 reported a periodic quasar and SMBHB candidate PG 1302–102 (hereafter PG 1302), with a light curve from the Catalina Real-Time Transient Survey (CRTS) that can be fitted to a sinusoid of an observed period of

¹However, some of these claims have already been challenged: for example, [Barth & Stern \(2018\)](#) pointed out some issues that affect the [Dorn-Wallenstein et al. \(2017\)](#) analysis.

$P = 1884 \pm 88$ days over the ~ 9 year CRTS baseline. Its light curve including the Lincoln Near-Earth Asteroid Research (LINEAR; [Sesar et al. 2011](#)) data, which extends ~ 0.5 cycles before the CRTS data, is consistent with the sinusoidal fit, and archival photometry data from various telescopes are largely consistent with the extrapolation of the sinusoid ~ 10 years before LINEAR, although their sampling is sporadic.

While there have been multi-wavelength analyses of PG 1302 in the UV ([D’Orazio et al., 2015](#)), IR ([Jun et al., 2015](#)), and radio ([Kun et al., 2015](#)), which can provide key complementary clues about the true nature of a variability-selected SMBHB candidate, the periodicity of PG 1302 remains unconvincing due to the small number of cycles ($N_{\text{cycle}} \sim 2$ over a combined LINEAR+CRTS baseline). [Vaughan et al. \(2016\)](#) have cautioned against claiming periodicity over such a small number of cycles, as the stochastic variability (“red noise”) of normal quasars and AGN (*i.e.*, those that do not host SMBHBs) can easily mimic periodic variation. Indeed, [Vaughan et al. \(2016\)](#) showed that aperiodic light curves simulated using the Damped Random Walk model (DRW; [Kelly et al. 2009](#)) or a broken power-law (BPL) power spectrum can also be fitted to few-cycle data after down-sampling and adding photometric noise. Moreover, an extended baseline analysis using new monitoring data disfavors the persistence of the periodic quasar candidates from the Pan-STARRS1 Medium Deep Survey (PS1 MDS) MD09 field ([Liu et al., 2016](#)).

Three years after G15 and five since its last published CRTS data, we revisit the periodicity of PG 1302 in this Letter, by adding the publicly available light curve from the All-sky Automated Survey for Supernovae (ASAS-SN). We describe

the ASAS-SN light curve in Section 4.2 and the maximum likelihood method that we use in the analysis in Section 4.3. In Section 4.4 we describe and simulate the expectations in the case where a genuine periodicity is present, and then compare those expectations with our reanalysis of PG 1302. We conclude in Section 4.5.

4.2 Extended Light Curve from ASAS-SN

The ASAS-SN survey (Kochanek et al., 2017; Shappee et al., 2014) is regularly monitoring the variable sky down to $V \sim 17$ mag using multiple telescopes hosted by the Las Cumbres Observatory. We retrieved the ASAS-SN light curve of PG 1302 (J2000 R.A. = 196.3875, decl. = -10.5553) from 2012 February 15 to 2018 March 1 (MJD = 55,972 – 58,178) from the Sky Patrol². For calibration purposes, we choose the length of the ASAS-SN light curve (≈ 2200 days) to overlap with the CRTS light curve by ~ 400 days. Due to the dense sampling and the large photometric uncertainty of the ASAS-SN light curve, we have binned the light curve using a width of ~ 100 days (such that there are 20 bins over ~ 2000 days with an average of 46 measurements per bin) using the arithmetic mean, and the uncertainty of each bin is given by the standard deviation of the measurements.

The CRTS (Drake et al., 2009) light curve of PG 1302 was retrieved from the Second Data Release of the Catalina Sky Survey (CSS). While V_{CSS} is based largely on the Johnson V magnitude system used in ASAS-SN, there are some differences. Instead of calculating a color-dependent correction to convert between

²<https://asas-sn.osu.edu>

the V magnitudes of the two surveys, we simply apply a constant offset to the ASAS-SN light curve before it was “stitched” to the CRTS light curve: after binning the CRTS data via the same method described above (15 bins each of width of ~ 180 days), we calculate the difference between the (binned) CRTS and ASAS-SN magnitudes in each of the two overlapping seasons, *i.e.*, $\text{MJD} \approx 55,900 - 56,100$ and $\text{MJD} \approx 56,200 - 56,500$, and offset the ASAS-SN light curve by the average difference (0.17 mag) in order to match to CRTS. The LINEAR light curve of PG 1302 has also been offset and binned in the same way. Although early-time data from [Garcia et al. \(1999\)](#), [Eggers et al. \(2000\)](#) and [Pojmanski \(1997\)](#) are generally consistent with the extrapolated sinusoidal fit to LINEAR+CRTS data, we do not include them in our analysis due to their much sparser sampling and less reliable photometry.

The full baseline in our analysis is therefore given by LINEAR+CRTS+ASASSN. We present both the binned and unbinned light curves in [Figure 4.1](#). Although the ASAS-SN light curve does undulate, the periodic fluctuation detected in the CRTS light curve is not consistent with the ASAS-SN data. In particular, the extended ASAS-SN light curve fluctuation is clearly out of phase with the sinusoid fitted to the LINEAR+CRTS light curve, and the full data set favors a longer apparent period and larger amplitude.

4.3 Expectations for a True Periodic Signal

Because the LINEAR+CRTS+ASASSN light curve is inconsistent with a sinusoid of the best-fit period and phase from G15, we now analyze the combined data by considering a possible periodic signal in the presence of red noise. The basic picture is that fluctuations in the accretion disk can produce a red noise component in the power spectrum, whereas the binary is expected to produce a periodic signal.

We adopt the maximum likelihood method introduced by [Bond et al. \(1998\)](#), which has been applied in a number of previous studies, including [Miller et al. \(2010\)](#), [Zoghbi et al. \(2013\)](#), and [Foreman-Mackey et al. \(2017\)](#). The observed light curve is the combination of signal and noise $\mathbf{x} = \mathbf{s} + \mathbf{n}$, or in terms of a correlation matrix

$$C_x = C_s + C_n \quad , \quad (4.1)$$

where $C_s = \langle s_i s_j \rangle$ and $C_n = \langle n_i n_j \rangle$, and the indices i and j indicate elements of the light curve, which has a total of N elements. The noise terms are assumed to be Gaussian (which is usually true in optical astronomy); further assuming that they are uncorrelated, C_n is simply a diagonal matrix with elements $n_i n_i$. Each element of the signal matrix C_s can be expressed using the autocorrelation function

$$\langle s_i s_j \rangle = \mathcal{A}(\Delta t) = \int_{-\infty}^{+\infty} P(f) \cos(2\pi f \Delta t) df \quad , \quad (4.2)$$

where $P(f)$ is the power spectral density (PSD) of the signal, and Δt is the time lag

between s_i and s_j . Having calculated the signal matrix C_x for a set of parameters \mathbf{p} , we can then construct a likelihood function $\mathcal{L}(\mathbf{p})$ under the model $P(f)$:

$$\mathcal{L}(\mathbf{p}) = (2\pi)^{-N/2} |C_x|^{-1/2} \exp\left(-\frac{1}{2} \mathbf{x}^T C_x^{-1} \mathbf{x}\right) \quad , \quad (4.3)$$

where $|C_x|$ and C_x^{-1} are the determinant and inverse of the matrix C_x , respectively, and \mathbf{x}^T is the transpose of the time series \mathbf{x} . To calculate the likelihood under the DRW (Kelly et al., 2009), which has been successful in characterizing quasar variability (*e.g.* Kelly et al. 2009; MacLeod et al. 2010), $P(f)$ in Equation 4.2 would take the following form:

$$P(f) = \frac{2\sigma^2\tau^2}{1 + (2\pi\tau f)^2} \quad , \quad (4.4)$$

where σ^2 is the short-timescale variance, and τ is the characteristic timescale. To search for a periodic component of frequency f_0 in addition to DRW noise (hereafter “DRW+periodic”), we can introduce a delta function $\delta(f - f_0)$, so that the autocorrelation function in Equation 4.2 becomes

$$\mathcal{A}(\Delta t) = \left[\int_{-\infty}^{+\infty} P(f) \cos(2\pi f \Delta t) df \right] + A_0 \cos(2\pi f_0 \Delta t) \quad . \quad (4.5)$$

where A_0 is the amplitude of the periodic signal.

To test our implementation of the method, we simulated 10 light curves under the DRW model using the Timmer & Koenig (1995) method, uniformly sampling σ from $0.00224 \text{ mag day}^{-1/2}$, which is the minimum value from the Kelly et al. (2009)

quasar sample, to $0.0187 \text{ mag day}^{-1/2}$, which corresponds to the value at $3\sigma_{\text{Gaussian}}$ after fitting the [Kelly et al. \(2009\)](#) σ_{DRW} distribution to a Gaussian; the input τ ranges from ≈ 30 to 970 days³. We then add sinusoidal functions with amplitudes measured from the periodic candidates from PS1 MDS (T. Liu *et al.* 2018, in preparation) so that $A_0 \approx 0.1 - 0.3 \text{ mag}$. The input periods range from $P \approx 50 - 970$ days; the maximum period corresponds to two-thirds of the length of the baseline, which is the requirement in previous work including [Graham et al. \(2015b\)](#) and [Charisi et al. \(2016\)](#). We then down-sample the light curve to the observing cadence of PS1 MDS and add typical PS1 photometric noise. We then use a C implementation of an affine-invariant Markov Chain Monte Carlo (MCMC) sampler ([Goodman & Weare, 2010](#)) to sample the parameter space. Our implementation is successful in recovering the input period: the best-fit periods generally follow a one-to-one correlation with the input values. To select those by which the DRW+periodic model is at least moderately preferred, we further impose the cut $\text{AIC}_{\text{DRW+periodic}} - \text{AIC}_{\text{DRW}} < -2$, where the Akaike information criterion $\text{AIC} = 2n - 2 \ln \mathcal{L}$ when there are n parameters in the model. The AIC imposes a penalty on the more complex model, and between two models the model with the lower AIC value is therefore the preferred one. Those best-fit periods that meet this criterion correspond to > 3 cycles, and they follow a yet tighter correlation.

Next, we apply the method to a simulated DRW +periodic light curve to demonstrate the expected decrease in the p -value (and therefore increase in significance) if the periodic signal is real. We down-sampled the simulated light curve to

³All temporal parameters explored in this analysis are in the observed frame.

the sampling of the LINEAR+CRTS+ASAS-SN light curve and added photometric uncertainties that are typical of the three different surveys (Figure 4.2). The light curve is then binned using the same bin sizes as Figure 4.1. The relative amplitudes of the sinusoid and DRW noise are such that the significance level at which the DRW+periodic model is preferred is comparable between the (binned) LINEAR+CRTS-sampled light curve from the simulation and that from PG 1302. The input period of $P = 2012$ days is chosen to be the same as the best-fit period from our reanalysis of the LINEAR+CRTS+ASASSN light curve of PG 1302 (Section 4.4), and the phase of the simulated light curve also mimics that of PG 1302. As Table 4.1 shows, the method consistently recovered the input period in the LINEAR+CRTS and LINEAR+CRTS+ASASSN-sampled light curves, and the longer baseline produced a best-fit period that is closer to the true value with a smaller uncertainty. Furthermore, the p -value (for a chi-squared distribution with two degrees of freedom) has decreased significantly (by a factor of ~ 100) when the mock ASAS-SN data are included, even though they have a larger photometric uncertainty than the simulated CRTS data.

4.4 Extended Baseline Analyses of PG 1302

We now apply this method to PG 1302, and the ranges of the sampled parameters are summarized in Table 4.2; in particular, the ranges of τ and P are sampled from 200 days to 3000 days (recall that the putative period is $P = 1884$ days). As calculating the inverse and determinant of a large $N \times N$ matrix is com-

putationally intensive (Equation 4.3; both are typically $\mathcal{O}(N^3)$ operations⁴), where $N \sim 1000$ for the unbinned full-baseline light curve, we apply the method only to the binned light curve, where $N = 19$ for LINEAR+CRTS and $N = 35$ for LINEAR+CRTS+ASASSN. When we first applied the method to the CRTS-only and LINEAR+CRTS light curves (Table 4.2), the DRW+periodic model is preferred over the DRW-only model at the 98.4% and 99.9% levels, respectively. If PG 1302 were the only quasar analyzed, this would be intriguing evidence for periodicity. However, given that it was selected from an initial sample of $\sim 200,000$ CRTS quasars, its periodicity can easily be produced by chance alone; to demonstrate strong evidence for periodicity, the candidate should instead have a p -value $< 5 \times 10^{-6}$.

As we showed in Section 4.3, for a genuinely periodic source we expect that additional data should strengthen the evidence. However, the p -value of the DRW+periodic model has increased from $p = 1.39 \times 10^{-3}$ on the LINEAR+CRTS baseline to $p = 4.70 \times 10^{-3}$ after including ASAS-SN data (Table 4.2). The decrease in significance after adding new data is inconsistent with our expectation when a true periodic signal is present, which suggests that the periodic signal is not persistent.

The decrease in significance after including extended data was also seen for the sources in Charisi et al. (2016). Their initial systematic search in the Palomar Transient Factory (PTF) identified 50 periodic quasar candidates from $\sim 35,000$ spectroscopically confirmed quasars. They analyzed those candidates using additional data from CRTS and/or the intermediate Palomar Transient Factory (iPTF). Of

⁴However, we note that the algorithm `celerite` (Foreman-Mackey et al., 2017) is able to compute Equation 4.3 at a cost of $\mathcal{O}(N)$ for some classes of PSD models, which include DRWs.

the 47 candidates that have additional data, all but two had significantly increased p -values. Although the CRTS measurements have larger photometric uncertainties than PTF or iPTF and are in a different filter, the increase in the p -value may still be an indication that the additional data are inconsistent with the claimed periodicity. A similar phenomenon from the statistical perspective is also seen in a large sample of SDSS Stripe 82 quasars by [Andrae et al. \(2013\)](#): although a small number of quasars are better described by the DRW+periodic model than the DRW-only model, more quasars are preferred by DRW-only as the number of observations increases. The failure of PG 1302 and the many periodic candidates from [Charisi et al. \(2016\)](#) to demonstrate persistent periodicity therefore seems typical of the stochastic variability that is ubiquitous in normal (single black hole) quasars and AGN.

While quasar variability can be characterized by the DRW process, high-frequency power-law slopes that deviate from DRW have been found in a number of studies, including those using large samples from ground-based surveys ([Caplar et al., 2017](#); [Kozłowski, 2016](#); [Simm et al., 2016](#)) and the ones using high-quality *Kepler* AGN light curves ([Aranzana et al., 2018](#); [Edelson et al., 2014](#); [Mushotzky et al., 2011](#); [Smith et al., 2018a](#)). Because assuming the incorrect PSD form would result in an overestimate of the significance of the periodic signal, we have also analyzed PG 1302 under the more general BPL model and take the PSD in Equation 4.2 to be

$$P(f) = \frac{A f^{-\alpha_{\text{lo}}}}{1 + (f/f_{\text{br}})^{-\alpha_{\text{lo}} + \alpha_{\text{hi}}}} \quad , \quad (4.6)$$

where A is the normalization, f_{br} is the break frequency, and α_{lo} and α_{hi} are the low- and high- frequency slopes, respectively. The parameter ranges sampled are listed in Table 4.3; as also shown in the table, while the BPL+periodic model is moderately preferred over the BPL only model and the best-fit period is consistent with that in the DRW+periodic model, evidence for the periodic signal also becomes weaker when ASAS-SN data are included.

4.5 Conclusions

PG 1302 has been reported as an SMBHB candidate, having shown apparent periodic variation over ~ 2 cycles on a LINEAR+CRTS baseline of ~ 10 years (G15). Its variability has been modeled as the relativistic Doppler boosting of the secondary minidisk (D’Orazio et al., 2015), and it has an inferred binary separation of ~ 0.01 pc. If verified, PG 1302 would be one of the most compact SMBHB candidates discovered to date, and searches using similar techniques can potentially uncover more candidates in the gravitational wave-emitting regime for multi-messenger studies with the pulsar timing arrays.

In this Letter, we have included the recent ASAS-SN data for this source, which has regular and dense sampling spanning ~ 5 years since CRTS and thus extends the total baseline to ~ 15 years. We have also applied a maximum likelihood analysis to search for a periodic component in addition to red noise, which is modeled as the

DRW process or a BPL PSD. While we find that DRW+periodic or BPL+ periodic is the preferred model for the LINEAR+CRTS light curve, evidence for either model becomes weaker after adding ASAS-SN data. As Doppler boost from a binary should produce persistent periodicity, and more data should only strengthen the signal, our reanalysis suggests that the variability of PG 1302 may be inconsistent with this proposed model.

In this Letter, we have highlighted the importance of the long-term monitoring of SMBHB candidates that have been selected for their periodicity; it is also necessary to evaluate the significance of the periodic signal in the presence of stochastic variability. Any robust periodic quasar and SMBHB candidate should be able to withstand those two tests.

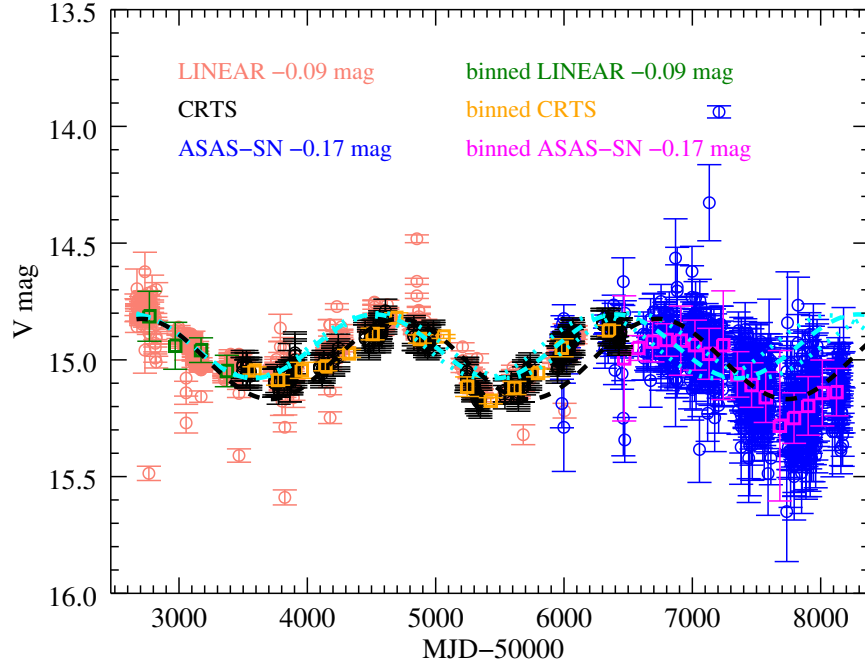


Figure 4.1: Combined light curve of PG 1302–102 from LINEAR (pink), CRTS (black) and ASAS-SN (blue). LINEAR and ASAS-SN have been offset to match CRTS (see the text). Adopting the best-fit period and its uncertainties from G15, sinusoids with periods of $P = 1884$ days (cyan dashed line) and $P = 1884 \pm 88$ days (cyan dotted lines) have been fitted to the LINEAR+CRTS light curve and extrapolated to guide the eye. Additionally, we have superimposed a best-fit sinusoid of the period $P = 2012$ days (black dashed line), the best-fit period of the LINEAR+CRTS+ASASSN light curve that we determined under the DRW+periodic model. The binned light curve is also shown (LINEAR: green; CRTS: orange; ASAS-SN: magenta). Individual images of the light curve have not been checked for spurious photometric detections.

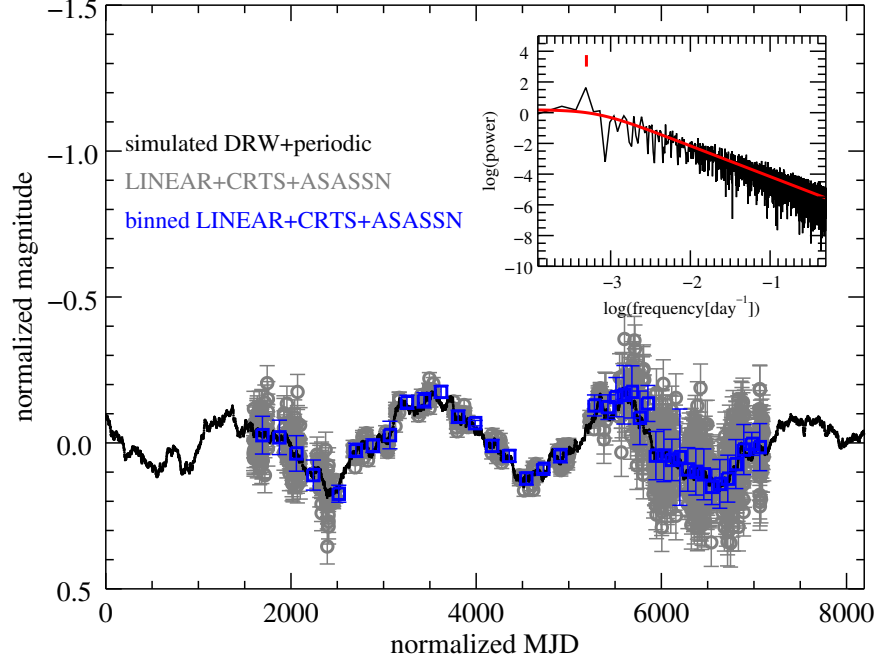


Figure 4.2: We generate a light curve under the DRW model and inject a periodic function. The light curve is initially nightly sampled (black line). We then down-sampled the perfect light curve and added typical photometric noise of the LINEAR, CRTS, and ASAS-SN data (gray circles with error bars). The resampled light curve is then binned (blue squares with error bars). The inset shows the periodogram of the evenly sampled light curve without photometric noise. The DRW model that generates the light curve is superimposed (red line), and the input period is indicated with a red tick mark. We find that despite the significant photometric uncertainties in the simulated ASAS-SN data, its addition to the analysis strongly improves the evidence for periodicity when a periodic signal is actually present.

Table 4.1: Maximum Likelihoods for the Simulated DRW+periodic Light Curve

| | DRW (LINEAR+CRTS) | DRW+periodic (LINEAR+CRTS) | DRW (LINEAR+CRTS+ASASSN) | DRW+periodic (LINEAR+CRTS+ASASSN) |
|----------------------------|----------------------|-------------------------------|-----------------------------|--------------------------------------|
| $\ln \mathcal{L}_{\max}$ | 22.98 | 30.04 | 46.42 | 58.17 |
| p -value | ... | 8.59×10^{-4} | ... | 7.87×10^{-6} |
| P_{bestfit} (day) | ... | $2060.75^{+229.75}_{-430.24}$ | ... | $2026.83^{+59.42}_{-70.57}$ |

Table 4.2: Damped Random Walk Parameter Ranges Sampled by MCMC

| | DRW (LINEAR+CRTS) | DRW+periodic (LINEAR+CRTS) | DRW (LINEAR+CRTS+ASASSN) | DRW+periodic (LINEAR+CRTS+ASASSN) |
|--|----------------------|-------------------------------|-----------------------------|--------------------------------------|
| σ_{\min} (mag day ^{-1/2}) | 0.00224 | 0.00224 | 0.00224 | 0.00224 |
| σ_{\max} (mag day ^{-1/2}) | 0.0187 | 0.0187 | 0.0187 | 0.0187 |
| τ_{\min} (day) | 200 | 200 | 200 | 200 |
| τ_{\max} (day) | 3000 | 3000 | 3000 | 3000 |
| $\ln A_{0\min}$ | ... | -10 | ... | -10 |
| $\ln A_{0\max}$ | ... | 5 | ... | 5 |
| P_{\min} (day) | ... | 200 | ... | 200 |
| P_{\max} (day) | ... | 3000 | ... | 3000 |
| $\ln \mathcal{L}_{\max}$ | 20.49 | 27.07 | 33.19 | 38.55 |
| p -value | ... | 1.39×10^{-3} | ... | 4.70×10^{-3} |
| AIC | -36.98 | -46.15 | -62.39 | -69.10 |
| P_{bestfit} (day) | ... | $1773.60^{+434.87}_{-125.12}$ | ... | $2012.62^{+280.03}_{-219.96}$ |

Table 4.3: Broken Power-law Parameter Ranges Sampled by MCMC

| | BPL (LINEAR+CRTS) | BPL+periodic (LINEAR+CRTS) | BPL (LINEAR+CRTS+ASASSN) | BPL+periodic (LINEAR+CRTS+ASASSN) |
|---|----------------------|-------------------------------|-----------------------------|--------------------------------------|
| A_{\min} | 10^{-3} | 10^{-3} | 10^{-3} | 10^{-3} |
| A_{\max} | 10^{-2} | 10^{-2} | 10^{-2} | 10^{-2} |
| $f_{\text{br min}} \text{ (day}^{-1}\text{)}$ | 0.00033 | 0.00033 | 0.00033 | 0.00033 |
| $f_{\text{br max}} \text{ (day}^{-1}\text{)}$ | 0.005 | 0.005 | 0.005 | 0.005 |
| $\alpha_{\text{lo min}}$ | 0 | 0 | 0 | 0 |
| $\alpha_{\text{lo max}}$ | 2 | 2 | 2 | 2 |
| $\alpha_{\text{hi min}}$ | 2 | 2 | 2 | 2 |
| $\alpha_{\text{hi max}}$ | 4 | 4 | 4 | 4 |
| $\ln A_{0 \min}$ | ... | -10 | ... | -10 |
| $\ln A_{0 \max}$ | ... | 5 | ... | 5 |
| $P_{\min} \text{ (day)}$ | ... | 200 | ... | 200 |
| $P_{\max} \text{ (day)}$ | ... | 3000 | ... | 3000 |
| $\ln \mathcal{L}_{\max}$ | 19.89 | 26.82 | 32.90 | 38.37 |
| $p\text{-value}$ | ... | 9.78×10^{-4} | ... | 4.21×10^{-3} |
| AIC | -31.79 | -41.65 | -57.80 | -64.75 |
| $P_{\text{bestfit}} \text{ (day)}$ | ... | $1713.78^{+133.90}_{-116.09}$ | ... | $1988.13^{+114.11}_{-845.88}$ |

Chapter 5: Supermassive Black Hole Binary Candidates from the Pan-STARRS1 Medium Deep Survey

5.1 Introduction

Supermassive black hole binaries (SMBHBs) are expected as a result of galaxy mergers occurring the Universe (*e.g.* [Begelman et al. 1980](#)). As the supermassive black holes (SMBHs) in the centers of massive galaxies sink to the center of the merged system via dynamical friction, the pair of active SMBHs on \sim a few-kpc scale can be observable as a dual active galactic nucleus (AGN; *e.g.* [Comerford et al. 2015](#)). As its separation continues to shrink by ejecting stars in the “loss cone”, the pair becomes a gravitationally-bound SMBHB at a sub-parsec separation. While spatially resolving close-separation SMBHBs has been achieved with very long baseline interferometry (*e.g.* [Rodriguez et al. 2006](#)), the direct imaging of SMBHBs at farther distances is beyond the capabilities of current, or even future, telescopes. An indirect method to search for SMBHBs is via spectroscopy, where the broad emission line from one black hole is shifted due to its radial velocity ([Eracleous et al., 2012](#); [Runnoe et al., 2017](#)), or there is the presence of a double broad line feature that is due to the broad line region associated with each black hole ([Boroson](#)

& Lauer, 2009).

Another indirect technique to search for SMBHBs is via their temporal variability signatures. (Magneto-) hydrodynamical simulations of an SMBHB system (*e.g.* D’Orazio et al. 2013; Farris et al. 2014; Gold et al. 2014; MacFadyen & Milosavljević 2008; Noble et al. 2012; Shi et al. 2012) show that the binary tidal torque clears and maintains a low-gas-density cavity of a radius $\sim 2a$ (where a is the binary separation) in the circumbinary disk, and material is ushered in through a pair of accretion streams. This distinct accretion pattern of a binary-disk system causes the accretion rate to strongly modulate on the order of the orbital frequency. Therefore, assuming the accretion rate directly translates to electromagnetic luminosity, these SMBHBs would manifest as AGNs or quasars that periodically vary on a timescale of months to years. More recently, D’Orazio et al. (2015) also proposed a relativistic Doppler boosting model: the SMBHB system is viewed at a high inclination angle, and the emission dominated by the minidisk of the secondary black hole is Doppler-boosted as the secondary travels at a relativistic speed along the line of sight. In addition to optical variability, periodicity in the X-ray bands has also been predicted for SMBHBs at the inspiral stage, due to gas being flung towards and hitting the cavity wall (Tang et al., 2018).

Observationally, there have been a number of systematic searches for periodically varying quasars in large optical time domain surveys: Graham et al. (2015a,b), using the Catalina Real-time Transient Survey (CRTS); Charisi et al. (2016), using the Palomar Transient Factory (PTF); and Liu et al. (2015, 2016) (hereafter L15 and L16, respectively), using the Pan-STARRS1 Medium Deep Survey (PS1 MDS). Gra-

ham et al. (2015b) claimed 111 SMBHB candidates from a search among $\sim 200,000$ spectroscopically confirmed quasars in the CRTS footprint, and Charisi et al. (2016) found 50 SMBHB candidates from a sample of $\sim 35,000$ spectroscopic quasars in PTF, 33 of which remained significant after their re-analysis with extended data.

However, due to the stochastic nature of normal (*i.e.* single black hole) quasar variability, the search for a periodic signal is highly susceptible to red noise (*i.e.* increasing variability power on longer timescales) masquerading as periodicity over a small number of cycles (Vaughan et al., 2016) and thus could produce a large number of false positive detections in a systematic search. In fact, from the candidates reported by Graham et al. (2015b) and Charisi et al. (2016) (assuming they are all genuine SMBHBs with their claimed binary parameters), Sesana et al. (2017) concluded that the expected stochastic gravitational wave background would exceed the current pulsar timing array (PTA) upper limit by a factor of a few to an order of magnitude. We addressed this issue of false positives due to red noise contamination in L16, where we tested the persistence of the periodic candidates with archival SDSS Stripe 82 light curves or new monitoring data taken at the Discovery Channel Telescope (DCT) since 2015, extending the total length of the baseline to $N_{\text{cycle}} > 5$. We find 3 periodic candidates from $\sim 1,000$ color-selected quasars in one PS1 Medium Deep field MD09, though none of them appear to be persistent over an extended baseline. Further, we have reanalyzed the best candidate from the CRTS SMBHB sample, PG 1302–102 (Graham et al., 2015a), by including new photometric data from the All-sky Automated Survey for Supernovae (ASAS-SN; Kochanek et al. 2017; Shappee et al. 2014), and we have shown that the detected periodicity

does not persist as expected for a true SMBHB (Liu et al., 2018).

Here, we expand our analysis in L16 to all ten fields in the Pan-STARRS1 Medium Deep Survey (Section 5.2), where we have searched for periodic quasars (Section 5.3) and identified 26 candidates (Section 5.4). In addition to monitoring the candidates on a longer baseline with DCT and the Las Cumbres Observatory network telescopes (Section 5.5), we also adopt a maximum likelihood method to reanalyze the significance of their periodicity and take into account normal quasar variability (Section 5.6). We also discuss the cumulative SMBHB rate from our search and compare with previous work and theoretical predictions (Section 5.7.1). A sample of SMBHB candidates from a systematic search are also exciting in the era of multi-messenger astronomy, as they are possible gravitational wave sources for the PTAs (Section 5.7.2). We also look ahead to the era of the Large Synoptic Survey Telescope (LSST), which will transform the study of the variable sky over its 10 years of operation and can potentially discover tens of thousands of SMBHBs (Section 5.7.3). Finally, we explore the multi-wavelength properties of the best SMBHB candidate from our sample, properties which have been explored both theoretically and observationally and are complementary to searching for SMBHBs in the time domain (Section 5.7.4). We summarize our results in Section 5.8. We adopt the following cosmological parameters throughout this Paper: $\Omega_m = 0.3$, $\Omega_\lambda = 0.7$, $H_0 = 70$ km/s/Mpc.

5.2 The Pan-STARRS1 Medium Deep Survey

The Pan-STARRS1 survey (PS1; [Kaiser et al. 2010](#)) operated from 2009 – 2014 on the 1.8-meter PS1 telescope at the summit of Haleakala on Maui, Hawaii. $\sim 25\%$ of the survey time was dedicated to the Medium Deep Survey (MDS), a multi-filter, high-cadence time domain survey of 10 circular fields ([Table 5.1](#)), each of which is $\sim 8 \text{ deg}^2$ in size. MDS observed in the $g_{P1} r_{P1} i_{P1} z_{P1} y_{P1}$ ¹ filters on the AB photometric system ([Tonry et al., 2012b](#)) and can reach a 5σ magnitude depth of 22.5 mag in $g_{P1} r_{P1} i_{P1}$ and 22.0 mag in the z_{P1} filter in a single exposure of 113 sec ($g_{P1} r_{P1}$) or 240 sec ($i_{P1} z_{P1}$). The data were processed by the PS1 Image Processing Pipeline (IPP; [Magnier 2006](#)) and were made available to members of the PS1 Science Consortium through the PS1 Science Archive.

Each nightly observation consisted of eight single exposures; though the sub-exposures can be combined to produce “nightly stacks”, we have used the single-exposure detections in this work, as well as in our previous work presented in L15 and L16. The telescope visited the field during the 6 – 8 months that it was visible and rotated through the $g_{P1} r_{P1} i_{P1} z_{P1}$ filters every three nights (observations in $g_{P1} r_{P1}$ were carried out on the same night). Therefore, in the full MDS data set, most objects were observed ~ 400 times over the ~ 4 -year baseline ([Figure 5.1](#)).

¹Although the y_{P1} filter was not used in our work.

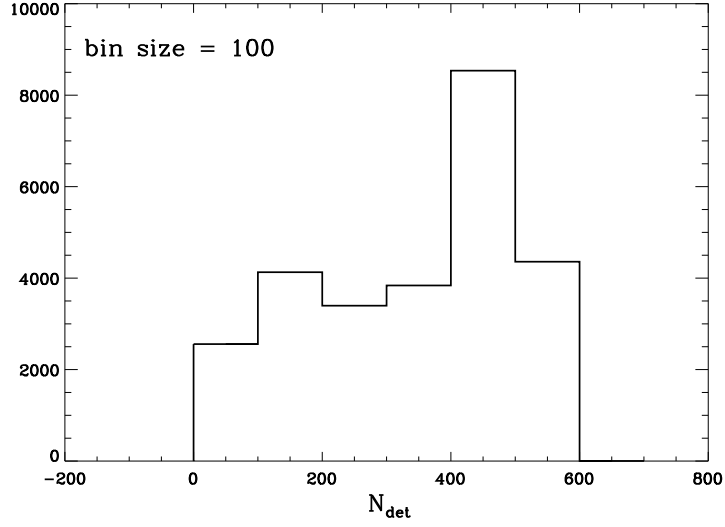


Figure 5.1: The number of detections for a random sample of $\sim 27,000$ objects in MDS.

5.3 Methods

5.3.1 Quasar and Variability Selection

We first extract sources from the catalog from the PS1 Science Archive that meet the same criteria in L16 for MD09 data: (1) they are point sources (defined as deep stack $\text{mag}_{\text{psf}} - \text{mag}_{\text{Kron}} < 0$) with good PSF quality factors ($\text{psfQF} > 0.85$); (2) they have at least five detections; and (3) the same quality flags in L16 were applied to exclude bad or poor detections. The query returns $\sim 30,000$ sources from each MD field.

We then cross-match the PS1 sources with a catalog of deep stacked images in the Canada–France–Hawaii Telescope (CFHT) u band and the PS1 $g r i z y$ bands (hereafter the PS1 \times CFHT catalog; [Heinis et al. 2016b](#)) using a one-arcsec radius.

Table 5.1: Medium Deep Field Centers

| MD Field | RA (J2000) | Dec (J2000) |
|----------|------------|-------------|
| MD01 | 02:24:50 | −04:35:00 |
| MD02 | 03:32:24 | −28:08:00 |
| MD03 | 08:42:22 | +44:19:00 |
| MD04 | 10:00:00 | +02:12:00 |
| MD05 | 10:47:40 | +58:05:00 |
| MD06 | 12:20:00 | +47:07:00 |
| MD07 | 14:14:49 | +53:05:00 |
| MD08 | 16:11:09 | +54:57:00 |
| MD09 | 22:16:45 | +00:17:00 |
| MD10 | 23:29:15 | −00:26:00 |

To extract point sources from the PS1×CFHT catalog, we used the star/galaxy classification in the catalog that has been trained on an HST/ACS sample of stars and galaxies (Heinis et al., 2016a). We then convert the u_{CFHT} g_{P1} r_{P1} band magnitudes to the SDSS system, so that the quasar selection box in SDSS colors from Sesar et al. (2007) can be directly applied (Figure 5.2). This results in $\sim 9,000$ quasars in $\sim 50 \text{ deg}^2$ of the total cross-matched sky area.

We then follow the method in L16 to select variable quasars: we construct an ensemble of objects within $\Delta\text{RA} = 0.5 \text{ deg}$ and $\Delta\text{Dec} = 0.5 \text{ deg}$ from each color-selected quasar. Then, in each filter, we compute the standard deviation σ of the

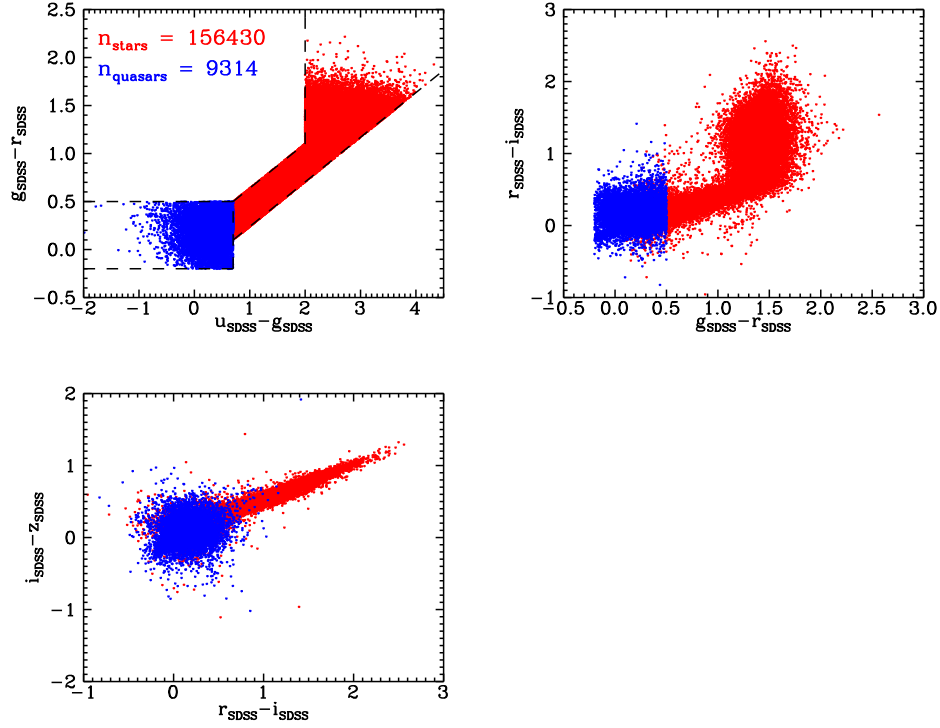


Figure 5.2: The CFHT u and PS1 $g i z$ magnitudes were first converted to the SDSS system, and quasars (blue dots) and stars (red dots) were selected by their $u_{\text{SDSS}} - g_{\text{SDSS}}$ and $g_{\text{SDSS}} - r_{\text{SDSS}}$ colors (dashed lines represent the color boxes). $\sim 9,000$ quasars were selected in the full PS1 MDS.

light curve for each object in the ensemble and iteratively exclude outliers by fitting a piece-wise linear function to the σ - m relation: $\sigma = \sigma(m)$. While most objects in the ensemble are stars and follow a tight σ - m trend, intrinsic variable objects such as quasars have significantly larger σ than stars of similar brightness and thus would appear as outliers from the trend. We identify the quasars with standard deviation $> 2\sigma(m)$ in at least two filters as variables, and $\sim 1,400$ out of the $\sim 9,000$ color-selected quasars are identified as variable quasars.

5.3.2 Searching for Periodicity

To search for periodicity among the variable quasars, we compute the Lomb-Scargle (LS) periodogram (Horne & Baliunas, 1986; Lomb, 1976; Scargle, 1982) and take advantage of the multi-filter observations and their different sampling to determine a coherent periodic signal by a “majority vote”. We also adopt the signal-to-noise (ξ) definition in Horne & Baliunas (1986), where $\xi = A_0^2/(2\sigma_r^2)$ (A_0 is the sinusoidal amplitude, and σ_r is the standard deviation of the residual) and select periodic candidates with high significance by requiring $\xi > 3$ in at least one filter. Finally, we require that the periodic variation has at least 1.5 cycles over the 4-year PS1 baseline. The search results in 26 periodic candidates from 10 MD fields, and in Tables 5.2-5.5, we break down the number from each step of the selection pipeline by the MD field. The mean g_{P1} magnitude distribution in Figure 5.3 shows our detection limit of periodic candidates at $g_{P1} \sim 20$ mag.

5.4 Results

5.4.1 Periodic Quasar Candidates from MDS

The light curves in the g_{P1} r_{P1} i_{P1} z_{P1} filters are then fitted to sinusoids of the same period, while the amplitude and phase in each filter are left as free parameters. In Table 5.7, we tabulate the ξ calculated for each filter and the best-fit period \bar{P} of each candidate: $\bar{P} = \sum_i^N (P_i)/N$, where $i = 1...N$ is index of the filter in which a coherent period has been detected, and the uncertainty of \bar{P} is determined from the

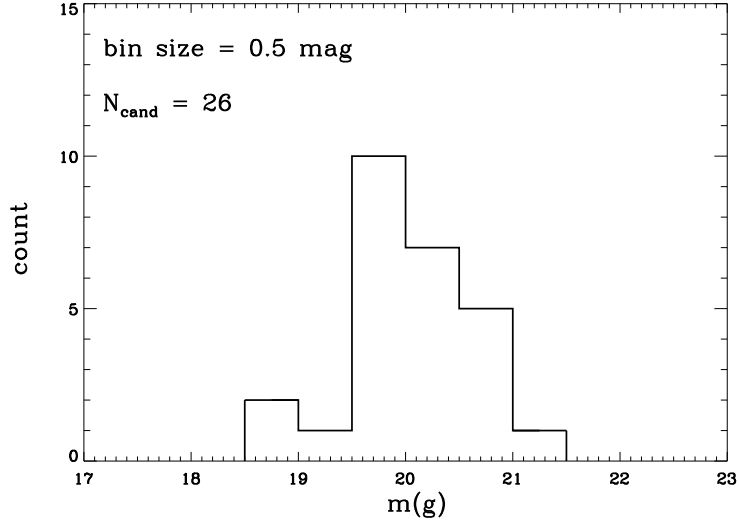


Figure 5.3: The mean g band magnitude distribution of the 26 periodic candidates. The magnitude limit of our candidate selection pipeline is ~ 20 mag.

uncertainty in each filter: $(\Delta P)^2 = (\sqrt{\sum \delta P_i^2}/N)^2 + \sum (P_i - \bar{P})^2/(N - 1)$, where the δP in each filter is given by uncertainty in the frequency $\delta\omega = 3\pi\sigma/(2\sqrt{N_0}TA)$ (Horne & Baliunas, 1986). We also list the number of cycles in Tables 5.7 and 5.8, which is simply $N_{\text{cycle}} = [\max(\text{MJD}) - \min(\text{MJD})]/\bar{P}$. In Figure 5.4, we show the distribution of the detected periods in the observed frame.

In Tables 5.9 and 5.10, we list the amplitude of the best-fit sinusoid and the mean PS1 magnitude in each filter for each candidate. To compare with the relation of variability amplitude vs. rest-frame wavelength with the previous study of normal AGNs by Vanden Berk et al. (2004), we calculate the rest wavelength for each PS1 filter at the redshift of each quasar ($\lambda_{\text{eff}}(g) = 4810 \text{ \AA}$, $\lambda_{\text{eff}}(r) = 6170 \text{ \AA}$, $\lambda_{\text{eff}}(i) = 7520 \text{ \AA}$, $\lambda_{\text{eff}}(z) = 8660 \text{ \AA}$) and define an intrinsic variability amplitude $V = \sqrt{\pi(\Delta m)^2/2 - \sigma^2}$, where here Δm is the amplitude A_0 obtained from our

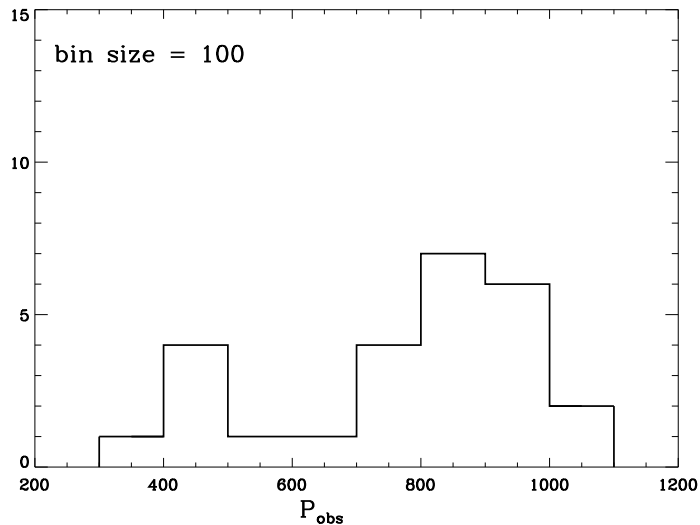


Figure 5.4: The distribution of P_{obs} , the observed period determined by the periodogram.

sinusoidal fit, and the magnitude-dependent observed scatter from stars is used as a proxy for σ (see L16). The intrinsic variability amplitude V of our candidates decreases with longer rest wavelength, which is consistent with the empirical relation from [Vanden Berk et al. \(2004\)](#) and has no apparent deviation from regular AGNs (Figure 5.5). We note, however, the exception of PSO J334.0298+0.9687, which shows much larger variability amplitudes in all filters and an apparently steeper amplitude-wavelength trend; a visual inspection of its light curves (Figure 5.25) also shows a large variation (~ 0.8 mag in the g band).

5.4.2 Spectroscopy and Black Hole Mass

We retrieved archival spectra of 16 candidates from the SDSS Science Archive Server. The remaining candidates with no archival spectra were observed at the

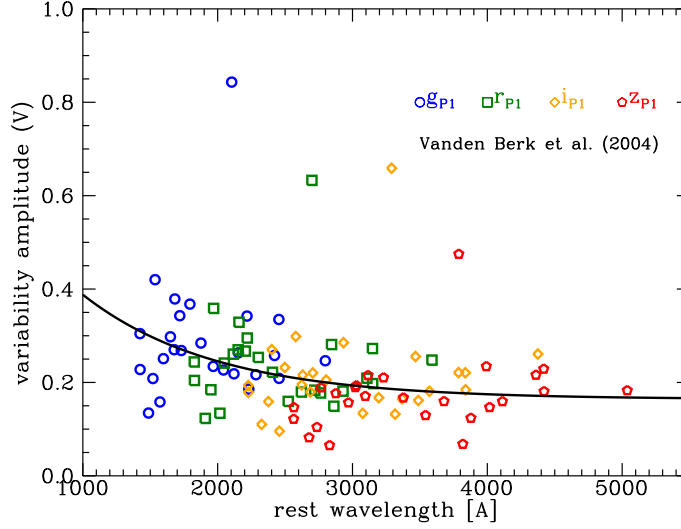


Figure 5.5: We measure the variability amplitude of each candidate in each filter after subtracting the measurement uncertainty in quadrature (g_{P1} : blue circles; r_{P1} : green squares; i_{P1} : orange diamonds; z_{P1} : red pentagons). The amplitude V decrease with longer rest wavelength, consistent with the exponential relation from [Vanden Berk et al. \(2004\)](#) (black curve).

Gemini-South Telescope (PI: Liu) or the Discovery Channel Telescope (DCT). The Gemini spectra were obtained with the R400 slit with GMOS, while the DCT spectra were obtained with the DeVeney spectrograph with a 300 g/mm grating; we summarize the details of the observations in Table 5.11. The Gemini/GMOS spectra were reduced with the Gemini IRAF package, and the DCT/DeVeney data were reduced with standard IRAF procedures.

Due to the variable weather conditions under which the spectra were taken, a standard star may not accurately calibrate the science object’s flux. Therefore,

in addition to the standard procedures to reduce the spectroscopic data, we also calibrate the object’s flux to its latest photometric measurement. We first convolve the DeVený spectrum with the SDSS r filter sensitivity curve to calculate a synthetic magnitude r'_{SDSS} ; if it differs from the latest photometric measurement r_{SDSS} by more than the variability amplitude of the object (Table 5.9) — where r_{SDSS} is either observed with DCT/LMI (see Section 5.5) or, in the absence of new observations, obtained from the SDSS Science Archive Server — we then re-normalize the spectrum to match its synthetic magnitude to r_{SDSS} . The procedure is repeated iteratively until $|r'_{\text{SDSS}} - r_{\text{SDSS}}| < 0.05$ mag. We note that this re-normalization procedure is unlikely to significantly bias our black hole mass estimates: a $\Delta m \sim 0.8$ mag intrinsic variability (which is on the order of the maximum variability amplitude in our sample of candidates) translates to a factor of ~ 2 difference in the continuum luminosity (assuming $z = 1$), which in turn corresponds to a ~ 0.2 dex error on the black hole mass — much smaller than the systematic uncertainty of Equation 5.1 or 5.2. Spectra of all candidates (including the renormalized DeVený spectra) are presented in Figures 5.27-5.30.

To measure a virial black hole mass from the spectrum, we first use the following procedure to measure the broad line width of MgII: we fit a power-law continuum in the range [2200, 2675] and [2925, 3090] Å and subtract it from the spectrum; we then broaden and scale the iron emission template from Vestergaard & Wilkes (2001) by fitting it to the range [2250, 2650] Å where iron emission is strong, which is then subtracted from the spectrum. In those spectra where S/N is low, we do not fit the iron emission to avoid over-fitting and subtracting. Next, we fit a single Gaus-

sian to the emission line in the range [2700, 2900] Å and measure a Full Width at Half Maximum (FWHM). Although [McLure & Dunlop \(2004\)](#) fit two components (broad and narrow) to the MgII line and adopt the broad component in the black hole mass estimate, we do not find a clear presence of a narrow component in every spectrum and thus only fit a single Gaussian. Then, we measure the flux density f_λ at 3000 Å in the fitted continuum and convert to a continuum luminosity: $\lambda L_\lambda = \lambda 4\pi D_L^2 f_\lambda (1+z)$. We also correct for Galactic extinction using the dust map by [Schlafly & Finkbeiner \(2011\)](#) and the extinction curve of [Cardelli et al. \(1989\)](#). Finally, we substitute the FWHM and λL_λ into the following equation from [McLure & Dunlop \(2004\)](#) to calculate the black hole mass:

$$\frac{M_{\text{BH}}}{M_\odot} = 3.2 \left(\frac{\text{FWHM}(\text{MgII})}{\text{km s}^{-1}} \right)^2 \left(\frac{\lambda L_\lambda(3000\text{\AA})}{10^{44} \text{ ergs s}^{-1}} \right)^{0.62}, \quad (5.1)$$

In a spectrum where CIV is the black hole mass estimator, we fit the continuum in the range [1445, 1465] and [1700, 1705] Å, and after subtracting the continuum, we adopt the procedure in [Shen et al. \(2008\)](#) and use a three-component fit to fully characterize the CIV line profile: a narrow component with $\text{FWHM} < 1200 \text{ km s}^{-1}$, a broad component with $\text{FWHM} > 1200 \text{ km s}^{-1}$, and a broader hump component. We then measure the FWHM from the fitted profile. The corresponding continuum luminosity is calculated from the mean flux density in the range [1340, 1360] Å, and the black hole mass estimate is adopted from [Vestergaard & Peterson \(2006\)](#):

$$\log \left(\frac{M_{\text{BH}}}{M_\odot} \right) = \log \left[\left(\frac{\text{FWHM}(\text{CIV})}{1000 \text{ km s}^{-1}} \right)^2 \left(\frac{\lambda L_\lambda(1350\text{\AA})}{10^{44} \text{ ergs s}^{-1}} \right)^{0.53} \right] + 6.66. \quad (5.2)$$

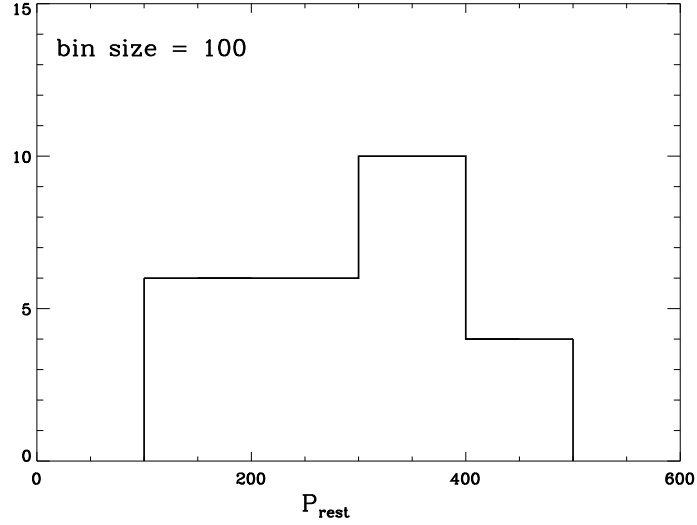


Figure 5.6: The distribution of P_{rest} ranges from $\sim 100 - 500$ days. These rest-frame periods are also tabulated in Tables 5.12 and 5.13.

The fitting procedures are demonstrated in the last two panels of Figure 5.30. The measurements of z , f_λ , FWHM, and M_{BH} are listed in Tables 5.12 and 5.13, and the distribution of rest-frame periods $P_{\text{rest}} = P_{\text{obs}}/(1+z)$ is shown in Figure 5.6. We show the distribution of the measured black hole masses in Figure 5.7.

We also compare the redshifts of the candidates from PS1 MDS with those from CRTS and PTF in Figure 5.8: our search with PS1 MDS appears to be more sensitive to candidates at higher redshifts ($\langle \bar{z} \rangle \sim 2$) than CRTS or PTF ($\langle \bar{z} \rangle \sim 1$). In fact, the redshifts of MDS candidates follow an opposite trend to those of the variable quasars that our selection pipeline can detect (see L16), suggesting a selection bias towards high redshifts.

From the black hole mass and redshift, we can infer a binary separation a via Kepler’s law, assuming the variation is on the rest-frame orbital period timescale:

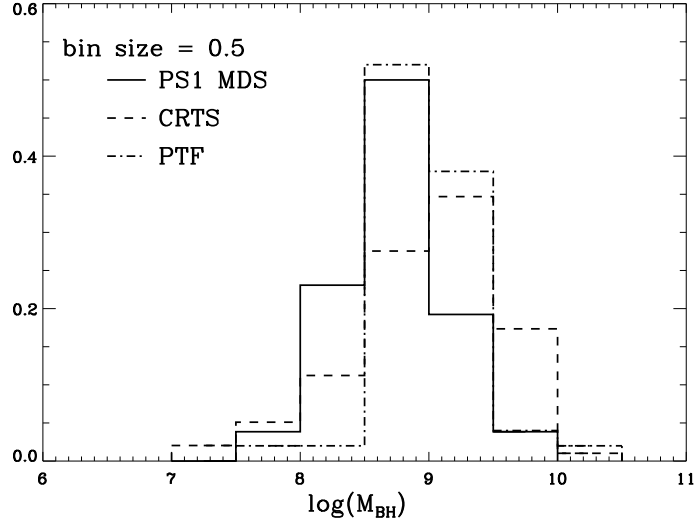


Figure 5.7: The black hole masses of the candidates from PS1 MDS are $10^8 - 10^{10} M_{\odot}$ (solid histogram). This distribution is similar to that of the candidates from [Graham et al. \(2015b\)](#) (dashed histogram) and [Charisi et al. \(2016\)](#) (dash dot histogram).

$a^3/t_{\text{orb}}^2 = GM/4\pi^2$, where $t_{\text{orb}} = P_{\text{obs}}/(1+z)$ is the rest-frame orbital period. In Figure 5.9, we show the a - M_{BH} parameter space occupied by the SMBHB candidates with more than three cycles from [Graham et al. \(2015b\)](#), [Charisi et al. \(2016\)](#), and this work. While those candidates with more than three cycles may already be in the GW-dominated regime of orbital decay, LSST will explore much larger parameter space than any of the three surveys.

5.5 Extended Baseline Photometry

As been pointed out by [Vaughan et al. \(2016\)](#), red noise can easily mimic a periodic variation over a small number of cycles (~ 3), especially when the sampling is sparse and uneven and the photometric uncertainty is large. Therefore, cur-

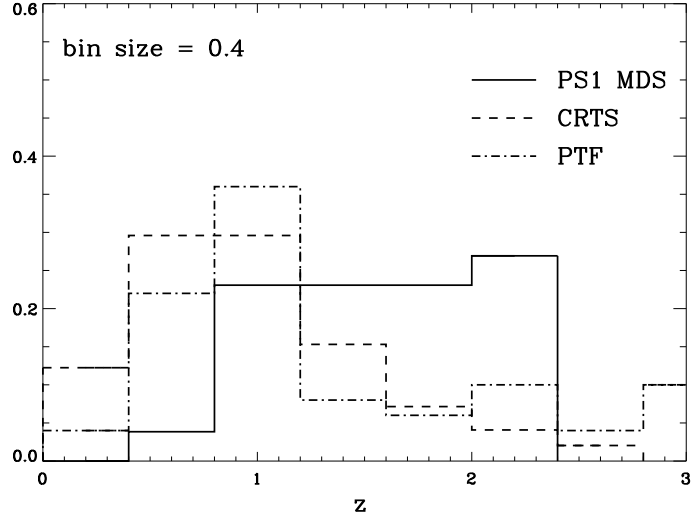


Figure 5.8: The redshift distribution of our candidates from PS1 MDS (solid histogram) shows that our selection is sensitive out to $z \sim 2$, while the redshift distributions of the periodic candidates from CRTS and PTF peak at $z \sim 1$ (dashed and dash dot histograms, respectively).

rent efforts to systematically search for periodically varying quasars (*e.g.* [Charisi et al. 2016](#); [Graham et al. 2015b](#)) are limited by the several-years-long baseline of the survey, and it is essential to test the persistence of periodicity with long-term monitoring. Our extended baseline analysis of the periodic candidates from MD09 presented in L16 and of PG 1302–102 in [Liu et al. \(2018\)](#) further demonstrated this effect, and here we present our ongoing campaign to monitor candidates from the full PS1 MDS.

New imaging data presented in this work include those taken with the Large Monolithic Imager (LMI) in g_{SDSS} r_{SDSS} i_{SDSS} z_{SDSS} filters at DCT from 2015 May to 2017 November. In Tables [5.14](#) and [5.15](#), we list the Modified Julian Dates (MJDs)

on which the observations were carried out, as well as the filters that were used. The images were reduced using standard **IRAF** routines and corrected for astrometry with **SCAMP** (Bertin, 2006). For the z_{SDSS} band images which are affected by fringe patterns, we also subtract a scaled master fringe pattern created via **create_fringes** (Snodgrass & Carry, 2013) from all z_{SDSS} band images taken on the same night and remove the fringes using the routine **remove_fringes** (Snodgrass & Carry, 2013).

We then co-add five sub-exposures in each filter (taken in a dither pattern to avoid bad pixels) with **SWARP** (Bertin et al., 2002) before performing aperture photometry using **SExtractor** (Bertin & Arnouts, 1996). Following the method described in L16, we cross-match **SExtractor** detections with an SDSS catalog of point sources from DR12 (Alam et al., 2015), resulting in ~ 200 cross-matched pairs in LMI’s $12'.3 \times 12'.3$ field of view (FOV). We exclude bright, saturated detections ($m < 16$ mag), faint objects ($m > 22$ mag), outliers, and the target itself (which is variable) and obtain a linear transformation from the **SExtractor** instrumental magnitude to an SDSS magnitude. We then apply the transformation to the target and obtain a measurement of its magnitude on the SDSS photometric system. To convert the SDSS magnitudes to the PS1 system and thus directly compare with PS1 data, we adopt the same customized method in L16 that is suitable for quasar colors. We first calculate synthetic PS1 and SDSS magnitudes by convolving the (redshifted) composite quasar spectrum from Vanden Berk et al. (2001) with the respective filter sensitivity. We then apply the PS1-SDSS magnitude offset to the LMI measurements to obtain their magnitudes on the PS1 system. Finally, we construct an extended light curve of the object by “stitching together” its PS1 light

curves and new LMI data. Those extended baseline light curves are presented in Figures 5.20 - 5.26.

We have also included data from our monitoring program with the Las Cumbres Observatory (LCO), a global network of telescopes on both hemispheres. The observations were carried out with the Spectral imager on the 2-meter class telescopes at the Haleakala Observatory on Maui, Hawaii and the Siding Spring Observatory in Australia between 2017 April and 2017 November (Project ID: NOAO2017AB-013; PI: Liu) in the g_{SDSS} and r_{SDSS} filters. The MJDs of those observations are also included in Tables 5.14 and 5.15. The LCO images have been reduced by the BANZAI pipeline and are retrieved from the LCO Science Archive. Coadding of the sub-exposures and photometry on the coadded image are then run on the same custom-developed pipeline that we apply to LMI data. However, due to the smaller FOV of the 2-m class LCO telescope ($10' \times 10'$) and shallower magnitude depth (~ 22 mag), we instead obtain $\sim 50 - 100$ SDSS-cross-matched point sources on each image, and we avoid faint detections and potential saturated detections by excluding objects with $m > 21$ mag or $m < 15$ mag when performing photometry.

We tabulate the number of cycles for each candidate on its PS1-only and extended baselines in Tables 5.7 and 5.8. While most PS1-only light curves only have $1.5 - 3$ cycles, the LMI and LCO monitoring data extended the baseline to $3 - 8$ cycles, and, in the cases where archival SDSS Stripe 82 light curves are also available, as long as ≈ 14 cycles (Figure 5.10). We have also re-calculated the S/N factor ξ on the extended baseline, by assuming a pure sinusoid with the same period as detected in the PS1-only light curve. Three candidates appears to be persistent,

having the same or improved ξ in all filters (Tables 5.7 and 5.8).

5.6 Reevaluating Periodic Candidates Using a Maximum Likelihood Method

In Section 5.3, we have assumed the null hypothesis of white noise when searching for a periodic signal using the LS periodogram. However, quasar variability is known to be stochastic and has the characteristic of “red noise”, where variability power increases on longer timescales. Here we reevaluate the significance of our periodic candidates using a maximum likelihood method and investigate whether a periodic component is justified if a red noise background is also present. We have recently applied this method to the SMBHB candidate PG 1302–102 (reported by [Graham et al. 2015a](#)) in [Liu et al. \(2018\)](#), and we refer the reader to that paper for details. Guided by the expectations when a genuine periodic signal is present in addition to DRW noise, we down-select candidates whose maximum likelihoods under the DRW model (\mathcal{L}_{DRW}) and the DRW model plus a periodic signal ($\mathcal{L}_{\text{DRW}+\text{periodic}}$) meet the following criteria:

1. $\ln \mathcal{L}_{\text{DRW}+\text{periodic}} > \ln \mathcal{L}_{\text{DRW}}$ for both PS1-only and extended light curves;
2. $(\ln \mathcal{L}_{\text{DRW}+\text{periodic}} - \ln \mathcal{L}_{\text{DRW}})_{\text{Extended}} > (\ln \mathcal{L}_{\text{DRW}+\text{periodic}} - \ln \mathcal{L}_{\text{DRW}})_{\text{PS1-only}}$;
3. $P_{\text{bestfit}} = P_{\text{LS}}$; where P_{bestfit} is determined from the maximum likelihood method, and P_{LS} is measured from the LS periodogram;

4. $p < \frac{1}{9314}$; where 9314 is the size of the initial sample of quasars, and the p -value is calculated for a χ^2 distribution of two degrees of freedom.

While 12 candidates passed Criteria (1)–(3) (Tables 5.16 and 5.17), only one (PSO J185.8689+46.9752, hereafter PSO J185) met all four criteria with such a p -value that its periodicity is unlikely due to chance alone. The PS1 and extended light curves of PSO J185 are presented in Figure 5.17, its SDSS spectrum is shown in Figure 5.18, and its LS periodogram is shown in Figure 5.19. We note that PSO J334.2028+1.4075 (L15) only passed Criteria (1), which is consistent with our previous analysis in L16 that while it has been selected as a periodic candidate over its PS1 baseline, its periodicity does not persist.

If a BPL red noise background is assumed instead, then none of the candidates are statistically significant (Tables 5.18 and 5.19). However, we note that PSO J185 is one of the eight candidates that passed Criteria (1)–(3), *i.e.* its p -value has decreased when extended data are included, and therefore could still become a significant candidate as our monitoring program continues.

Table 5.2: Medium Deep Fields by the Numbers (MD01-MD02)

| Category | Number |
|--|--------|
| MD01 | |
| PS1 point sources | 30,109 |
| PS1×CFHT quasars | 983 |
| PS1×CFHT variable quasars | 109 |
| Variable quasars with coherent periodogram peaks | 88 |
| Candidates with $\xi > 3.0$ in at least one filter | 5 |
| Candidates with $N_{\text{cycle}} > 1.5$ | 2 |
| MD02 | |
| PS1 point sources | 28,845 |
| PS1×CFHT quasars | 1,147 |
| PS1×CFHT variable quasars | 112 |
| Variable quasars with coherent periodogram peaks | 97 |
| Candidates with $\xi > 3.0$ in at least one filter | 3 |
| Candidates with $N_{\text{cycle}} > 1.5$ | 1 |

Table 5.3: Medium Deep Fields by the Numbers (MD03-MD04)

| Category | Number |
|--|--------|
| MD03 | |
| PS1 point sources | 31,350 |
| PS1×CFHT quasars | 942 |
| PS1×CFHT variable quasars | 202 |
| Variable quasars with coherent periodogram peaks | 134 |
| Candidates with $\xi > 3.0$ in at least one filter | 7 |
| Candidates with $N_{\text{cycle}} > 1.5$ | 4 |
| MD04 | |
| PS1 point sources | 32,661 |
| PS1×CFHT quasars | 1,030 |
| PS1×CFHT variable quasars | 200 |
| Variable quasars with coherent periodogram peaks | 158 |
| Candidates with $\xi > 3.0$ in at least one filter | 11 |
| Candidates with $N_{\text{cycle}} > 1.5$ | 6 |

Table 5.4: Medium Deep Fields by the Numbers (MD05-MD06)

| Category | Number |
|--|--------|
| MD05 | |
| PS1 point sources | 29,517 |
| PS1×CFHT quasars | 1,083 |
| PS1×CFHT variable quasars | 163 |
| Variable quasars with coherent periodogram peaks | 102 |
| Candidates with $\xi > 3.0$ in at least one filter | 3 |
| Candidates with $N_{\text{cycle}} > 1.5$ | 3 |
| MD06 | |
| PS1 point sources | 34,112 |
| PS1×CFHT quasars | 854 |
| PS1×CFHT variable quasars | 115 |
| Variable quasars with coherent periodogram peaks | 77 |
| Candidates with $\xi > 3.0$ in at least one filter | 1 |
| Candidates with $N_{\text{cycle}} > 1.5$ | 1 |

Table 5.5: Medium Deep Fields by the Numbers (MD07-08)

| Category | Number |
|--|--------|
| MD07 | |
| PS1 point sources | 29,031 |
| PS1×CFHT quasars | 815 |
| PS1×CFHT variable quasars | 120 |
| Variable quasars with coherent periodogram peaks | 84 |
| Candidates with $\xi > 3.0$ in at least one filter | 3 |
| Candidates with $N_{\text{cycle}} > 1.5$ | 2 |
| MD08 | |
| PS1 point sources | 38,194 |
| PS1×CFHT quasars | 1,013 |
| PS1×CFHT variable quasars | 138 |
| Variable quasars with coherent periodogram peaks | 98 |
| Candidates with $\xi > 3.0$ in at least one filter | 5 |
| Candidates with $N_{\text{cycle}} > 1.5$ | 3 |

Table 5.6: Medium Deep Fields by the Numbers (MD09-MD10)

| Category | Number |
|--|--------|
| MD09 | |
| PS1 point sources | 40,488 |
| PS1×CFHT quasars | 670 |
| PS1×CFHT variable quasars | 104 |
| Variable quasars with coherent periodogram peaks | 77 |
| Candidates with $\xi > 3.0$ in at least one filter | 6 |
| Candidates with $N_{\text{cycle}} > 1.5$ | 3 |
| MD10 | |
| PS1 point sources | 28,455 |
| PS1×CFHT quasars | 777 |
| PS1×CFHT variable quasars | 106 |
| Variable quasars with coherent periodogram peaks | 68 |
| Candidates with $\xi > 3.0$ in at least one filter | 3 |
| Candidates with $N_{\text{cycle}} > 1.5$ | 1 |
| Full MDS | |
| N_{tot} (quasar) | 9,314 |
| N_{tot} (variable) | 1,369 |
| N_{tot} (periodic) | 26 |

Table 5.7: Period, Significance Factors, and Number of Cycles of Periodic Candidates (MD01-MD04)

| PS1 Designation | $\bar{P} \pm \Delta P$ (day) | ξ (g r i z) | N_{cycle} | ξ (g r i z) | N_{cycle} |
|------------------------------|------------------------------|-------------------|--------------------|-------------------|--------------------|
| | (PS1 Only) | (PS1 Only) | (PS1 Only) | (Extended) | (Extended) |
| PSO J35.7068–4.2314 | 427±4 | (3.6 3.1 3.6 2.2) | 3.6 | (3.4 3.1 3.4 2.2) | 6.8 |
| PSO J35.8704–4.0263 | 829±23 | (3.5 3.8 3.5 2.0) | 1.9 | (3.4 3.7 3.5 2.0) | 3.5 |
| PSO J52.6172–27.6268 | 992±33 | (5.0 5.6 4.9 2.9) | 1.6 | ... | ... |
| PSO J129.4288+43.8234 | 313±5 | (2.6 3.2 1.9 1.8) | 4.9 | (2.5 3.1 1.9 1.8) | 8.8 |
| PSO J130.9953+43.7685 | 717±18 | (2.9 3.1 3.0 2.7) | 2.2 | (2.9 3.1 3.0 2.7) | 3.6 |
| PSO J131.1273+44.8582 | 843±31 | (3.5 3.5 3.0 2.1) | 1.8 | (3.4 3.3 3.0 2.1) | 3.0 |
| PSO J131.7789+45.0939 | 697±18 | (3.2 3.0 2.0 1.0) | 2.2 | (3.0 2.8 1.9 1.0) | 4.2 |
| PSO J148.8485+1.8124 | 816±5 | (3.7 4.0 2.9 1.4) | 1.9 | (3.7 3.7 2.8 1.4) | 3.2 |
| PSO J149.4989+2.7827 | 960±8 | (2.0 2.7 3.1 2.2) | 1.6 | (1.8 2.4 2.8 2.2) | 2.7 |
| PSO J149.2447+3.1393 | 810±8 | (4.0 3.1 2.0 1.2) | 1.9 | (3.8 2.8 2.0 1.2) | 3.2 |
| PSO J149.9400+1.5090 | 417±5 | (2.8 3.3 2.9 1.6) | 3.7 | (2.8 3.3 2.9 1.6) | 6.3 |
| PSO J149.6873+1.7192 | 820±5 | (2.8 4.3 4.5 3.3) | 1.9 | (2.7 4.0 4.5 3.3) | 3.6 |
| PSO J150.9191+3.3880 | 741±9 | (1.9 2.7 3.8 2.6) | 2.1 | (2.0 2.7 3.8 2.6) | 3.6 |

Table 5.8: Period, Significance Factors, and Number of Cycles of Periodic Candidates (MD05-MD10)

| PS1 Designation | $\bar{P} \pm \Delta P$ (day) | ξ (g r i z) | N_{cycle} | ξ (g r i z) | N_{cycle} |
|-----------------------|------------------------------|-------------------|--------------------|-------------------|--------------------|
| | (PS1 Only) | (PS1 Only) | (PS1 Only) | (Extended) | (Extended) |
| PSO J160.6037+56.9160 | 988±17 | (3.0 2.0 1.6 1.2) | 1.6 | (2.9 1.9 1.6 1.2) | 2.7 |
| PSO J161.2980+57.4038 | 982±10 | (3.7 3.2 2.9 1.6) | 1.6 | (3.5 3.0 2.8 1.5) | 2.6 |
| PSO J163.2331+58.8626 | 1000±13 | (2.1 3.2 3.3 2.1) | 1.5 | (2.1 3.1 3.3 2.1) | 2.7 |
| PSO J185.8689+46.9752 | 958±19 | (3.3 2.9 2.1 1.6) | 1.6 | (3.3 2.8 2.1 1.6) | 3.3 |
| PSO J213.9985+52.7527 | 727±22 | (5.2 5.0 3.7 2.5) | 2.2 | (3.4 3.1 2.8 2.0) | 4.0 |
| PSO J214.9172+53.8166 | 1003±21 | (4.0 4.4 4.0 2.4) | 1.6 | (3.5 3.8 3.7 2.3) | 3.0 |
| PSO J242.5040+55.4391 | 862±24 | (2.9 3.5 2.8 2.0) | 1.8 | (2.8 3.3 2.7 2.0) | 3.6 |
| PSO J242.8039+54.0585 | 735±22 | (3.2 2.8 2.1 1.4) | 2.1 | (3.1 2.8 2.0 1.4) | 4.2 |
| PSO J243.5676+54.9741 | 984±17 | (3.2 2.6 1.2 0.4) | 1.6 | (3.0 2.5 1.2 0.4) | 3.1 |
| PSO J333.0298+0.9687 | 428±12 | (3.5 2.8 2.8 1.1) | 3.8 | (1.9 1.9 2.0 0.9) | 15.3 |
| PSO J333.9833+1.0242 | 466±11 | (3.9 2.6 2.2 1.3) | 3.5 | (2.4 1.8 1.6 1.1) | 14.1 |
| PSO J334.2028+1.4075 | 556±17 | (3.8 2.7 1.8 0.9) | 2.8 | (3.2 2.3 1.6 0.9) | 5.4 |
| PSO J351.5679−1.6795 | 805±6 | (1.9 2.0 3.2 2.5) | 1.9 | (1.8 1.9 3.1 2.5) | 3.7 |

Table 5.9: PS1 Mean Magnitudes and Variability Amplitudes of Periodic Quasar

Candidates (MD01-05)

| PS1 Designation | m (g,r,i,z) | A_0 (g,r,i,z) |
|-----------------------|------------------------------|--------------------------|
| PSO J35.7068−4.23144 | (19.69, 19.64, 19.69, 19.53) | (0.23, 0.18, 0.23, 0.14) |
| PSO J35.8704−4.0263 | (19.52, 19.46, 19.52, 19.23) | (0.24, 0.21, 0.24, 0.13) |
| PSO J52.6172−27.6268 | (20.37, 20.20, 20.14, 19.93) | (0.34, 0.29, 0.22, 0.16) |
| PSO J129.4288+43.8234 | (19.53, 19.37, 19.50, 19.48) | (0.17, 0.16, 0.15, 0.15) |
| PSO J130.9953+43.7685 | (19.88, 19.65, 19.81, 19.88) | (0.21, 0.17, 0.18, 0.18) |
| PSO J131.1273+44.8582 | (20.57, 20.42, 20.12, 19.87) | (0.21, 0.20, 0.19, 0.15) |
| PSO J131.7789+45.0939 | (20.62, 20.29, 20.29, 20.37) | (0.22, 0.15, 0.14, 0.12) |
| PSO J148.8485+1.8124 | (20.43, 20.17, 20.10, 19.88) | (0.25, 0.20, 0.16, 0.11) |
| PSO J149.4989+2.7827 | (20.34, 20.25, 20.24, 20.04) | (0.19, 0.17, 0.15, 0.13) |
| PSO J149.2447+3.1393 | (20.72, 20.72, 20.48, 20.45) | (0.31, 0.27, 0.18, 0.17) |
| PSO J149.9400+1.5090 | (20.17, 19.91, 20.00, 20.09) | (0.18, 0.15, 0.15, 0.14) |
| PSO J149.6873+1.7192 | (20.42, 20.12, 20.08, 20.08) | (0.19, 0.15, 0.14, 0.14) |
| PSO J150.9191+3.3880 | (19.63, 19.49, 19.39, 19.20) | (0.20, 0.20, 0.21, 0.15) |
| PSO J160.6037+56.9160 | (19.52, 19.33, 19.28, 19.33) | (0.19, 0.13, 0.11, 0.11) |
| PSO J161.2980+57.4038 | (20.45, 20.44, 20.18, 20.22) | (0.28, 0.22, 0.15, 0.15) |
| PSO J163.2331+58.8626 | (19.59, 19.48, 19.43, 19.19) | (0.17, 0.15, 0.13, 0.09) |

Table 5.10: PS1 Mean Magnitudes and Variability Amplitudes of Periodic Quasar Candidates (MD06-10)

| PS1 Designation | m (g,r,i,z) | A_0 (g,r,i,z) |
|------------------------|------------------------------|--------------------------|
| PSO J185.8689+46.9752 | (20.54, 20.50, 20.23, 20.28) | (0.30, 0.21, 0.17, 0.18) |
| PSO J213.9985+52.7527 | (19.94, 20.13, 19.90, 19.89) | (0.22, 0.22, 0.16, 0.16) |
| PSO J214.9172+53.8166 | (20.53, 20.32, 20.39, 20.44) | (0.28, 0.23, 0.21, 0.20) |
| PSO J242.5040+55.4391 | (20.17, 20.17, 19.91, 19.95) | (0.22, 0.24, 0.18, 0.18) |
| PSO J242.8039+54.05853 | (19.72, 19.64, 19.87, 19.89) | (0.27, 0.22, 0.18, 0.19) |
| PSO J243.5676+54.9741 | (19.97, 19.64, 19.58, 19.61) | (0.18, 0.15, 0.11, 0.07) |
| PSO J333.0298+0.9687 | (21.42, 20.94, 20.96, 20.95) | (0.68, 0.51, 0.53, 0.39) |
| PSO J333.9832+1.0242 | (18.97, 18.85, 18.79, 18.57) | (0.11, 0.10, 0.09, 0.07) |
| PSO J334.2028+1.4075 | (19.38, 19.28, 19.14, 18.94) | (0.13, 0.11, 0.08, 0.06) |
| PSO J351.5679−1.6795 | (18.91, 18.56, 18.54, 18.67) | (0.15, 0.12, 0.13, 0.12) |

Table 5.11: Spectroscopic Follow-ups

| PS1 Designation | Telescope/Instrument | Semester or Quarter | Grating | Slit width (arcsec) | Exposure time (sec) |
|-----------------------|----------------------|--------------------------------|----------|------------------------|------------------------|
| PSO J52.6172−27.6268 | Gemini/GMOS | 16B (Gemini ID: GS-2016B-Q-50) | R400 | 0.75 | 2×1000 |
| PSO J149.2447+3.1393 | Gemini/GMOS | 15B (Gemini ID: GS-2015B-Q-42) | R400 | 0.75 | 2×1000 |
| PSO J149.6873+1.7192 | DCT/DeVeny | 17Q1 | 300 g/mm | 1.5 | 2×2000 |
| PSO J161.2980+57.4038 | DCT/DeVeny | 17Q1 | 300 g/mm | 1.5 | 2×1700 |
| PSO J163.2331+58.8626 | DCT/DeVeny | 17Q1 | 300 g/mm | 1.5 | 2×1800 |
| PSO J242.5040+55.4391 | DCT/DeVeny | 17Q1 | 300g/mm | 1.5 | 2100 |
| PSO J243.5676+54.9741 | DCT/DeVeny | 16Q3 | 300g/mm | 1.5 | 2×900 |
| PSO J333.0298+0.9687 | DCT/DeVeny | 15Q3 | 300g/mm | 1.5 | 1400 |
| PSO J334.2028+1.4075 | Gemini/GMOS | 15A (Gemini ID: GS-2015A-Q-17) | R400 | 0.75 | 720 |
| PSO J351.5679−1.6795 | DCT/DeVeny | 17Q2 | 300g/mm | 1.5 | 1200 |

Table 5.12: Spectroscopic Measurements and Inferred Binary Parameters (MD01-04)

| PS1 Designation | Spectroscopy | M_{BH} | Estimator | f_{λ} [$\text{erg s}^{-1} \text{cm}^{-2} \text{\AA}^{-1}$] | FWHM [km s^{-1}] | $\log(M_{\text{BH}})$ [M_{\odot}] | z | P_{rest} [day] | a [pc] | a |
|-----------------------|--------------|-----------------|-----------|---|--------------------------------|--|-------|----------------------------|-------------|--------------------|
| | | | | | | | | | | [R_{s}] |
| PSO J35.7068−4.23144 | SDSS | MgII | | 1.4×10^{-17} | 5185 | 8.7 | 1.564 | 167 | 0.002 | 47 |
| PSO J35.8704−4.0263 | SDSS | MgII | | 3.3×10^{-17} | 3810 | 8.8 | 1.916 | 284 | 0.004 | 55 |
| PSO J52.6172−27.6268 | GS16B | MgII | | 1.3×10^{-17} | 7384 | 9.2 | 2.134 | 317 | 0.005 | 32 |
| PSO J129.4288+43.8234 | SDSS | MgII | | 4.5×10^{-17} | 3744 | 8.3 | 0.959 | 160 | 0.002 | 80 |
| PSO J130.9953+43.7685 | SDSS | MgII | | 4.1×10^{-17} | 3850 | 8.4 | 0.986 | 361 | 0.003 | 133 |
| PSO J131.1273+44.8582 | SDSS | MgII | | 1.6×10^{-17} | 2450 | 8.3 | 2.011 | 280 | 0.002 | 126 |
| PSO J131.7789+45.0939 | SDSS | MgII | | 2.0×10^{-17} | 6773 | 8.8 | 1.233 | 312 | 0.004 | 58 |
| PSO J148.8485+1.8124 | SDSS | MgII | | 7×10^{-18} | 5402 | 8.9 | 2.378 | 242 | 0.003 | 45 |
| PSO J149.4989+2.7827 | SDSS | CIV | | 3.4×10^{-17} | 5173 | 9.1 | 2.376 | 284 | 0.004 | 38 |
| PSO J149.2447+3.1393 | GS15B | MgII | | 8.6×10^{-17} | 1955 | 8.5 | 1.859 | 283 | 0.003 | 94 |
| PSO J149.9400+1.5090 | SDSS | MgII | | 2.4×10^{-17} | 3715 | 8.3 | 1.106 | 198 | 0.002 | 102 |
| PSO J149.6873+1.7192 | DCT17Q1 | MgII | | 1.3×10^{-17} (n) | 5755 | 8.6 | 1.354 | 348 | 0.004 | 85 |
| PSO J150.9191+3.3880 | SDSS | MgII | | 6.9×10^{-17} | 1995 | 7.7 | 0.719 | 431 | 0.002 | 426 |

Table 5.13: Spectroscopic Measurements and Inferred Binary Parameters (MD05-10)

| PS1 Designation | Spectroscopy | M_{BH} | Estimator | f_{λ} [$\text{erg s}^{-1} \text{cm}^{-2} \text{\AA}^{-1}$] | FWHM [km s^{-1}] | $\log(M_{\text{BH}})$ [M_{\odot}] | z | P_{rest} [day] | a [pc] | a [R_{s}] |
|-----------------------|--------------|-----------------|-----------|---|--------------------------------|--|-------|----------------------------|-------------|---------------------------|
| PSO J160.6037+56.9160 | SDSS | MgII | | 3.7×10^{-17} | 3251 | 8.5 | 1.445 | 404 | 0.004 | 119 |
| PSO J161.2980+57.4038 | DCT17Q1 | MgII | | $2.0 \times 10^{-17}(\text{n})$ | 3043 | 8.5 | 1.798 | 351 | 0.003 | 114 |
| PSO J163.2331+58.8626 | DCT17Q1 | CIV | | $6.7 \times 10^{-17}(\text{n})$ | 5611 | 9.2 | 2.165 | 316 | 0.005 | 33 |
| PSO J185.8689+46.9752 | SDSS | MgII | | 1.3×10^{-17} | 6070 | 8.9 | 1.681 | 357 | 0.004 | 59 |
| PSO J213.9985+52.7527 | SDSS | MgII | | 1.5×10^{-17} | 4123 | 8.7 | 1.867 | 253 | 0.003 | 67 |
| PSO J214.9172+53.8166 | SDSS | MgII | | 1.5×10^{-17} | 4907 | 8.4 | 1.169 | 462 | 0.004 | 142 |
| PSO J242.5040+55.4391 | DCT17Q1 | MgII | | $1.9 \times 10^{-17}(\text{n})$ | 5547 | 8.9 | 1.780 | 310 | 0.004 | 53 |
| PSO J242.8039+54.0585 | SDSS | MgII | | 3.6×10^{-17} | 6581 | 8.8 | 0.960 | 375 | 0.004 | 70 |
| PSO J243.5676+54.9741 | DCT16Q3 | MgII | | $3.5 \times 10^{-17}(\text{n})$ | 2041 | 8.0 | 1.268 | 434 | 0.002 | 280 |
| PSO J333.0298+0.9687 | DCT15Q3 | Mg II | | 2.4×10^{-17} | 8851 | 9.2 | 1.284 | 244 | 0.004 | 28 |
| PSO J333.9833+1.0242 | SDSS | MgII | | 4.2×10^{-17} | 6157 | 9.5 | 2.234 | 144 | 0.003 | 13 |
| PSO J334.2028+1.4075 | GS15A | Mg II | | 1.9×10^{-17} | 5492 | 9.1 | 2.070 | 182 | 0.003 | 28 |
| PSO J351.5679-1.6795 | DCT17Q2 | MgII | | 10.7×10^{-17} | 4702 | 8.9 | 1.156 | 373 | 0.005 | 59 |

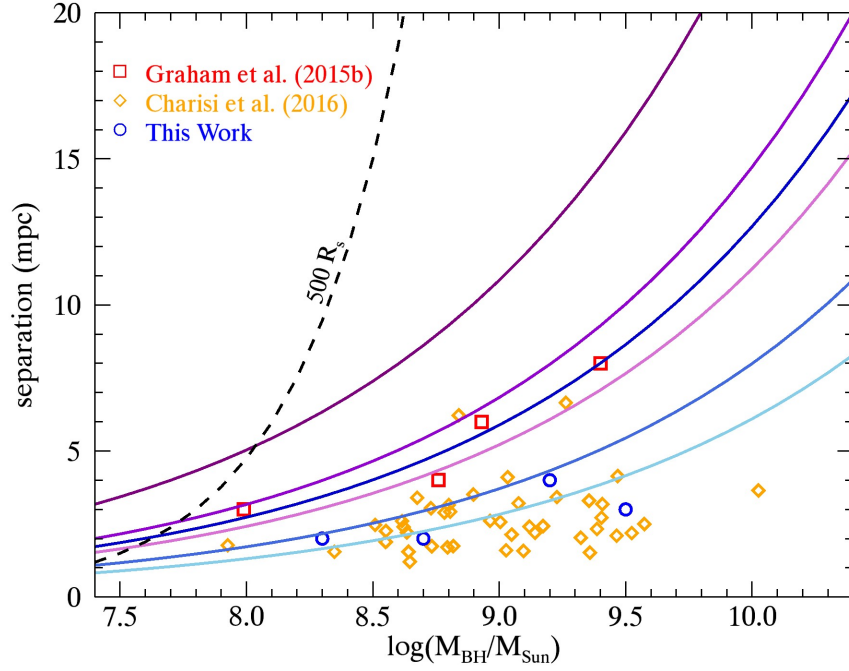


Figure 5.9: The blue solid curves represent the $M_{\text{BH}} - a$ detection limit if we require 3 cycles of periodic variation over a 4-year baseline (*i.e.* sources located below the curves have more than 3 cycles over the baseline); curves from dark to light shades correspond to $z = 0, 1, 2$. The purple solid curves correspond to 3 cycles over 10 years (*i.e.* LSST); from dark to light shades: $z = 0, 1, 2$. The black dashed curve represents a binary separation of $500 R_S$, which we use as fiducial value within which the binary is in the gravitational wave driven regime (*i.e.* candidates that are below the black dashed curve). Only a small number of candidates from the three surveys satisfy the 3-cycle requirement (assuming 4-year MDS and PTF baselines and a 9-year CRTS baseline). LSST, however, will be able to detect periodic candidates in a larger part of the $a - M_{\text{BH}}$ parameter space, many of them will be in the GW-driven regime.

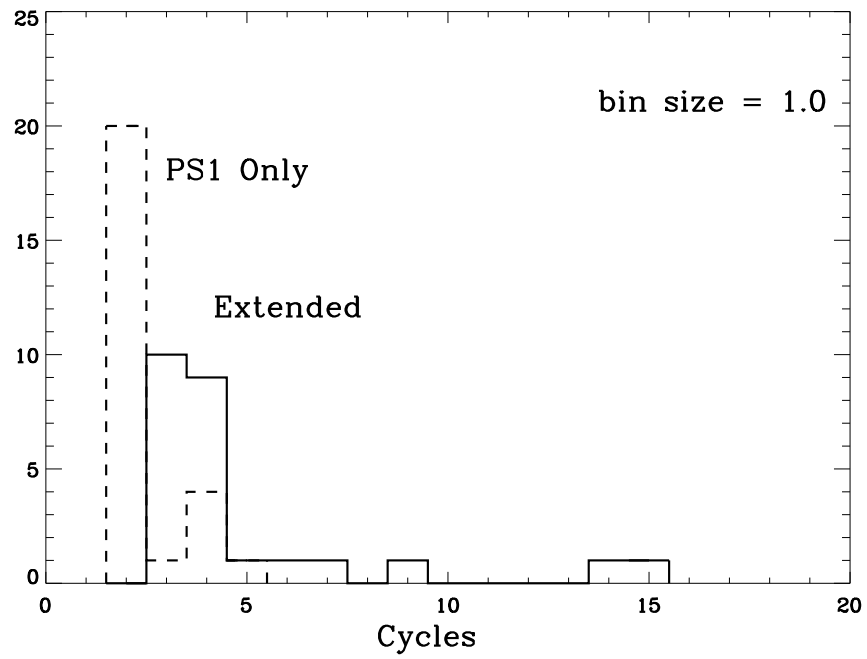


Figure 5.10: While most candidates have only ~ 2 cycles in their PS1-only light curves, we have extended the baseline to > 3 cycles with new imaging data from DCT/LMI and LCO/Spectral and archival SDSS data.

Table 5.14: Extended Baseline Monitoring of Candidates (MD01-MD04)

| PS1 Designation | Telescope/Instrument | MJD(s) of follow-up observation(s) | Filters |
|-----------------------|-----------------------|------------------------------------|---------|
| PSO J35.7068−4.23144 | DCT/LMI, LCO/Spectral | 57641, 57682, 57940, 57993 | g r i z |
| PSO J35.8704−4.0263 | DCT/LMI, LCO/Spectral | 57641, 57682, 57939 | g r i z |
| PSO J52.6172−27.6268 | ... | ... | ... |
| PSO J129.4288+43.8234 | DCT/LMI, LCO/Spectral | 57682, 57901 | g r i z |
| PSO J130.9953+43.7685 | DCT/LMI | 57682, 57741 | g r i z |
| PSO J131.1273+44.8582 | DCT/LMI | 57682 | g r i z |
| PSO J131.7789+45.0939 | DCT/LMI | 57682, 57741, 58075 | g r i z |
| PSO J148.8485+1.8124 | DCT/LMI | 57787 | r i |
| PSO J149.4989+2.7827 | DCT/LMI | 57787 | g r i |
| PSO J149.2447+3.1393 | DCT/LMI | 57369, 57788 | g r i z |
| PSO J149.9400+1.5090 | DCT/LMI | 57788 | g r i z |
| PSO J149.6873+1.7192 | DCT/LMI | 57788, 58075 | g r |
| PSO J150.9191+3.3880 | DCT/LMI, LCO/Spectral | 57833, 57845 | g r i z |

Table 5.15: Extended Baseline Monitoring of Candidates (MD05-MD10)

| PS1 Designation | Telescope/Instrument | MJD(s) of follow-up observation(s) | Filters |
|-----------------------|-----------------------|--|---------|
| PSO J160.6037+56.9160 | DCT/LMI, LCO/Spectral | 57741, 57852 | g r i z |
| PSO J161.2980+57.4038 | DCT/LMI | 57741 | g r i z |
| PSO J163.2331+58.8626 | DCT/LMI, LCO/Spectral | 57741, 57851 | g r i z |
| PSO J185.8689+46.9752 | DCT/LMI, LCO/Spectral | 57833, 57858 , 58075 | g r i z |
| PSO J213.9985+52.7527 | DCT/LMI | 57833 | g r i z |
| PSO J214.9172+53.8166 | DCT/LMI, LCO/Spectral | 57170, 57284, 57369, 57522, 57977 | g r i z |
| PSO J242.5040+55.4391 | DCT/LMI, LCO/Spectral | 57522, 57578, 57642, 57851 , 57977 , 58012 | g r i z |
| PSO J242.8039+54.0585 | DCT/LMI, LCO/Spectral | 57522, 57579, 57641, 57851 , 57977 , 58012 | g r i z |
| PSO J243.5676+54.9741 | DCT/LMI, LCO/Spectral | 57522, 57579, 57851 , 57901 , 57976 , 58012 | g r i z |
| PSO J333.0298+0.9687 | DCT/LMI, LCO/Spectral | 57579, 57641, 57940 , 57990 , 58012, 58016 | g r i z |
| PSO J333.9832+1.0242 | DCT/LMI | 57579, 57641, 57935, 58016 | g r i z |
| PSO J334.2028+1.4075 | DCT/LMI | 57170, 57282, 57284, 57523, | g r i z |
| | | 57579, 57641, 57682, 57990 , 57935 , 58016 | |
| PSO J351.5679−1.6795 | DCT/LMI, LCO/Spectral | 57578, 57641, 57682, 57940 , 57985 , 58016 | g r i z |

Table 5.16: Re-analyses Using the Maximum Likelihood Method under the DRW Model (MD01-MD04)

| PS1 Designation | $\ln \mathcal{L}_{\text{DRW}}$ (PS1 Only) | $\ln \mathcal{L}_{\text{DRW+p}}$ (PS1 Only) | P [day] (PS1 Only) | p -value (PS1 Only) | $\ln \mathcal{L}_{\text{DRW}}$ (Ext.) | $\ln \mathcal{L}_{\text{DRW+p}}$ (Ext.) | P [day] (Ext.) | p -value (Ext.) |
|------------------------------|--|--|------------------------------|--------------------------|--|--|------------------------------|-----------------------|
| PSO J35.7068–4.2314 | 123.199 | 125.139 | $436.10^{+350.50}_{-169.49}$ | 0.143 | 144.519 | 150.933 | $426.22^{+213.63}_{-336.36}$ | 0.00163 |
| PSO J35.8704–4.0263 | 131.743 | 137.596 | $953.43^{+9.75}_{-240.24}$ | 0.00287 | 150.884 | 157.592 | $878.89^{+74.18}_{-15.81}$ | 0.00122 |
| PSO J52.6172–27.6268 | 88.442 | 95.024 | $953.20^{+15.16}_{-34.83}$ | 0.00138 | ... | ... | ... | ... |
| PSO J129.4288+43.8234 | 146.559 | 146.866 | $412.99^{+192.45}_{-277.54}$ | 0.735 | 144.646 | 146.082 | $230.54^{+218.78}_{-211.21}$ | 0.237 |
| PSO J130.9953+43.7685 | 139.766 | 142.989 | $658.15^{+310.40}_{-349.59}$ | 0.0398 | 159.584 | 166.840 | $721.75^{+190.72}_{-29.27}$ | 7.06×10^{-4} |
| PSO J131.1273+44.8582 | 121.928 | 125.289 | $845.20^{+113.61}_{-566.38}$ | 0.0347 | 136.706 | 141.580 | $967.15^{+4.20}_{-55.79}$ | 0.00764 |
| PSO J131.7789+45.0939 | 113.227 | 122.755 | $694.46^{+259.30}_{-40.69}$ | 7.27×10^{-5} | 140.334 | 145.664 | $801.40^{+49.08}_{-140.911}$ | 0.00484 |
| PSO J148.8485+1.8124 | 115.019 | 120.755 | $829.88^{+50.10}_{-59.89}$ | 0.00322 | 134.159 | 138.174 | $885.46^{+80.96}_{-279.03}$ | 0.0180 |
| PSO J149.4989+2.7827 | 113.043 | 121.036 | $873.75^{+35.77}_{-44.22}$ | 3.37×10^{-4} | 127.629 | 131.386 | $966.54^{+0}_{-80.76}$ | 0.0233 |
| PSO J149.2447+3.1393 | 101.544 | 108.689 | $929.64^{+41.27}_{-28.72}$ | 7.88×10^{-4} | 99.573 | 103.032 | $916.98^{+51.74}_{-118.25}$ | 0.0314 |
| PSO J149.9400+1.5090 | 131.136 | 131.962 | $332.23^{+340.78}_{-329.21}$ | 0.437 | 149.546 | 151.097 | $408.28^{+238.52}_{-381.47}$ | 0.212 |
| PSO J149.6873+1.7192 | 105.086 | 111.844 | $812.11^{+93.47}_{-56.52}$ | 0.00116 | 136.715 | 145.201 | $864.87^{+32.49}_{-17.50}$ | 2.06×10^{-4} |
| PSO J150.9191+3.3880 | 94.701 | 95.448 | $768.34^{+134.88}_{-145.11}$ | 0.4737 | 109.721 | 111.391 | $708.60^{+241.80}_{-158.19}$ | 0.188 |

Table 5.17: Re-analyses Using the Maximum Likelihood Method under the DRW Model (MD05-MD10)

| PS1 Designation | $\ln \mathcal{L}_{\text{DRW}}$ (PS1 Only) | $\ln \mathcal{L}_{\text{DRW}+\text{p}}$ (PS1 Only) | P [day] (PS1 Only) | p -value (PS1 Only) | $\ln \mathcal{L}_{\text{DRW}}$ (Ext.) | $\ln \mathcal{L}_{\text{DRW}+\text{p}}$ (Ext.) | P [day] (Ext.) | p -value (Ext.) |
|-------------------------------|--|---|------------------------------|--------------------------|--|---|------------------------------|-----------------------|
| PSO J160.6037+56.9160 | 160.342 | 162.407 | $840.95^{+124.35}_{-135.64}$ | 0.126 | 159.561 | 162.939 | $885.10^{+78.26}_{-341.73}$ | 0.0341 |
| PSO J161.2980+57.4038 | 120.002 | 127.036 | $850.52^{+79.49}_{-180.50}$ | 8.8×10^{-4} | 104.117 | 106.059 | $759.86^{+212.38}_{-197.61}$ | 0.1434 |
| PSO J163.2331+58.8626 | 157.293 | 158.086 | $948.16^{+22.23}_{-177.76}$ | 0.452 | 158.228 | 159.103 | $294.14^{+181.23}_{-268.76}$ | 0.416 |
| PSO J185.8689+46.9752* | 112.525 | 114.019 | $279.05^{+603.95}_{-166.04}$ | 0.224 | 112.272 | 122.465 | $954.32^{+17.41}_{-22.58}$ | 3.74×10^{-5} |
| PSO J213.9985+52.7527 | 146.229 | 154.131 | $768.64^{+159.95}_{-410.04}$ | 3.7×10^{-4} | 142.168 | 148.269 | $686.37^{+20.72}_{-29.27}$ | 0.00224 |
| PSO J214.9172+53.8166 | 118.971 | 120.498 | $89.91^{+315.98}_{-44.01}$ | 0.217 | 120.820 | 122.185 | $892.77^{+70.37}_{-129.62}$ | 0.255 |
| PSO J242.5040+55.4391 | 150.588 | 155.394 | $950.25^{+20.73}_{-39.26}$ | 0.00818 | 172.481 | 174.968 | $881.85^{+78.69}_{-91.30}$ | 0.0831 |
| PSO J242.8039+54.0585 | 140.902 | 146.990 | $720.49^{+40.56}_{-39.43}$ | 0.00226 | 170.788 | 176.619 | $725.43^{+95.77}_{-34.22}$ | 0.00293 |
| PSO J243.5676+54.9741 | 152.054 | 152.959 | $113.69^{+295.66}_{-84.33}$ | 0.404 | 184.189 | 186.841 | $189.08^{+155.22}_{-164.77}$ | 0.0705 |
| PSO J333.0298+0.9687 | 62.335 | 63.660 | $408.09^{+365.78}_{-254.21}$ | 0.265 | 106.265 | 107.822 | $971.06^{+0}_{-230.31}$ | 0.210 |
| PSO J333.9832+1.0242 | 181.015 | 184.466 | $466.40^{+298.54}_{-441.45}$ | 0.0317 | 242.674 | 248.747 | $442.39^{+464.69}_{-15.30}$ | 0.00230 |
| PSO J334.2028+1.4075 | 164.979 | 167.303 | $578.32^{+108.16}_{-441.83}$ | 0.0978 | 214.130 | 215.850 | $695.27^{+262.37}_{-127.62}$ | 0.179 |
| PSO J351.5679-1.6795 | 117.924 | 124.945 | $814.33^{+140.21}_{-89.78}$ | 8.92×10^{-4} | 81.783 | 88.879 | $826.42^{+67.75}_{-22.24}$ | 8.28×10^{-4} |

5.7 Discussion

In Section 5.6, we have applied a more rigorous method and selected one statistically-significant candidate which is preferred by the DRW+periodic model and 12 candidates that are consistent with the expectations for a true periodic signal (and eight if BPL noise is assumed instead). In this Section, we discuss the astrophysical implications: how does our detection rate of SMBHB candidates compare with previous work? Are these variability-selected SMBHB candidates from PS1 MDS within the reach of current and future pulsar timing array experiments? Given the capabilities of the Large Synoptic Survey Telescope, how many periodic quasars can it detect?

5.7.1 The Detection Rate of SMBHBs

Boroson & Lauer (2009) (hereafter BL09) searched for SDSS quasars that have multiple redshift systems, which could indicate the presence of a binary, and there are two candidates that show such features from $\sim 17,500$ SDSS quasars at $z < 0.7$. This rate ($\sim 0.01\%$) is consistent with the results from Volonteri et al. (2009) (hereafter VMD09), who predicted an upper limit of $\sim 0.1\%$ per quasar for $z < 0.7$ or $\sim 1\%$ for $z < 1$.

To compare with the results from BL09, we calculate the cumulative number of SMBHB candidates ($N(< z)$) per 1,000 quasars included in the search in PS1 MDS. We also compare with previous work by Graham et al. (2015b) (hereafter G15) and Charisi et al. (2016) (hereafter C16): G15 searched among $\approx 243,000$

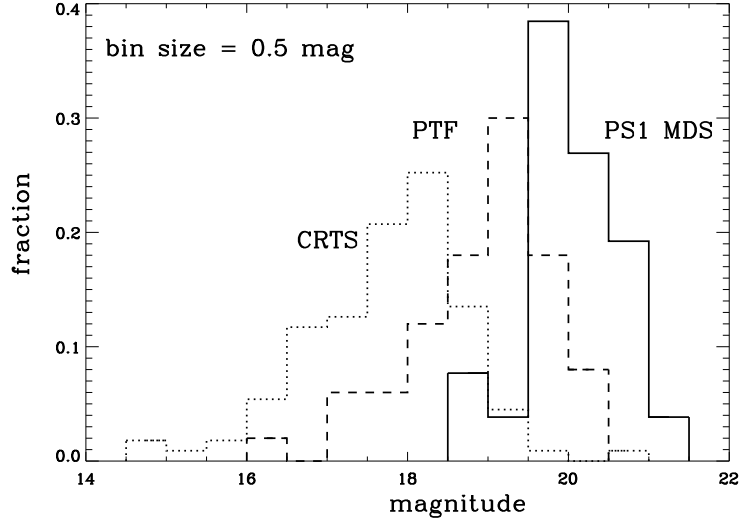


Figure 5.11: Dotted histogram: V band magnitude distribution of the candidates from CRTS (G15). Dashed histogram: the R magnitude distribution of the candidates from PTF (C16). Solid histogram: the g_{PS1} magnitude distribution of candidates from this work (also shown in Figure 5.3).

spectroscopically confirmed quasars and claimed 111 candidates; 50 candidates from C16 were selected among $\approx 35,000$ spectroscopic quasars (33 after re-analysis with extended data).

We first calibrate the completeness of G15 and C16 in detecting periodic quasars relative to this work: our candidates have a magnitude cut-off at $m \sim 20$ mag (Figure 5.3), which results in our sensitivity out to $z \sim 2$ (Figure 5.8). Assuming this work is complete out to $z \sim 2$ and the candidates from G15 and C16 are relatively complete down to $m \sim 18$ mag and $m \sim 19$ mag, respectively (Figure 5.11), that translates to a redshift limit at $z \sim 1.0$ for G15 and $z \sim 1.4$ for C16. We then calculate $N(< z)$ out to the redshift that each search is complete (relative to

this work) by counting the total number of $< z$ candidates that is in the respective sample.

We note that from our down-selection criteria outlined in Section 5.6, six candidates passed Criteria (1)-(3) under both DRW and BPL models. They are still consistent with the expectation that new data should strengthen the evidence when a genuine periodic signal is present (Liu et al., 2018), and with more extended data from our ongoing monitoring program, the p -value is expected to further decrease if the periodicity persists. Since at most six candidates can potentially be statistically significant, we use them to calculate an upper limit, which corresponds to an SMBHB rate of 0.6 per 1,000 quasars. The cumulative rate inferred from C16 has a higher value out to a lower redshift and is tension with our rate (Figure 5.12, left panel).

We also compare the number of SMBHB candidates per deg^2 of sky area searched (Figure 5.12, right panel). We performed our search in the cross-matched area between the PS1 MDS and PS1 \times CFHT catalogs, which covers an area of $\sim 50 \text{ deg}^2$. This corresponds to a rate of < 0.12 SMBHBs per deg^2 (out to $z \sim 2$). To compare with the predicted observability of periodic sources, we adopt the fiducial values in Haiman et al. (2009) (hereafter HKM09), for which we expect 20 sources varying at 245 days in a 10^4 deg^2 sky area for a survey magnitude depth of 22 mag (which is the magnitude limit of our candidate selection). Since most of our candidates vary on the timescale of ~ 800 days (Figure 5.4), we then apply the scaling relation for a population of purely GW-driven SMBHBs to calculate the expected number of periodic quasars, *i.e.* $(800/245)^{8/3} \times 0.002 = 0.05$, which is consistent with our upper limit (Figure 5.12, right panel). We note the caveat,

however, that the redshift of the sources from HKM09 is fixed at $z = 2$, while we have measured a cumulative rate *out to* $z = 2$. We have also compared with the predicted upper limit from VMD09 of ~ 0.1 per deg^2 out to $z = 1$, and our measured rate is still consistent with this upper limit².

5.7.2 Implications for Gravitational Wave Astrophysics in the PTA Regime

SMBHBs are potential sources of gravitational waves (GW) in the nanohertz frequencies ($10^{-9} - 10^{-7}$ Hz). In the late 70s, [Sazhin \(1978\)](#) and [Detweiler \(1979\)](#) realized that GW signals would appear in the times of arrival (TOAs) of pulsar signals as “unexplained” residuals, after subtracting a timing model from the observed TOA. For a number of pulsars distributed across the sky, their timing residuals should correlate with their angular separations on the sky ([Hellings & Downs, 1983](#)). There are currently three pulsar timing array (PTA) experiments dedicated to using well-timed pulsars to detect this effect induced by GWs — the North American Nanohertz Observatory for Gravitational Waves (NANOGrav; [McLaughlin 2013](#)), the European Pulsar Timing Array (EPTA; [Kramer & Champion 2013](#)), and the Parkes Pulsar Timing Array (PPTA; [Hobbs 2013](#)) — and they combine to form the International Pulsar Timing Array (IPTA; [Hobbs et al. 2010](#)). In the PTA regime, SMBHBs could appear as individual continuous wave (CW) sources, or contribute to a stochastic gravitational wave background (GWB). Those PTA experiments,

²However, we note that the VMD09 prediction is motivated by SMBHBs with broad emission line features and not optical periodicity.

having operated for ~ 10 years, have started to put meaningful constraints on the strain amplitudes of CW sources (Arzoumanian et al., 2014; Babak et al., 2016; Zhu et al., 2014) and the GWB (Arzoumanian et al., 2016; Lentati et al., 2015; Shannon et al., 2015).

Recently, Perera et al. (2018) have placed upper limits on the SMBHB candidates from G15, C16, and L16³, and here we calculate the GW strain amplitudes of the 26 candidates and compare them with this upper limit. For an SMBHB in a circular orbit, the strain is given by:

$$h = \frac{2\pi^{2/3}G^{5/3}(f_{\text{GW}})^{2/3}(M_{\text{ch}})^{5/3}}{c^4d_{\text{L}}}, \quad (5.3)$$

where the observed gravitational wave frequency $f_{\text{GW}} = 2f_{\text{orb}}$, M_{ch} is the chirp mass: $M_{\text{ch}} = (M_1M_2)^{3/5}(M_1 + M_2)^{-1/5}$, and d_{L} is the luminosity distance of the source. As shown in Figure 5.13, the strain amplitudes of our SMBHB candidates from PS1 MDS are lower than this upper limit by $\sim 2 - 4$ orders of magnitude and therefore cannot be detected as individual CW sources by the current PTAs.

5.7.3 Periodic Quasar Detections in the LSST Era

Expected to start its operation in ~ 2022 , the Large Synoptic Survey Telescope (LSST; Ivezić et al. 2008) will be thousands of times more powerful than PS1 MDS, thanks to its magnitude depth, photometric precision, and large survey area (Table 5.20). Here, we explore its capabilities to detect periodic quasars by using our results

³We note that PSO J334.2028+1.4075, which is included in both L15 and L16, has a lower BH mass in L16 which was measured from its Gemini spectrum.

from PS1 MDS as a benchmark. The notation \tilde{N} represents the number of quasars from a simulated population, while N is the observed or expected number from a survey.

Following the method in L16, we first simulate a population of quasars from $0.3 < z < 3.1$ given the quasar luminosity function. We then apply the magnitude cut at $m < 25$ mag (Table 5.20); from $\tilde{N}_{\text{tot,LSST}} = 8,996$ simulated quasars, $\tilde{N}_{\text{sel,LSST}} = 1,700$ quasars can be “visible” in the survey (Figure 5.14). Next, we assign a variability amplitude to each quasar based on the same amplitude–absolute magnitude relation from Heinis et al. (2016b). To determine the variability detection threshold, we adopt the expected photometric error as a function of magnitude from Ivezić et al. (2008):

$$\sigma^2 = \sigma_{\text{sys}}^2 + (0.04 - \gamma)10^{0.4(m-m_5)} + \gamma 10^{0.8(m-m_5)}, \quad (5.4)$$

From the same simulation performed for MDS in L16, the $\tilde{N}_{\text{sel,MDS}} = 924$ quasar are selected from an initial sample of $\tilde{N}_{\text{tot,MDS}} = 8,996$. To estimate the total number of quasars in the LSST footprint, we simply scale up the number of quasars selected in MDS ($N_{\text{sel,MDS}} = 9,314$) by the survey area A (Table 5.20):

$$N_{\text{tot,LSST}} = N_{\text{sel,MDS}} \times \frac{\tilde{N}_{\text{tot,MDS}}}{\tilde{N}_{\text{sel,MDS}}} \times \frac{A(\text{LSST})}{A(\text{MDS})} = 3.63 \times 10^7 \quad (5.5)$$

Since $\tilde{N}_{\text{var,LSST}} = 1,199$ quasars are selected as variables from $\tilde{N}_{\text{tot,LSST}} = 8,996$ quasars from our simulation, the number of variable quasars that can be detected by LSST is:

$$N_{\text{var,LSST}} = N_{\text{tot,LSST}} \times \frac{\tilde{N}_{\text{var,LSST}}}{\tilde{N}_{\text{tot,LSST}}} = 4.84 \times 10^6. \quad (5.6)$$

Assuming the same periodic candidate selection method (which selected 26 candidates from $N_{\text{var,MDS}} = 1,369$ quasars, out of which $N_{\text{cand,MDS}} = 3$ is persistent over a baseline spanning 3 cycles, Table 5.7) is applied to LSST variable quasars, the number of periodic candidates it could yield is:

$$N_{\text{cand,LSST}} = N_{\text{var,LSST}} \times \frac{N_{\text{cand,MDS}}}{N_{\text{var,MDS}}} \approx 10,600, \quad (5.7)$$

a factor of ~ 50 more than the number of SMBHB candidates from G15, C16, and this work combined.

We also estimated the part of the $h - f_{\text{GW}}$ parameter space that LSST can explore. For simplicity, we adopt the mean redshift of the variable quasars from our simulation of LSST quasars: $z_{\text{LSST}} = 1.6$. The distribution of absolute magnitudes to which LSST is sensitive ($-17 < M < -27$) corresponds to a black hole mass range $6.5 < \log(M_{\text{BH}}(M_{\odot})) < 9.6$ (which is calculated using the quasar sample from Peng et al. 2006). To determine the range of gravitational wave frequencies to which it is sensitive, we assume at least 3 cycles over its 10-year baseline and adopt a ~ 20 -day cadence for LSST.

To compare them with parameters that CRTS is sensitive to, we take M_{BH} to range from the the black hole mass that corresponds to 3σ below the mean to the maximum mass of the G15 sample, *i.e.* $7.5 < \log(M_{\text{BH}}) < 10.2$, and adopt its mean redshift $z = 1.0$. We also require at least 3 cycles over its 9-year baseline and adopt

a 11-day cadence for CRTS. By comparison, the MDS parameter space is calculated for the mean redshift of the simulated variable quasar sample ($z_{\text{MDS}} = 1.0$), at least 3 cycles over a 4-year baseline, and a typical 3-day cadence. We assumed $q = 1$ in calculating the chirp mass M_{ch} from M_{BH} , and those parameters of z , M_{ch} , and f_{GW} are listed in Table 5.21.

We then compare those parameters with those of the first most likely CW sources calculated for the IPTA and simulated SKA arrays from Rosado et al. (2015): for each of the parameters $\log z$, $\log M_{\text{ch}}$, and $\log f_{\text{GW}}$, we approximate the probability density of the first likely sources as a Gaussian and draw $\sim 300 - 400$ SMBHB realizations from the distribution. The minimum and maximum values of each parameter are listed in Table 5.21, as well as the number of realizations of SMBHB sources for each PTA array. As shown in Figure 5.15, the SMBHB candidates from PS1 MDS with more than 3 cycles are unlikely to be detected as individual sources by IPTA or the SKA arrays due to their higher GW frequencies; neither are the current $N > 3$ cycles CRTS candidates⁴ likely to be detected by IPTA. However, candidates occupying the LSST parameter space might be detectable by the SKA array: if LSST yields SMBHBs candidates that are nearby ($z < 0.5$), massive ($\log(M_{\text{BH}}) \sim 9$), and at long orbital periods ($f_{\text{GW}} \sim 10$ nHz), they are the best contestants for the first individual CW sources detectable by the SKA.

⁴Only candidates with black hole masses in G15 are included.

5.7.4 Probing the SED Properties of SMBHBs

While a long baseline is essential to break false signals due to red noise and help to verify the variability behavior of SMBHB candidates (Sections 5.5 and 5.6), analyses of these systems based on optical variability alone may not suffice to identify robust SMBHB candidates, and follow-up multi-wavelength studies are needed to independently verify an SMBHB candidate.

For example, Roedig et al. (2014) have predicted a deficit in the spectrum (“notch”), due to missing radiation from the cavity in the circumbinary disk. For typical SMBHB parameters, the notch is expected in the UV band⁵. However, a multi-wavelength study of the SMBHB candidate PSO J334.2028+1.4075 (hereafter PSO J334) by Foord et al. (2017) shows that its spectral energy distribution (SED) is consistent with that of a radio-quiet quasar⁶ and does not show evidence for the predicted notch. Since PSO J334 has been disfavored as a periodic source by L16 and this work, we now explore any possible notch for the best candidate from our PS1 MDS sample, PSO J185.

We query the archival photometry data from the *AllWISE* (Cutri & et al., 2013), SDSS, and *GALEX* (Bianchi et al., 2011) catalogs; in the radio and X-ray bands, where no detections are reported, we instead use their respective upper limits. We summarize the calculated rest-frame ν and νL_ν in Table 5.22. We then calculate the temperature range $kT_0 - 15kT_0$ where the spectral notch

⁵However, see Farris et al. (2015), who do not predict the presence of a notch.

⁶With $R \sim 17$ (Foord et al., 2017), PSO J334 is technically classified as radio-loud.

is expected, where T_0 is the characteristic temperature of the notch: $T_0 = 3.3 \times 10^4 [\dot{m}(\eta/0.1)^{-1} M_8^{-1} (a/100 R_g)^{-3}]^{1/4} \text{K}$ (we have assumed a radiative efficiency $\eta = 0.1$) and the largest deficit is expected at $\sim 4kT_0$ (Roedig et al., 2014). As we show in Figure 5.16, the SED of PSO J185 is consistent with that of a radio quiet quasar and does not show evidence for a spectral deficit. However, due to the low spectral resolution, the presence of a notch cannot be ruled out either.

5.8 Summary and Conclusions

We have conducted a systematic search for periodically varying quasars in the PS1 Medium Deep Survey, following our previous work in L16. Periodic variability has been predicted as a signature of a supermassive black hole binary (SMBHB) system as the mass accretion is modulated by the binary’s orbital motion; in an SMBHB viewed at a high inclination angle, periodic variation can also be produced by relativistic Doppler boosting. SMBHBs at sub-pc separations should be a natural product of galaxy mergers; however, compelling observational evidence for their existence has been elusive. A systematic search for periodic quasars in the time domain is therefore a novel approach to identify SMBHB candidates that are not resolvable via direct imaging.

One challenge to the SMBHB candidates identified in systematic searches (*e.g.* G15; C16; L16) is a robust detection of periodicity, since stochastic, normal quasar variability can easily mimic periodic variation over a small number of cycles. We monitor the variability of our periodic candidates using the Discovery Channel Tele-

scope and the Las Cumbres Observatory network and are able to extend the total baseline of observations to 3-15 cycles. We have also searched for a periodic signal in the presence of red noise, which is modeled by the Damped Random Walk (DRW) process, or a broken power-law power spectrum. Only one candidate is considered statistically significant from this analysis (assuming DRW noise), but six candidates have increased significance when extended data are included (assuming either noise model) and are therefore still consistent with the expectations for a true periodic signal. This sample of SMBHB candidates down-selected from our more rigorous method translates to a rate of < 0.6 per 1000 quasars, or < 0.12 per deg^2 , which is consistent with theoretical predications but in possible tension with the rates inferred by previous searches.

Table 5.18: Re-analyses Using the Maximum Likelihood Method under the BPL Model (MD01-MD04)

| PS1 Designation | $\ln \mathcal{L}_{\text{BPL}}$ (PS1 Only) | $\ln \mathcal{L}_{\text{BPL}+\text{p}}$ (PS1 Only) | P [day] (PS1 Only) | p-value (PS1 Only) | $\ln \mathcal{L}_{\text{BPL}}$ (Ext.) | $\ln \mathcal{L}_{\text{BPL}+\text{p}}$ (Ext.) | P [day] (Ext.) | p-value (Ext.) |
|------------------------------|--|---|------------------------------|-----------------------|--|---|------------------------------|-------------------|
| PSO J35.7068–4.2314 | 122.084 | 123.290 | $440.65^{+272.31}_{-197.69}$ | 0.299 | 146.222 | 149.598 | $438.39^{+253.81}_{-386.18}$ | 0.0341 |
| PSO J35.8704–4.0263 | 135.932 | 139.463 | $933.95^{+37.15}_{-42.84}$ | 0.0292 | 159.068 | 159.456 | $865.56^{+96.79}_{-363.20}$ | 0.678 |
| PSO J52.6172–27.6268 | 92.067 | 94.015 | $920.65^{+42.86}_{-327.13}$ | 0.142 | ... | ... | ... | ... |
| PSO J129.4288+43.8234 | 149.500 | 151.079 | $39.67^{+286.67}_{-23.32}$ | 0.206 | 142.371 | 144.485 | $315.03^{+283.01}_{-276.98}$ | 0.120 |
| PSO J130.9953+43.7685 | 144.857 | 146.891 | $676.61^{+125.09}_{-94.90}$ | 0.130 | 167.262 | 171.668 | $719.63^{+73.29}_{-66.70}$ | 0.0122 |
| PSO J131.1273+44.8582 | 122.882 | 126.346 | $854.51^{+63.68}_{-76.31}$ | 0.0313 | 139.890 | 142.284 | $951.58^{+11.24}_{-28.75}$ | 0.0912 |
| PSO J131.7789+45.0939 | 116.029 | 122.908 | $683.18^{+35.24}_{-564.75}$ | 0.00102 | 144.822 | 147.025 | $791.39^{+161.90}_{-138.09}$ | 0.110 |
| PSO J148.8485+1.8124 | 118.235 | 121.033 | $843.44^{+124.29}_{-115.70}$ | 0.0609 | 136.484 | 137.714 | $884.32^{+82.72}_{-527.27}$ | 0.292 |
| PSO J149.4989+2.7827 | 117.984 | 115.298 | $837.46^{+36.91}_{-33.08}$ | ... | 133.597 | 134.509 | $970.23^{+0}_{-187.79}$ | 0.401 |
| PSO J149.2447+3.1393 | 103.452 | 107.834 | $937.46^{+25.36}_{-54.63}$ | 0.0125 | 100.806 | 102.672 | $911.45^{+53.11}_{-256.88}$ | 0.154 |
| PSO J149.9400+1.5090 | 132.670 | 135.961 | $139.77^{+221.62}_{-58.38}$ | 0.0372 | 150.163 | 150.793 | $410.55^{+260.84}_{-399.15}$ | 0.532 |
| PSO J149.6873+1.7192 | 106.677 | 111.590 | $809.69^{+124.54}_{-225.45}$ | 0.00735 | 138.831 | 145.153 | $882.80^{+73.75}_{-36.24}$ | 0.00179 |
| PSO J150.9191+3.3880 | 91.667 | 96.013 | $750.01^{+215.48}_{-184.51}$ | 0.0129 | 108.393 | 109.759 | $714.21^{+155.27}_{-444.73}$ | 0.255 |

Table 5.19: Re-analyses Using the Maximum Likelihood Method under the BPL Model (MD05-MD10)

| PS1 Designation | $\ln \mathcal{L}_{\text{BPL}}$ (PS1 Only) | $\ln \mathcal{L}_{\text{BPL}+\text{p}}$ (PS1 Only) | P [day] (PS1 Only) | p -value (PS1 Only) | $\ln \mathcal{L}_{\text{BPL}}$ (Ext.) | $\ln \mathcal{L}_{\text{BPL}+\text{p}}$ (Ext.) | P [day] (Ext.) | p -value (Ext.) |
|------------------------------|--|---|------------------------------|--------------------------|--|---|------------------------------|----------------------|
| PSO J160.6037+56.9160 | 163.097 | 165.788 | $940.31^{+27.71}_{-362.28}$ | 0.0678 | 159.657 | 163.796 | $887.59^{+81.60}_{-138.39}$ | 0.0159 |
| PSO J161.2980+57.4038 | 121.914 | 127.821 | $889.98^{+80.16}_{-59.83}$ | 0.00272 | 102.539 | 105.230 | $749.69^{+212.07}_{-247.93}$ | 0.0678 |
| PSO J163.2331+58.8626 | 157.344 | 157.899 | $114.96^{+329.92}_{-110.07}$ | 0.574 | 158.363 | 159.913 | $114.03^{+344.93}_{-65.06}$ | 0.212 |
| PSO J185.8689+46.9752 | 115.700 | 117.084 | $276.42^{+282.49}_{-17.50}$ | 0.250 | 115.590 | 121.326 | $948.27^{+16.31}_{-23.68}$ | 0.00322 |
| PSO J213.9985+52.7527 | 149.063 | 151.434 | $252.65^{+591.97}_{-88.02}$ | 0.0933 | 151.416 | 153.182 | $691.74^{+178.37}_{-261.62}$ | 0.171 |
| PSO J214.9172+53.8166 | 120.828 | 121.999 | $89.51^{+283.66}_{-46.33}$ | 0.310 | 119.487 | 122.671 | $859.68^{+40.56}_{-289.43}$ | 0.0414 |
| PSO J242.5040+55.4391 | 156.506 | 157.818 | $923.49^{+44.85}_{-125.14}$ | 0.269 | 178.187 | 178.543 | $860.67^{+102.24}_{-267.75}$ | 0.700 |
| PSO J242.8039+54.0585 | 141.217 | 145.791 | $11.11^{+289.78}_{-0.21}$ | 0.0103 | 176.463 | 178.068 | $693.01^{+79.97}_{-280.02}$ | 0.200 |
| PSO J243.5676+54.9741 | 152.160 | 152.454 | $957.06^{+7.42}_{-262.57}$ | 0.745 | 184.377 | 186.607 | $127.27^{+288.24}_{-111.75}$ | 0.107 |
| PSO J333.0298+0.9687 | 63.575 | 63.509 | $417.03^{+408.59}_{-131.40}$ | ... | 109.700 | 110.376 | $62.03^{+297.64}_{-52.35}$ | 0.508 |
| PSO J333.9832+1.0242 | 179.692 | 185.789 | $472.80^{+314.55}_{-15.44}$ | 0.00224 | 246.109 | 249.901 | $443.50^{+178.16}_{-401.83}$ | 0.0225 |
| PSO J334.2028+1.4075 | 165.162 | 166.541 | $573.64^{+106.54}_{-153.45}$ | 0.251 | 215.223 | 216.272 | $131.73^{+132.76}_{-127.23}$ | 0.350 |
| PSO J351.5679-1.6795 | 124.080 | 134.519 | $832.49^{+81.66}_{-28.33}$ | 2.92×10^{-5} | 113.713 | 120.584 | $827.56^{+70.45}_{-19.54}$ | 0.00103 |

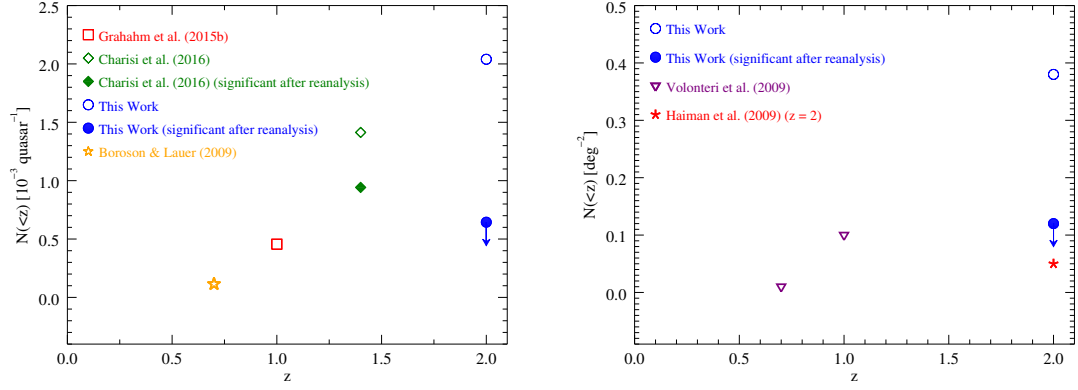


Figure 5.12: Left panel: the cumulative number of SMBHB candidates per 1,000 quasars from this work (blue circles), C16 (green diamonds), and G15 (red squares). Both this work and C16 re-analyzed their samples by adding extended data; the rates calculated from the candidates that are ruled significant after re-analysis are indicated with filled symbols. The cumulative rate inferred from C16 is inconsistent with the rate measured in this work. We also compare the rates from this work, C16, and G15 with the spectroscopic search by BL09 (orange star). Right panel: We compare the cumulative number of SMBHB candidates per deg^2 of sky area from this work with the predicted rates by VMD09 (purple triangles) and HKM09 (asterisk). The cumulative rate measured from this work is marginally consistent with the prediction by VMD09 or HKM09 (see the text for details).

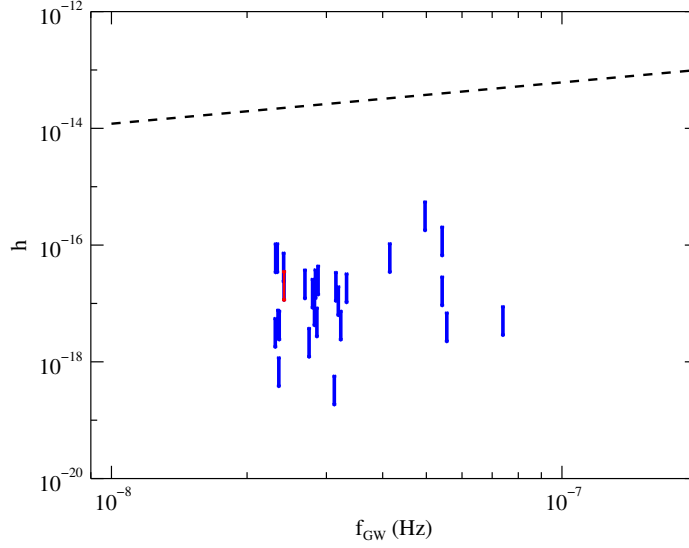


Figure 5.13: We use the current upper limit on CW ([Perera et al., 2018](#)) as a proxy for detection sensitivity (dashed line). The gravitational wave strain amplitudes of the candidates (bars) are lower by a few orders of magnitude than the upper limit. The best candidate (PSO J185) is indicated as a red bar. All chirp masses are calculated for the range $q = 0.1 - 1.0$.

Table 5.20: Comparing PS1 MDS and LSST Capabilities

| | PS1 MDS | LSST |
|--|---------|--------|
| Single visit 5σ magnitude depth in g band [mag] | 22.5 | 25.0 |
| Expected photometric error at $g = 17$ mag [mag] | 0.02 | 0.005 |
| Sky coverage [deg ²] | 50 | 20,000 |

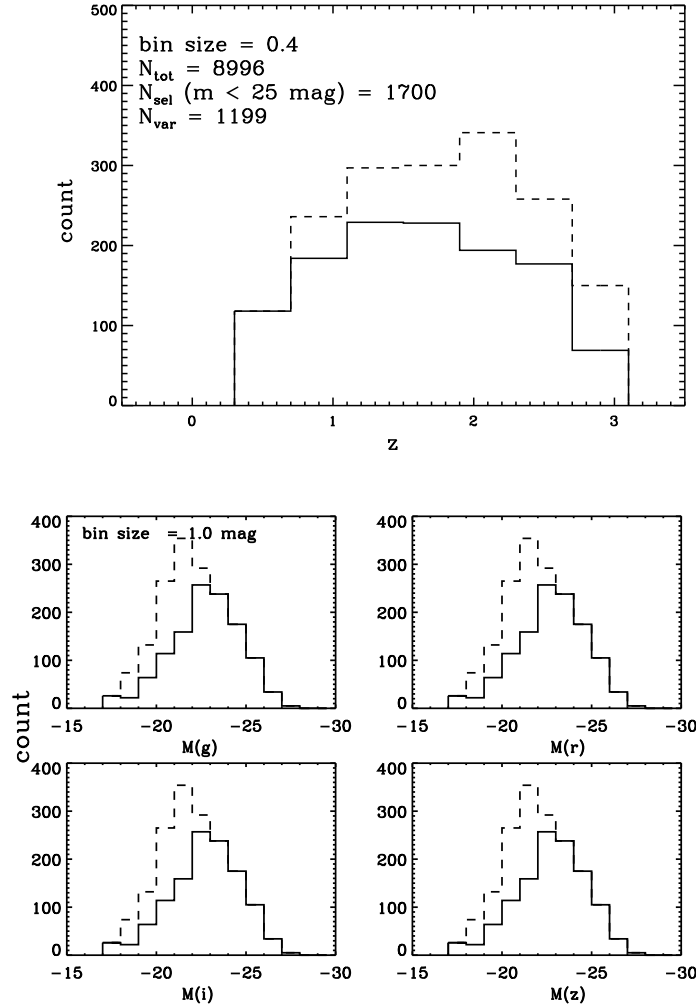


Figure 5.14: From an initial sample of 8,996 quasars drawn from the quasar luminosity function, 1,700 can be detected by LSST (dashed histograms). Assuming they follow the variability amplitude-absolute magnitude relation in [Heinis et al. \(2016b\)](#), 1,199 can be detected as variable quasars (solid histograms). They span a range of redshifts ($0.3 < z < 3.1$) and absolute magnitudes ($-17 < M < -27$).

Table 5.21: Overview of test cases used in this study.

| | z_{\min} | z_{\max} | $\log M_{\text{ch},\min}$ | $\log M_{\text{ch},\max}$ | $\log f_{\text{GW},\min}$ | $\log f_{\text{GW},\max}$ | number of realizations |
|------------|------------|------------|---------------------------|---------------------------|---------------------------|---------------------------|------------------------|
| LSST | 1.6 | 1.6 | 6.1 | 9.2 | -7.7 | -5.9 | ... |
| CRTS | 1.0 | 1.0 | 7.1 | 9.8 | -7.7 | -5.7 | ... |
| PS1 MDS | 1.0 | 1.0 | 7.3 | 9.5 | -7.3 | -5.1 | ... |
| 20-yr IPTA | 0.003 | 1.0 | 8.5 | 10.5 | -8.7 | -8.0 | 383 |
| 6-yr SKA1 | 0.003 | 1.0 | 8.5 | 10.0 | -8.2 | -7.5 | 395 |
| 6-yr SKA2 | 0.003 | 1.0 | 8.0 | 10.0 | -8.2 | -7.5 | 322 |

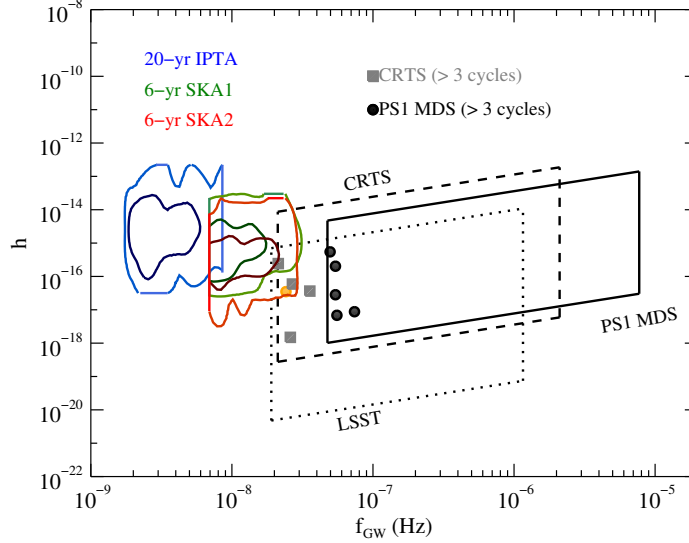


Figure 5.15: We calculate the GW strain amplitudes of SMBHBs that are most likely to be detected as individual sources by the 20-yr IPTA (blue contours), 6-yr SKA1 (green contours), and 6-yr SKA2 (red contours), adopting their z , M_{ch} , and f_{GW} values from [Rosado et al. \(2015\)](#). The contours have been smoothed, and the darker (lighter) shade of contour color represents 68% (99.7%) of the realizations. The abrupt cut-offs reflect the ranges of parameters applied (Table 5.21). We also estimate the range of h and f_{GW} that PS1 MDS, CRTS, and LSST are sensitive to (solid, dashed, and dotted box, respectively). Though the SMBHB candidates from PS1 MDS or CRTS ($N_{\text{cycle}} > 3$ only) are unlikely to be detected as individual CW sources by IPTA (grey boxes and black circles, respectively), those from LSST could be detected by the SKA. The best candidate from this work, PSO J185, is also included in figure (orange circle). For simplicity, we have adopted $q = 1$ for all calculations.

Table 5.22: The SED of PSO J185

| Catalog | Filter/Band | ν (Hz) | νL_ν (erg s ⁻¹) |
|-------------------|-------------|-----------------------|------------------------------------|
| FIRST | 1.4 GHz | 3.75×10^9 | (2.50×10^{41}) |
| <i>AllWISE</i> | W1 | 2.40×10^{14} | 9.38×10^{44} |
| <i>AllWISE</i> | W2 | 1.75×10^{14} | 7.96×10^{44} |
| <i>AllWISE</i> | W3 | 6.93×10^{13} | (1.68×10^{45}) |
| <i>AllWISE</i> | W4 | 3.64×10^{13} | (4.29×10^{45}) |
| SDSS | u | 2.27×10^{15} | 3.07×10^{45} |
| SDSS | g | 1.69×10^{15} | 2.58×10^{45} |
| SDSS | r | 1.29×10^{15} | 1.80×10^{45} |
| SDSS | i | 1.05×10^{15} | 2.05×10^{45} |
| SDSS | z | 8.81×10^{14} | 1.67×10^{45} |
| <i>GALEX</i> | NUV | 3.55×10^{15} | 2.02×10^{45} |
| <i>XMM-Newton</i> | 1.5 keV | 9.72×10^{17} | (4.89×10^{46}) |

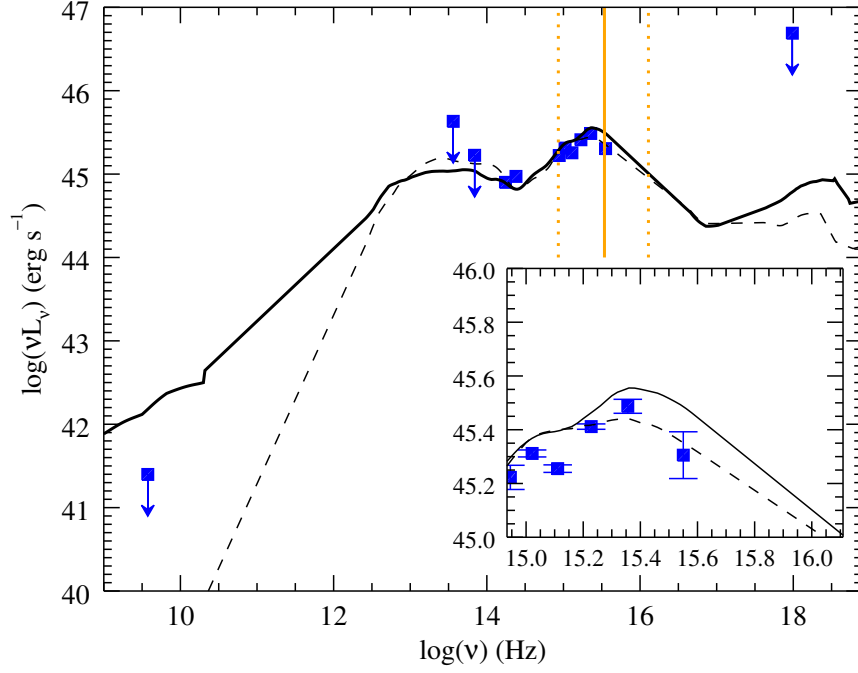


Figure 5.16: We construct the SED of PSO J185 using multi-band archival data (or upper limits; blue squares). We then compare with the mean SEDs of radio loud and radio quiet quasars (solid and dashed curves, respectively) from [Elvis et al. \(1994\)](#). The mean SED has been normalized to PSO J185 at $\lambda_{\text{rest}} = 2000\text{\AA}$. PSO J185 is consistent with the SED of a radio quiet quasar, while showing no evidence for a spectral notch (dashed orange lines mark the range $kT_0 - 15kT_0$, and the solid orange line marks $4kT_0$). The inset shows the SED of PSO J185 (and the mean quasar SEDs) in the frequency range $kT_0 - 15kT_0$.

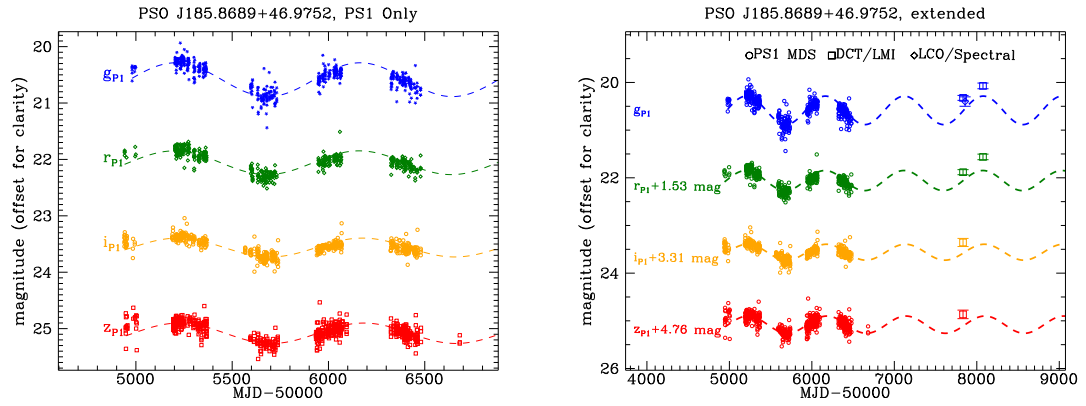


Figure 5.17: The PS1-only light curve of the best candidate from PS1 MDS, PSO J185.8689+46.9752 (hereafter PSO J185) (left), and its extended light curve, which consists of new data from DCT/LMI (squares) and LCO/Spectral (diamond). Sinusoids of periods determined from the periodogram are imposed to guide the eye (dashed lines).

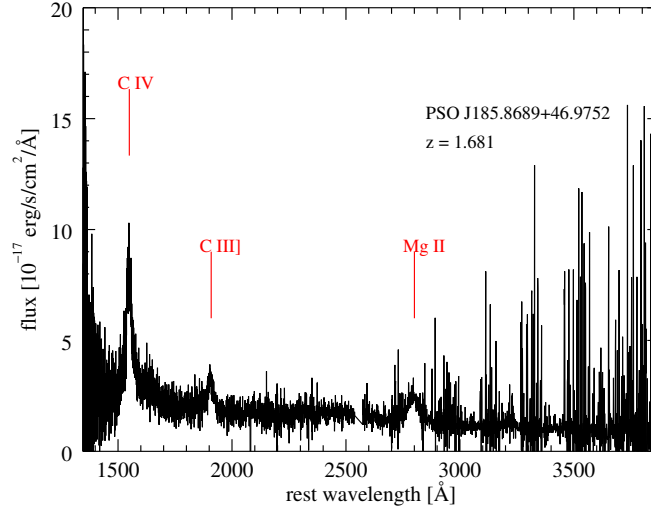


Figure 5.18: The SDSS spectrum of PSO J185 (also shown in Figure 5.27). Its broad MgII line (a blowup is shown in Figure 5.27, last but one panel) shows no apparent spectral features that deviate from those of a normal quasar.

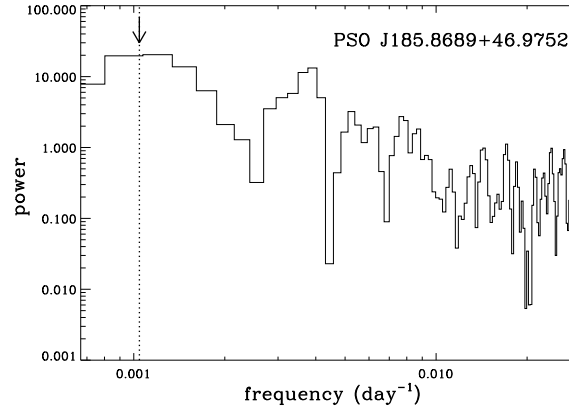


Figure 5.19: The Lomb-Scargle periodogram of PSO J185 (PS1-only). The dashed line marks the peak at 958 days, which is consistent with the best-fit period from the maximum likelihood analysis of the extended light curve (arrow). The best-fit period of ≈ 280 days from the PS1-only light curve is also seen as a possible peak in the periodogram (at $f \sim 0.003 \text{ day}^{-1}$).

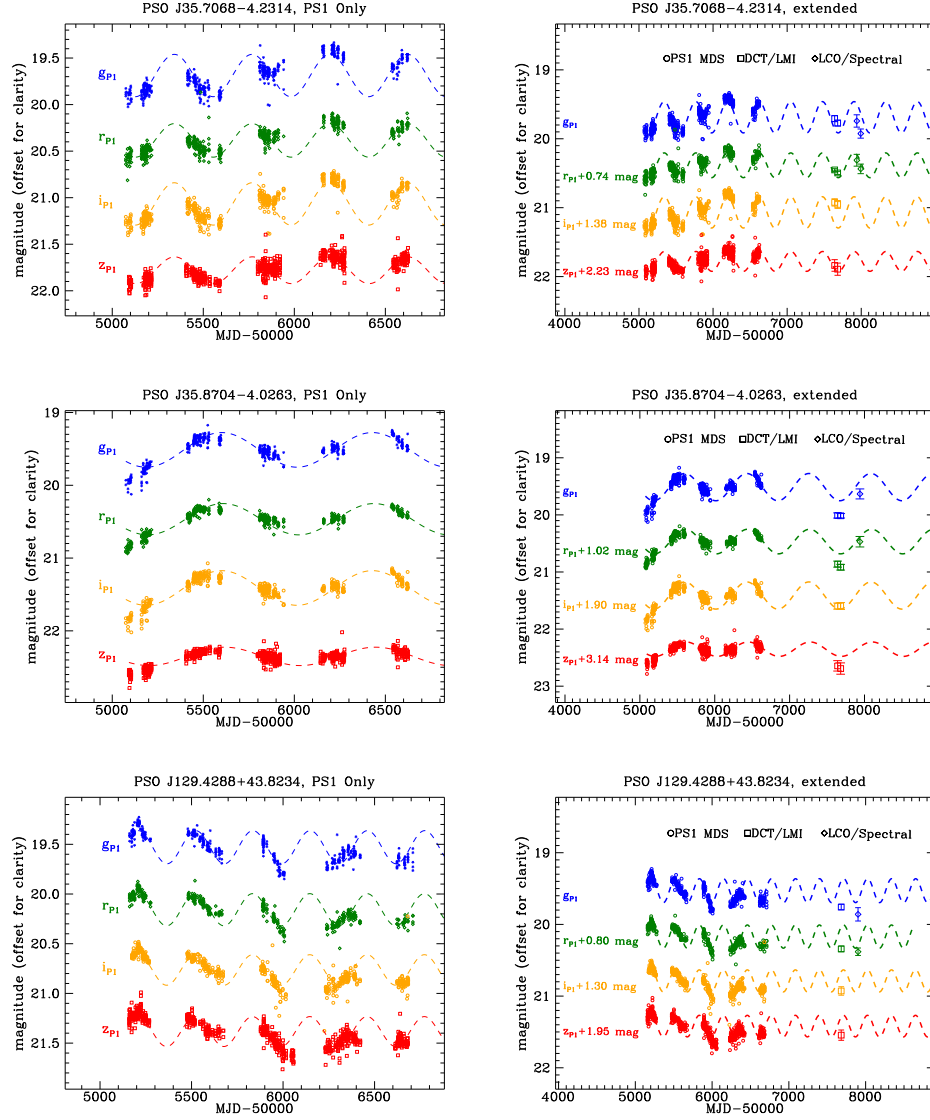


Figure 5.20: The PS1 and extended light curves of the remaining candidates from PS1 MDS. Sinusoids of periods determined from the periodogram are imposed to guide the eye (dashed lines). Different sources of archival or new monitoring data are represented by different symbols: *GALEX* – dots, SDSS/S82 – stars, PS1/MDS – circles, DCT/LMI – squares, LCO/Spectral – diamonds.

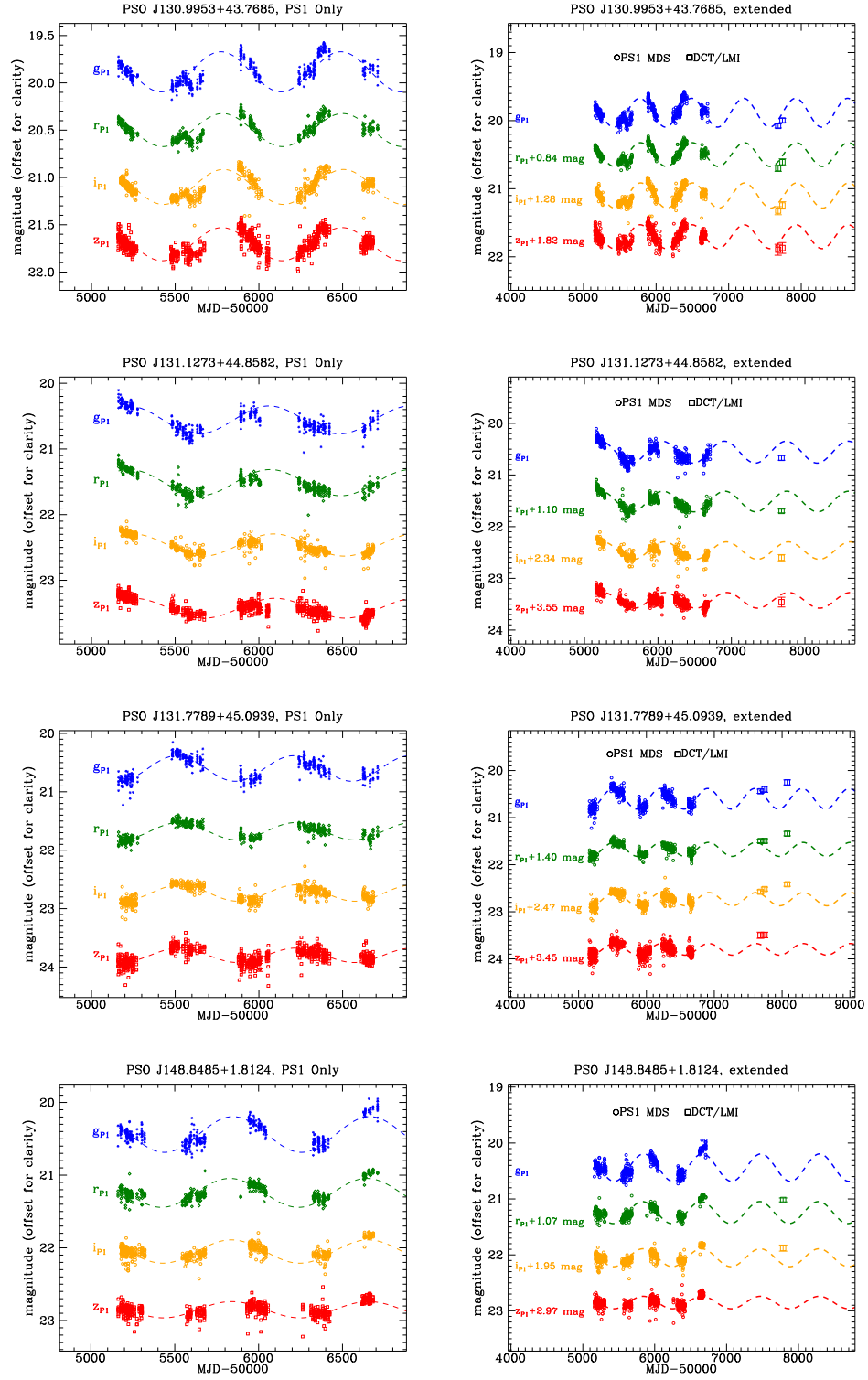


Figure 5.21: Figure 5.20 continued.

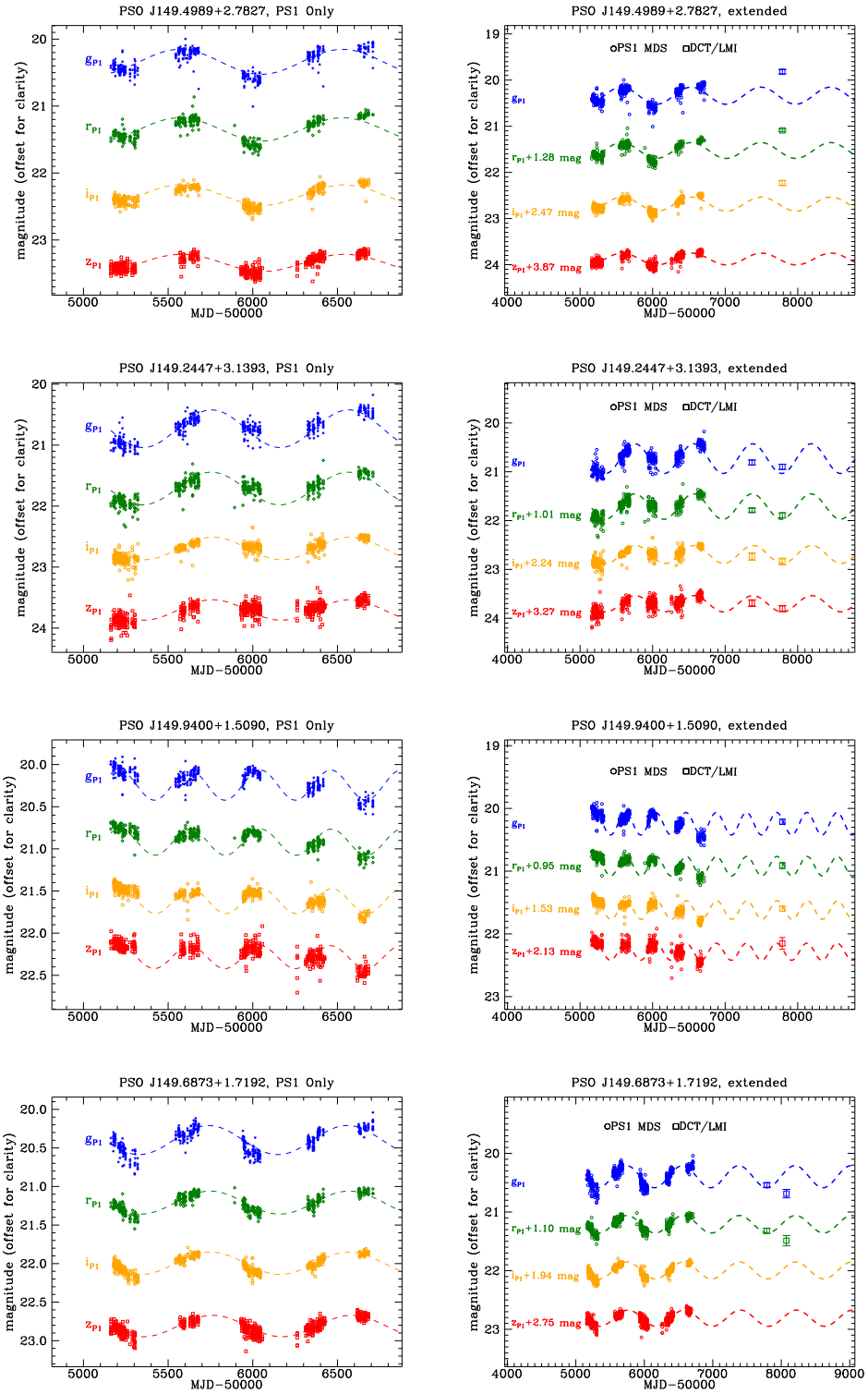


Figure 5.22: Figure 5.21 continued.

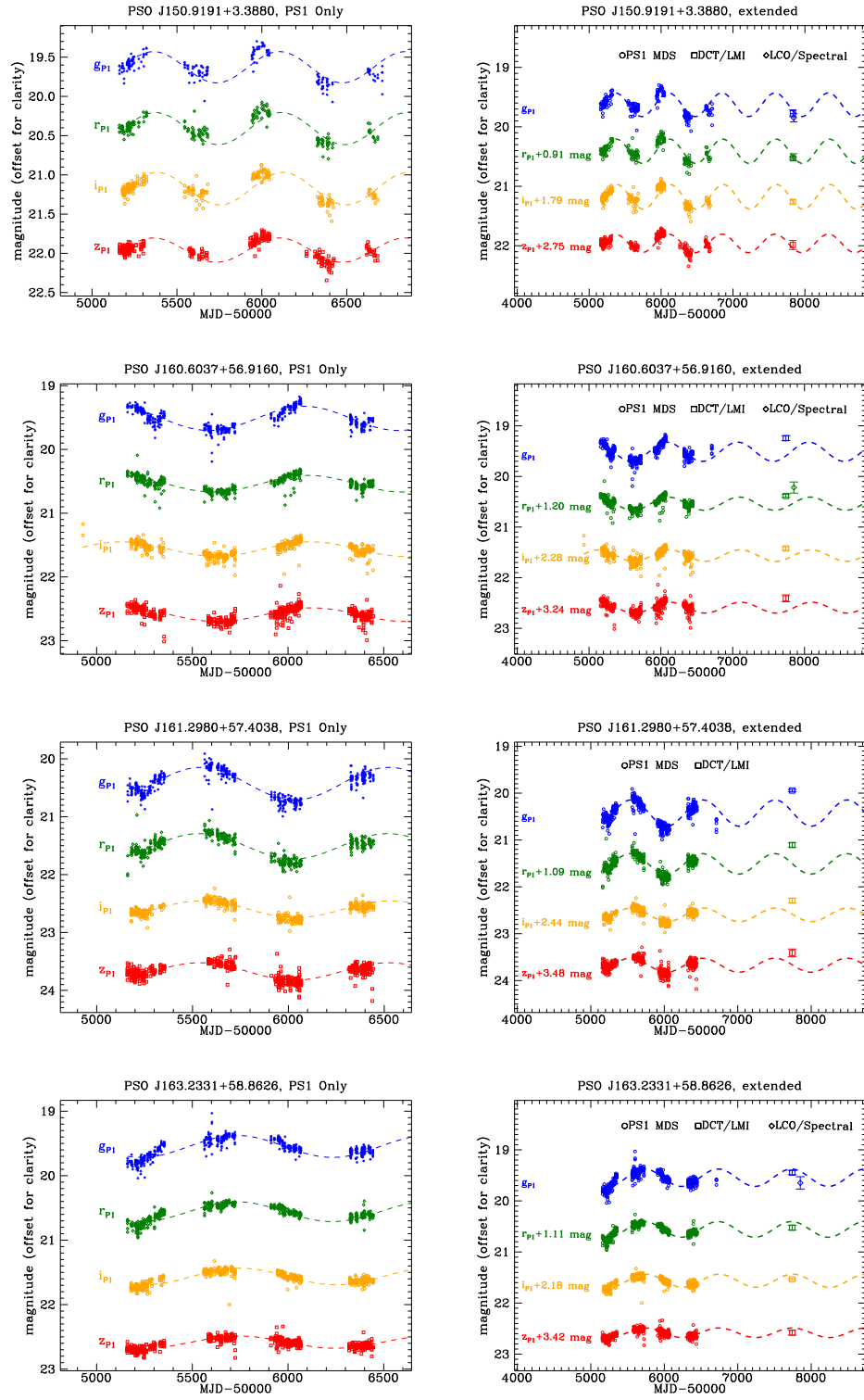


Figure 5.23: Figure 5.22 continued.

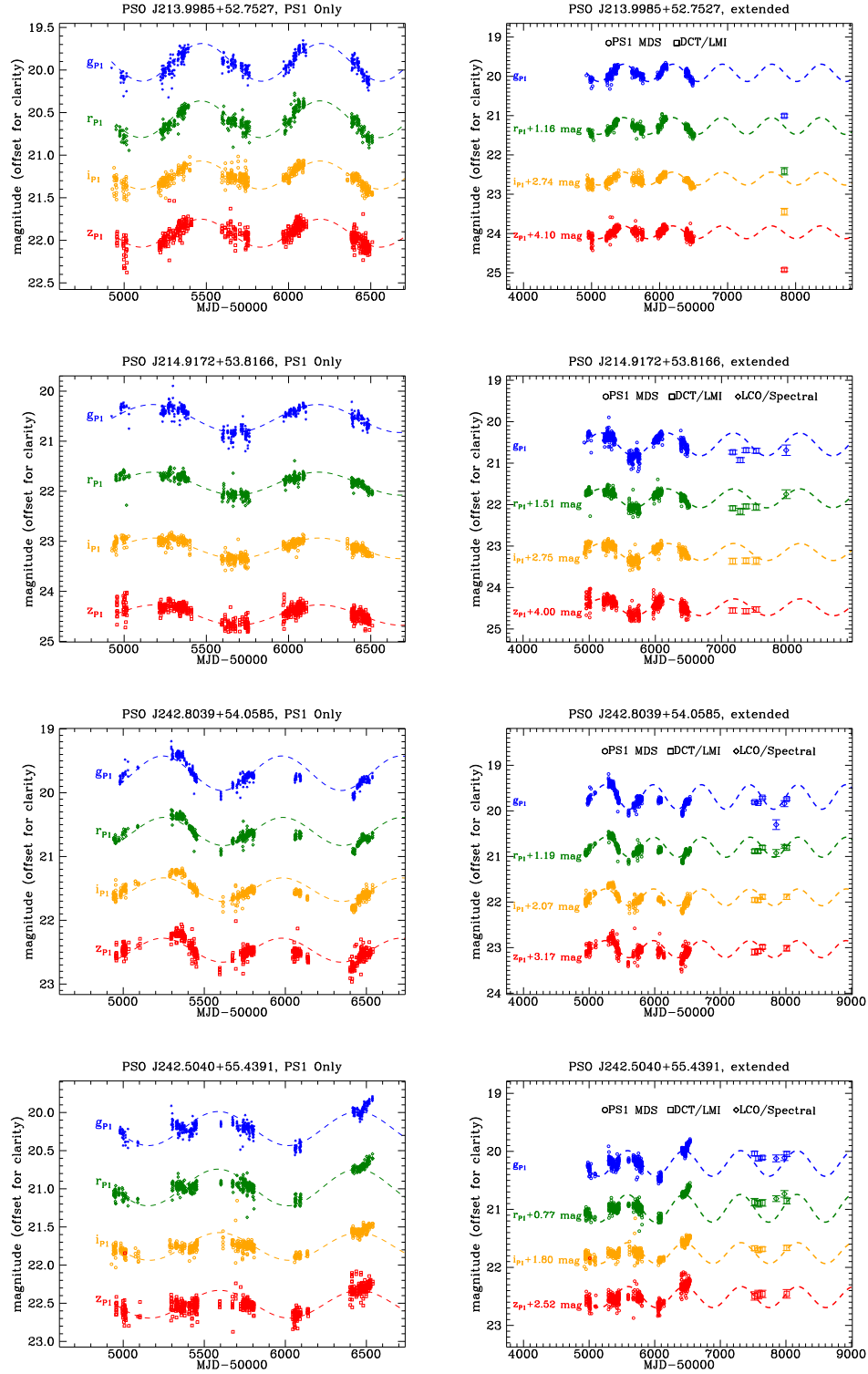


Figure 5.24: Figure 5.23 continued.

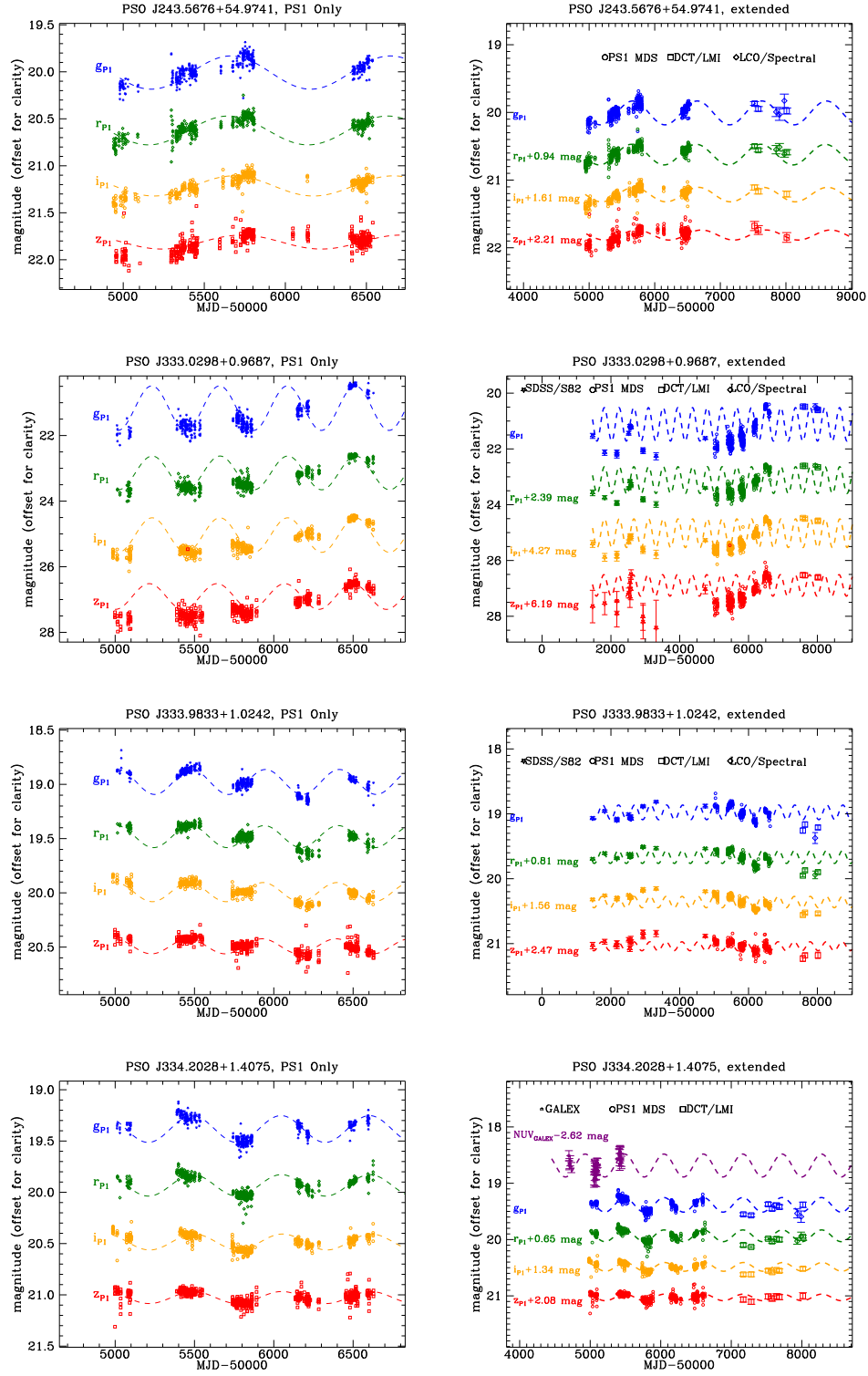


Figure 5.25: Figure 5.24 continued.

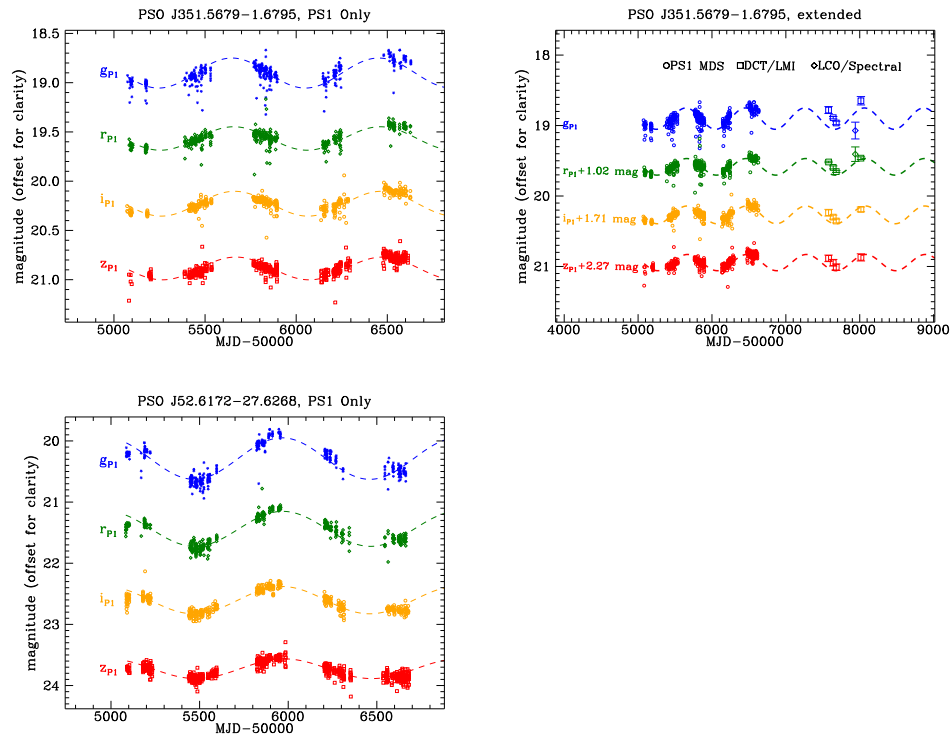


Figure 5.26: Figure 5.25 continued.

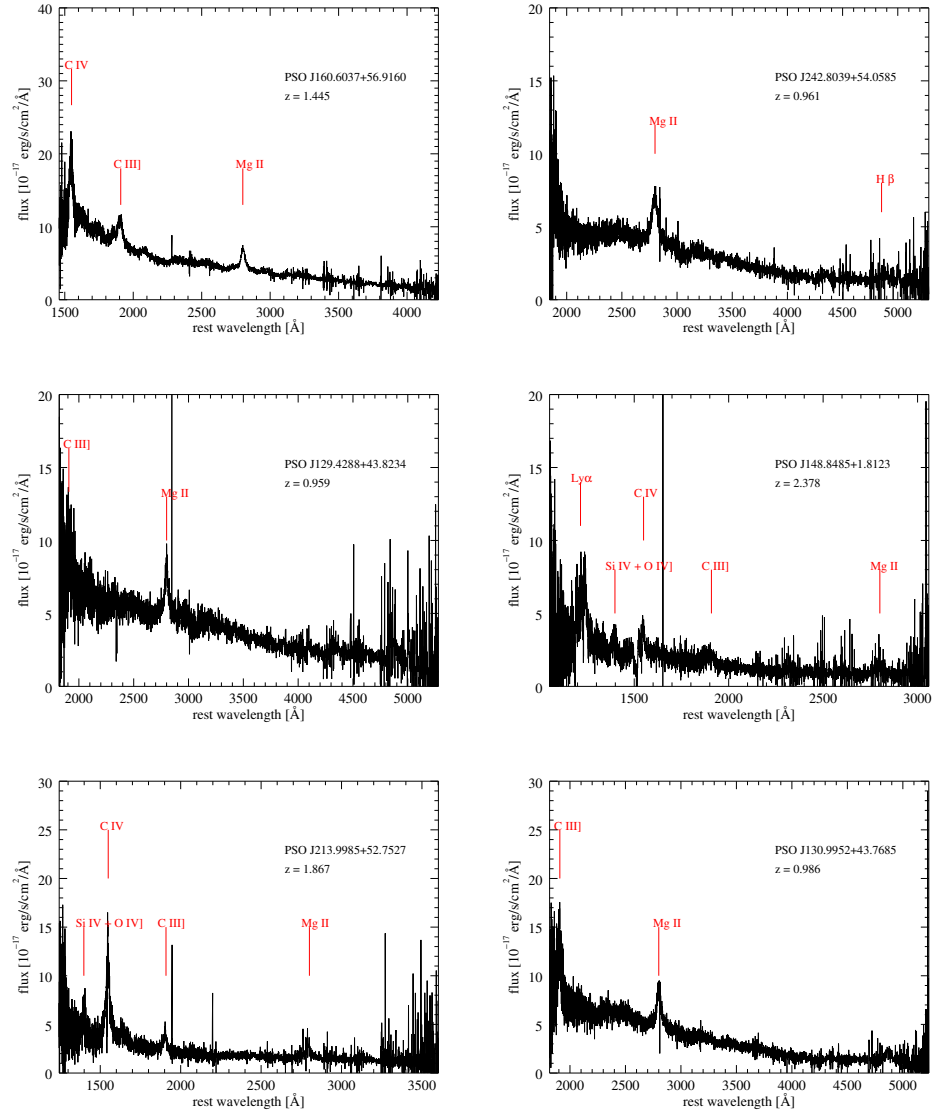


Figure 5.27: We retrieved archival SDSS spectra from the SDSS Science Archive and obtained spectroscopic observations with Gemini/GMOS or DCT/DeVeny. Prominent emission lines, including the black hole mass estimators C IV and Mg II, are indicated with red tick marks. The last two panels show example procedures of our spectral fitting of the continuum and the broad MgII or CIV line.

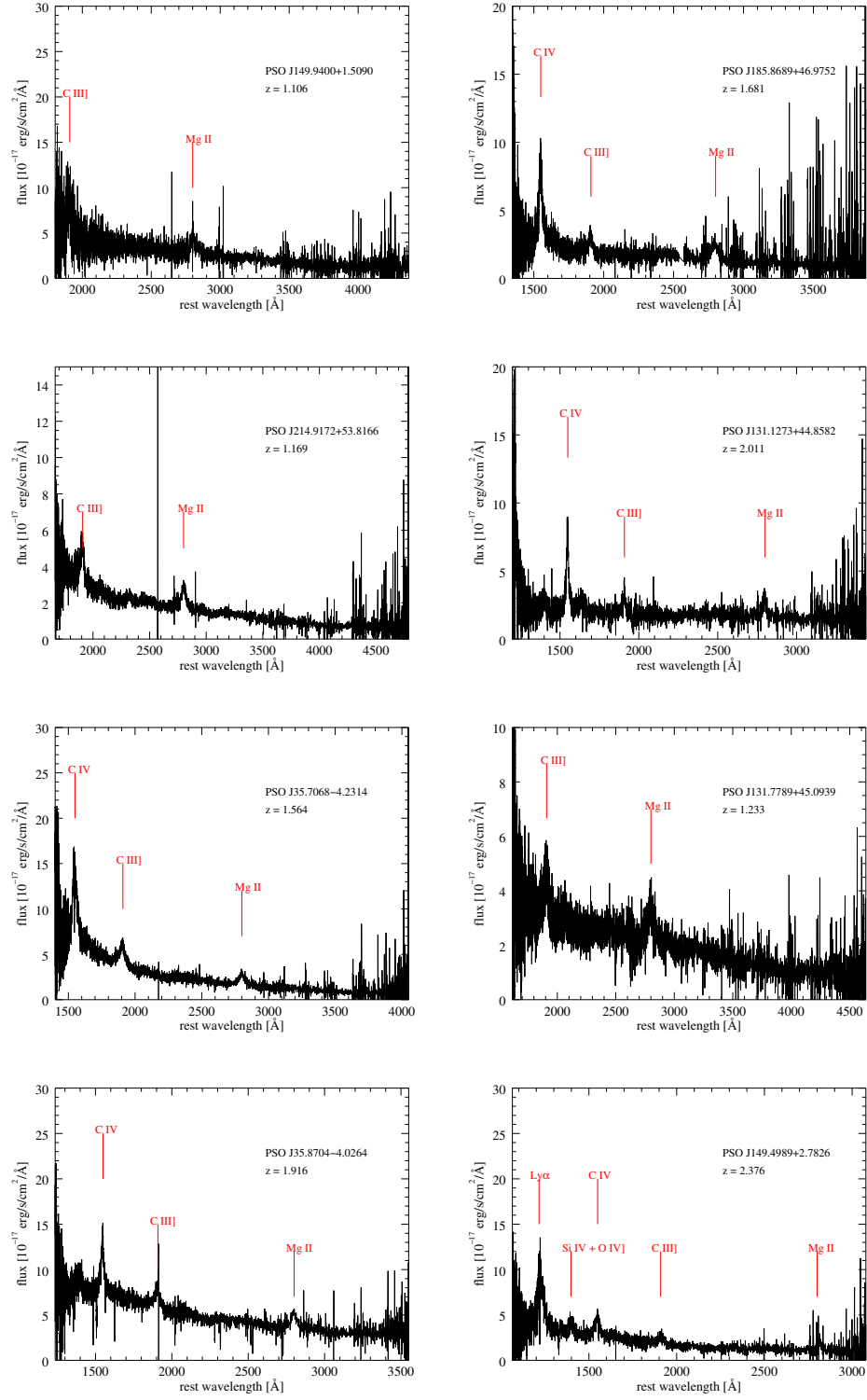


Figure 5.28: Figure 5.27 continued.

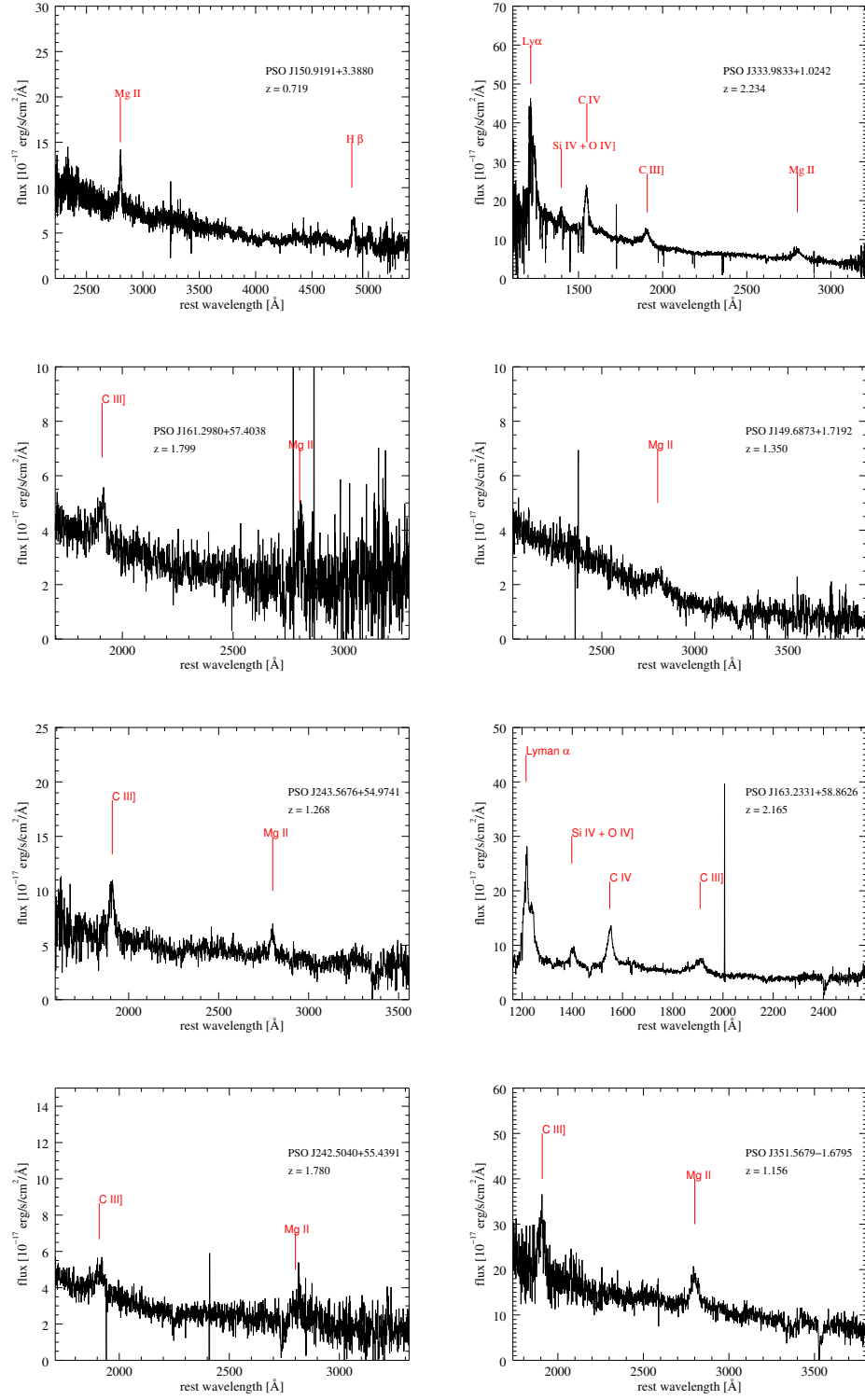


Figure 5.29: Figure 5.28 continued.

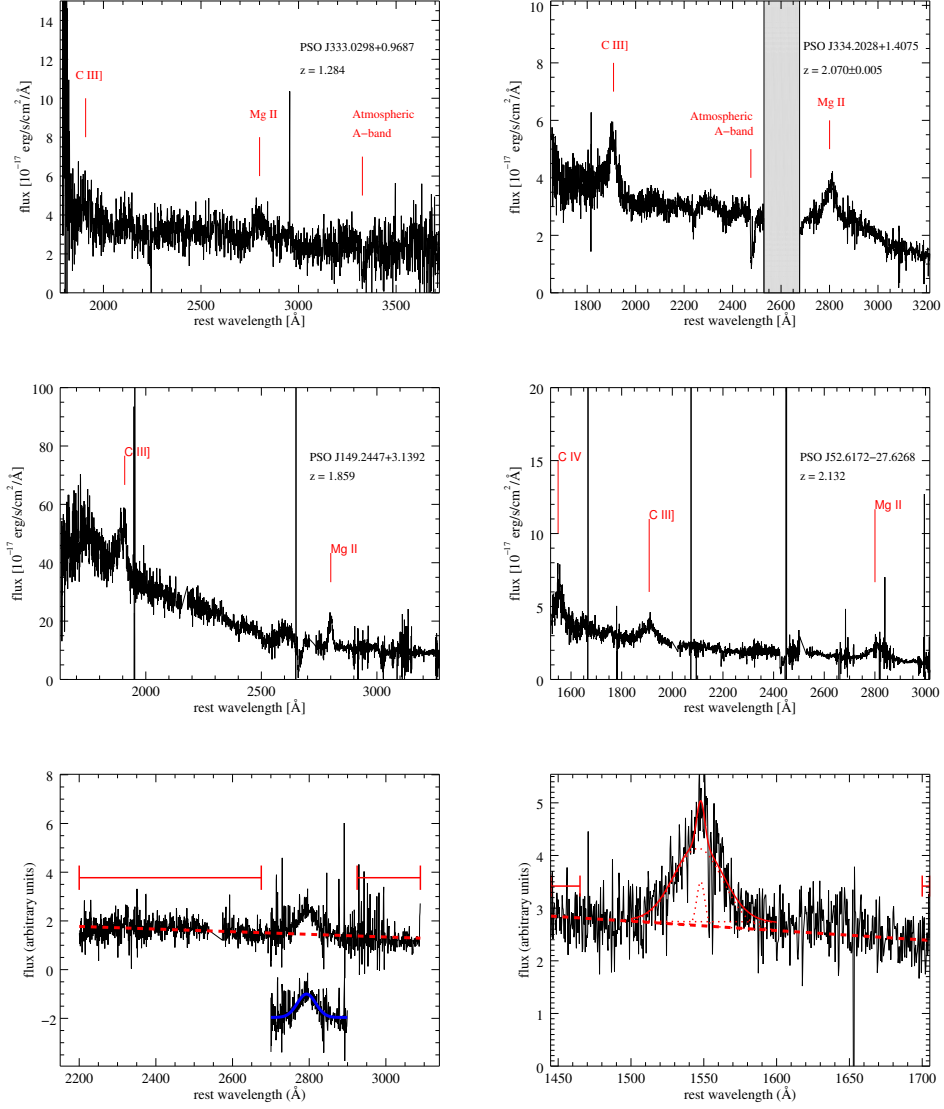


Figure 5.30: Figure 5.29 continued.

Chapter 6: Conclusions and Future Work

In this thesis, I have presented a systematic search for periodically varying quasars, which are theoretically-predicted manifestations of SMBHBs at sub-pc separations. Using a custom-developed pipeline, I have mined the PS1 MDS dataset and selected 26 candidates from ten MD fields. These candidates have at least 1.5 cycles of variation over the PS1 baseline, and their observed periods are between ~ 400 days and ~ 1000 days. Their PS1 magnitudes are between $g_{P1} = 19$ and 21, at least 1 mag deeper than previous systematic searches. By following up these sources spectroscopically, I was able to measure their black hole masses and redshifts. The majority of the candidates have masses between $10^8 M_{\odot}$ and $10^{10} M_{\odot}$, similar to previous work; however, our search is more sensitive at higher redshifts, and the candidates have an almost flat distribution between $1 < z < 2$. I then followed up these candidates with extended-baseline imaging, in order to put their periodicity to the test and break false positive signals due to the stochastic variability of regular quasars. As evidence for a true periodic signal should strengthen over a longer baseline, we are able to apply more rigorous down-selection criteria to the sample of 26 candidates, as well as a periodic candidate reported in the literature, the SMBHB candidate PG 1302–102. PG 1302–102 fails to demonstrate persistent

periodicity by our analysis, and at most six candidates from our PS1 MDS sample are statistically significant, assuming that normal stochastic quasar variability is modeled by the Damped Random Walk (DRW) process or a broken-power law (BPL) PSD. We show that the down-selected sample infers an accumulative SMBHB detection rate of < 0.6 per 1000 quasars, or < 0.12 per deg^2 out to $z = 2$. These upper limits are consistent with theoretical predictions, but the much-higher rates inferred from previous work (Charisi et al., 2016; Graham et al., 2015b) are incompatible with our upper limits.

Among the many questions that this thesis attempts to answer are the expectations for a true periodic signal (Chapter 4), the extended-baseline monitoring of periodic candidates (Chapter 3 Section 3.4; Chapter 5 Section 5.5), and the multi-wavelength (in particular, SED) properties of SMBHB candidates (Chapter 5 Section 5.7.4). However, a few questions remain and deserve further investigation:

1. What would be a convincing detection of periodicity?
2. Can we search for evidence for periodicity in the X-rays?
3. Can we find robust periodic candidates with extended-baseline imaging?
4. Can we search for complementary evidence for an SMBHB?

6.1 What Would be a Convincing Detection of Periodicity?

In Chapter 4, I have reanalyzed the putative periodicity of the SMBHB candidate PG 1302–102 and shown that it is inconsistent with the expectation that

the significance of a true periodic signal should increase over a longer baseline, even though the new data have larger photometric uncertainties. While I have performed the test for a simulated light curve generated from the DRW model plus a periodic signal (“DRW+periodic”), it can be further improved and made more convincing in the following ways:

- Generate a number of realizations of the DRW process, add periodic signals of various amplitudes and periods, and repeat the analysis; how does their significance increase with the length of the simulated data?
- Generate a number of “DRW-only” realizations using a Monte Carlo method, and repeat the analysis; since a large fluctuation in the power spectrum can mimic a periodic signal, does their significance decrease rapidly with data length?
- Generate a number of realizations of BPL power spectra of various slopes; compared with the DRW+periodic light curves, how does the signal degrade with a different choice of the power-law slope?

In addition to applying the technique described in Chapter 4 to simulated data, one can also use QPOs (a quasi-periodic oscillation is indicated by variability power concentrated in a narrow range of frequencies, superimposed on a broad continuum of red noise) reported in the literature as test cases. One of the highest-significance X-ray QPO in an AGN is detected in the Seyfert galaxy RE J1034+396 (Gierliński et al., 2008), which shows 16 cycles of periodicity with a high quality

factor ($Q = f/\Delta f$, which indicates the coherence of the signal); recently, a candidate optical QPO has been reported in a Seyfert galaxy in the *Kepler* field (Smith et al., 2018b).

So far, the significance of an individual candidate is evaluated by assuming a red noise model (*i.e.* DRW or BPL). Due to our poor knowledge of the red noise continuum of a given candidate, in our analysis in Chapter 5 Section 5.6, a candidate is considered significant only if it passes the test under both assumed models. Thanks to the recent progress made on the analysis of high-quality *Kepler* AGN light curves (Aranzana et al., 2018; Smith et al., 2018a), we now have a better knowledge of the distribution of the (high-frequency) power-law slopes for a sample of AGNs. Equipped with this knowledge, one can calibrate the false alarm rate by simulating a population of variable AGNs or quasars that follow this power-law slope distribution several times over; this statistical approach can then be applied to a large sample of periodic candidates in order to determine their significance as an ensemble (Section 6.2).

6.2 Can We Find Robust Periodic Candidates with Extended-baseline Imaging?

I have demonstrated that extended-baseline monitoring is crucially important in breaking the false positive signal due to stochastic variability and have shown through simulated data that a true periodic signal can be identified with more confidence on a longer baseline. Most of the candidates from the Graham et al.

(2015b) sample have extended data from LINEAR, but an extended-baseline analysis has not been performed on those candidates (with the exception of PG 1302–102). Charisi et al. (2016) have included data from CRTS and/or iPTF in their reanalysis of PTF periodic candidates; however, as I have discussed in Chapter 4 Section 4.4, most of their candidates show a decrease in significance when extended data are included, which may indicate that the detected periodicity does not persist. Despite being shallower than PS1 MDS, the CRTS and PTF surveys are all-sky surveys and provide a much larger sample of periodic candidates (~ 200). We should perform a reanalysis of the periodic candidates from Graham et al. (2015b) and Charisi et al. (2016) and treat them with the same rigorous method as described in Chapter 4. Combined with the statistical method proposed in Section 6.1, the two samples can potentially yield robust periodic candidates for follow-up studies (*e.g.* Section 6.4).

Further, one can further extend the observational baseline of those candidates with new data produced by the Zwicky Transient Facility (ZTF). The new survey builds on the success of PTF and iPTF and is the third operating phase of the Palomar family of telescopes. It will operate for three years (2018-2020) and survey the northern sky with a three-day cadence. While the length of the ZTF survey is comparatively short for the purpose of identifying robust periodic sources that vary for many cycles, its magnitude depth is comparable to that of CRTS or PTF ($R \sim 20.4$) and is naturally suited to follow up those candidates on an even longer baseline.

6.3 Can We Search for Evidence for Periodicity in the X-rays?

So far, systematic searches for periodic quasars have only been performed in the optical time domain, thanks to the abundance, length, and cadence of light curves produced by large optical time domain surveys. The recently-published catalog of sources from the all-sky hard X-ray survey with the *Swift* Burst Alert Telescope (BAT) can help change this landscape.

The 105-month catalog (Oh et al., 2018) contains 1632 hard X-ray sources at 14–195 keV from *Swift* BAT, about 900 of which are AGNs (not including blazars). The catalog includes monthly-sampled light curves extracted from monthly mosaic images of the sources, and it is worthwhile to apply the technique developed for this thesis to search for periodic sources in the BAT catalog.

X-ray periodicity has been recently reported in an SMBHB candidate, MCG+11-11-032, by Severgnini et al. (2018). The source was initially proposed as a dual AGN identified through its double-peaked [OIII] emission lines in the SDSS spectrum (Wang et al., 2009), and follow-up observations have found two components separated by 0.77 arcsec, or 0.55 kpc ($z = 0.036$) (Comerford et al., 2012). Severgnini et al. (2018) further analyzed the BAT light curve of the source and found a tentative period of 25 months over a 123-month baseline, and the hardness ratio of the source suggests that the flux variation is intrinsic and not caused by variable absorption. Its X-ray Telescope (XRT) spectrum is best-fitted by an absorbed power law plus a reflection component and two narrow emission lines at 6.16 keV and 6.56 keV, respectively (the rest-frame energy of the Fe K α line is at 6.4 keV), which they

propose are produced at the inner edge of the circumbinary disk or by gas bound to the individual black holes. Interestingly, under the SMBHB hypothesis, the orbital velocity inferred from the ΔE of the two emission lines ($\sim 0.06c$) is consistent with that inferred from the BAT light curve (Severgnini et al., 2018).

Other X-ray variability signatures of an SMBHB have also been explored in recent simulations. Tang et al. (2018) followed an equal-mass $10^6 M_\odot$ SMBHB from $60 r_g$ to merger (which corresponds to ~ 100 orbits, or weeks prior to merger) and find clear periodicity at twice the binary orbital frequency throughout the process in the soft X-ray band (at 2 keV), which is produced by gas flung outwards by the black holes and periodically hitting the inner edge of the circumbinary disk. The hard X-ray band at 10 keV, on the other hand, is dominated by the minidisk emission. While variability in the hard X-ray band is more stochastic at the beginning of the process, clear periodicity develops at the late stage of the inspiral and pulsates at the same frequency as the soft X-ray band. This signature could be used to identify the EM counterpart of a source for the Laser Interferometer Space Antenna (LISA), the space-based GW detector which is sensitive to 0.1 mHz - 1 Hz frequencies.

The 105-month BAT catalog also provides spectra constructed from eight energy bands: 14 – 20 keV, 20 – 24 keV, 24 – 35 keV, 35 – 50 keV, 50 – 75 keV, 75 – 100 keV, 100 – 150 keV, and 150 – 195 keV, in which one can look for excess X-ray emission in a BAT periodic candidate and follow up with observations with a higher energy resolution. Enhanced X-ray emission should be a unique signature of shock-heated minidisks, which would provide complementary evidence for an SMBHB (Section 6.4).

6.4 Can We Search for Complementary Evidence for an SMBHB?

As several previous work have predicted (*e.g.* [Farris et al. 2015](#); [Roedig et al. 2014](#)), the spectrum of an SMBHB system has contributions from three distinct components — the minidisks, the accretion streams, and the circumbinary disk — and should distinguish from a regular accreting SMBH. In the analytical work by [Roedig et al. \(2014\)](#), the streams shock-heat the outer edge of the minidisks and produce bright hard X-ray emission at ~ 100 keV due to Compton cooling. They also argue that a spectral “notch” should be another distinctive signature of a binary, due to missing radiation from the cavity in the circumbinary disk; the temperature of the notch lies between the lowest temperature in the minidisks and the highest temperature in the circumbinary disk and depends on parameters including black hole mass, binary separation, accretion rate, and radiative efficiency. The 2D hydrodynamical simulation by [Farris et al. \(2015\)](#) finds similar enhancement in the X-rays, but they expect that the notch is partially filled by emission from the streams and unlikely to be noticeable. The recent 3D MHD simulation by [d’Ascoli et al. \(2018\)](#) has also produced a spectrum of an accreting SMBHB from UV to the X-rays, where the hard X-ray component has the most contribution from the minidisks. I can search for this enhanced feature in the *NuSTAR* hard X-ray spectrum of an SMBHB candidate down-selected from the PS1 MDS sample, or look for hints of spectral hardening in the soft X-rays, which may be more observationally feasible. These features are complementary to the variability signatures of an SMBHB and would be strong supporting evidence for a binary.

Bibliography

- Alam, S., Albareti, F. D., Allende Prieto, C., et al. 2015, *ApJS*, 219, 12
- Andrae, R., Kim, D.-W., & Bailer-Jones, C. A. L. 2013, *AAP*, 554, A137
- Aranzana, E., K rding, E., Uttley, P., Scaringi, S., & Bloemen, S. 2018, *MNRAS*, 476, 2501
- Arzoumanian, Z., Brazier, A., Burke-Spolaor, S., et al. 2014, *ApJ*, 794, 141
- . 2016, *ApJ*, 821, 13
- Arzoumanian, Z., Baker, P. T., Brazier, A., et al. 2018, *ApJ*, 859, 47
- Babak, S., Petiteau, A., Sesana, A., et al. 2016, *MNRAS*, 455, 1665
- Bansal, K., Taylor, G. B., Peck, A. B., Zavala, R. T., & Romani, R. W. 2017, *ApJ*, 843, 14
- Barrows, R. S., Lacy, C. H. S., Kennefick, D., Kennefick, J., & Seigar, M. S. 2011, *New Astronomy*, 16, 122
- Barth, A. J., & Stern, D. 2018, *ArXiv e-prints*, arXiv:1803.00691
- Bauer, A., Baltay, C., Coppi, P., et al. 2009, *ApJ*, 696, 1241
- Becker, R. H., White, R. L., Gregg, M. D., et al. 2001, *ApJS*, 135, 227
- Begelman, M. C., Blandford, R. D., & Rees, M. J. 1980, *Nature*, 287, 307
- Bertin, E. 2006, in *Astronomical Society of the Pacific Conference Series*, Vol. 351, *Astronomical Data Analysis Software and Systems XV*, ed. C. Gabriel, C. Arviset, D. Ponz, & S. Enrique, 112
- Bertin, E., & Arnouts, S. 1996, *AAPS*, 117, 393
- Bertin, E., Mellier, Y., Radovich, M., et al. 2002, in *Astronomical Society of the Pacific Conference Series*, Vol. 281, *Astronomical Data Analysis Software and Systems XI*, ed. D. A. Bohlender, D. Durand, & T. H. Handley, 228

- Bhatti, W. A., Richmond, M. W., Ford, H. C., & Petro, L. D. 2010, *ApJS*, 186, 233
- Bianchi, L., Herald, J., Efremova, B., et al. 2011, *APSS*, 335, 161
- Bond, J. R., Jaffe, A. H., & Knox, L. 1998, *PRD*, 57, 2117
- Boroson, T. A., & Lauer, T. R. 2009, *Nature*, 458, 53
- Bowen, D. B., Campanelli, M., Krolik, J. H., Mewes, V., & Noble, S. C. 2017, *ApJ*, 838, 42
- Bowen, D. B., Mewes, V., Campanelli, M., et al. 2018, *ApJL*, 853, L17
- Britzen, S., Fendt, C., Witzel, G., et al. 2018, *MNRAS*, 478, 3199
- Caplar, N., Lilly, S. J., & Trakhtenbrot, B. 2017, *ApJ*, 834, 111
- Cardelli, J. A., Clayton, G. C., & Mathis, J. S. 1989, *ApJ*, 345, 245
- Charisi, M., Bartos, I., Haiman, Z., et al. 2016, *MNRAS*, 463, 2145
- Charisi, M., Haiman, Z., Schiminovich, D., & D’Orazio, D. J. 2018, *MNRAS*, 476, 4617
- Chornock, R., Bloom, J. S., Cenko, S. B., et al. 2010, *ApJL*, 709, L39
- Comerford, J. M., Gerke, B. F., Stern, D., et al. 2012, *ApJ*, 753, 42
- Comerford, J. M., Griffith, R. L., Gerke, B. F., et al. 2009a, *ApJL*, 702, L82
- Comerford, J. M., Pooley, D., Barrows, R. S., et al. 2015, *ApJ*, 806, 219
- Comerford, J. M., Gerke, B. F., Newman, J. A., et al. 2009b, *ApJ*, 698, 956
- Cutri, R. M., & et al. 2013, *VizieR Online Data Catalog*, 2328
- d’Ascoli, S., Noble, S. C., Bowen, D. B., et al. 2018, *ArXiv e-prints*, arXiv:1806.05697
- Deane, R. P., Paragi, Z., Jarvis, M. J., et al. 2014, *Nature*, 511, 57
- Desvignes, G., Caballero, R. N., Lentati, L., et al. 2016, *MNRAS*, 458, 3341
- Detweiler, S. 1979, *ApJ*, 234, 1100
- D’Orazio, D. J., Haiman, Z., & MacFadyen, A. 2013, *MNRAS*, 436, 2997
- D’Orazio, D. J., Haiman, Z., & Schiminovich, D. 2015, *Nature*, 525, 351
- Dorn-Wallenstein, T., Levesque, E. M., & Ruan, J. J. 2017, *ApJ*, 850, 86
- Dotti, M., Montuori, C., Decarli, R., et al. 2009, *MNRAS*, 398, L73
- Drake, A. J., Djorgovski, S. G., Mahabal, A., et al. 2009, *ApJ*, 696, 870

- Edelson, R., Vaughan, S., Malkan, M., et al. 2014, *ApJ*, 795, 2
- Edwards, R. T., Hobbs, G. B., & Manchester, R. N. 2006, *MNRAS*, 372, 1549
- Eggers, D., Shaffer, D. B., & Weistrop, D. 2000, *AJ*, 119, 460
- Elvis, M., Wilkes, B. J., McDowell, J. C., et al. 1994, *ApJS*, 95, 1
- Eracleous, M., Boroson, T. A., Halpern, J. P., & Liu, J. 2012, *ApJS*, 201, 23
- Farris, B. D., Duffell, P., MacFadyen, A. I., & Haiman, Z. 2014, *ApJ*, 783, 134
- . 2015, *MNRAS*, 446, L36
- Ferrarese, L., & Ford, H. 2005, *SSR*, 116, 523
- Ferrarese, L., & Merritt, D. 2000, *ApJL*, 539, L9
- Foord, A., Gültekin, K., Reynolds, M., et al. 2017, *ApJ*, 851, 106
- Foreman-Mackey, D., Agol, E., Ambikasaran, S., & Angus, R. 2017, *AJ*, 154, 220
- Forster, K., Green, P. J., Aldcroft, T. L., et al. 2001, *ApJS*, 134, 35
- Foster, R. S., & Backer, D. C. 1990, *ApJ*, 361, 300
- Fried, J. W., & Schulz, H. 1983, *AAP*, 118, 166
- Fu, H., Yan, L., Myers, A. D., et al. 2012, *ApJ*, 745, 67
- Fu, H., Zhang, Z.-Y., Assef, R. J., et al. 2011, *ApJL*, 740, L44
- Garcia, A., Sodr , L., Jablonski, F. J., & Terlevich, R. J. 1999, *MNRAS*, 309, 803
- Gebhardt, K., Bender, R., Bower, G., et al. 2000, *ApJL*, 539, L13
- Gezari, S., Martin, D. C., Forster, K., et al. 2013, *ApJ*, 766, 60
- Gierliński, M., Middleton, M., Ward, M., & Done, C. 2008, *Nature*, 455, 369
- Gillespie, D. T. 1996, *American Journal of Physics*, 64, 225
- Gold, R., Paschalidis, V., Etienne, Z. B., Shapiro, S. L., & Pfeiffer, H. P. 2014, *PRD*, 89, 064060
- Goodman, J., & Weare, J. 2010, *Communications in Applied Mathematics and Computational Science*, Vol. 5, No. 1, p. 65-80, 2010, 5, 65
- Graham, A. W., Erwin, P., Caon, N., & Trujillo, I. 2001, *ApJL*, 563, L11
- Graham, M. J., Djorgovski, S. G., Stern, D., et al. 2015a, *Nature*, 518, 74
- . 2015b, *MNRAS*, 453, 1562

- Gültekin, K., Richstone, D. O., Gebhardt, K., et al. 2009, *ApJ*, 698, 198
- Haiman, Z., Kocsis, B., & Menou, K. 2009, *ApJ*, 700, 1952
- Heinis, S., Kumar, S., Gezari, S., et al. 2016a, *ApJ*, 821, 86
- Heinis, S., Gezari, S., Kumar, S., et al. 2016b, *ApJ*, 826, 62
- Hellings, R. W., & Downs, G. S. 1983, *ApJL*, 265, L39
- Hobbs, G. 2013, *Classical and Quantum Gravity*, 30, 224007
- Hobbs, G., Archibald, A., Arzoumanian, Z., et al. 2010, *Classical and Quantum Gravity*, 27, 084013
- Honeycutt, R. K. 1992, *PASP*, 104, 435
- Hopkins, P. F., Hernquist, L., Cox, T. J., et al. 2006, *ApJS*, 163, 1
- Horne, J. H., & Baliunas, S. L. 1986, *ApJ*, 302, 757
- Ivezic, Z., Tyson, J. A., Acosta, E., et al. 2008, *ArXiv e-prints*, arXiv:0805.2366
- Janssen, G., Hobbs, G., McLaughlin, M., et al. 2015, *Advancing Astrophysics with the Square Kilometre Array (AASKA14)*, 37
- Jenet, F. A., Lommen, A., Larson, S. L., & Wen, L. 2004, *ApJ*, 606, 799
- Jester, S., Schneider, D. P., Richards, G. T., et al. 2005, *AJ*, 130, 873
- Jun, H. D., Stern, D., Graham, M. J., et al. 2015, *ApJL*, 814, L12
- Kaiser, N., Burgett, W., Chambers, K., et al. 2010, in *Society of Photo-Optical Instrumentation Engineers (SPIE) Conference Series*, Vol. 7733, *Society of Photo-Optical Instrumentation Engineers (SPIE) Conference Series*, 77330E
- Kelly, B. C., Bechtold, J., & Siemiginowska, A. 2009, *ApJ*, 698, 895
- Kharb, P., Lal, D. V., & Merritt, D. 2017, *Nature Astronomy*, 1, 727
- Kochanek, C. S., Shappee, B. J., Stanek, K. Z., et al. 2017, *PASP*, 129, 104502
- Kocsis, B., Haiman, Z., & Loeb, A. 2012, *MNRAS*, 427, 2680
- Komossa, S., Burwitz, V., Hasinger, G., et al. 2003, *ApJL*, 582, L15
- Kormendy, J., & Ho, L. C. 2013, *ARAA*, 51, 511
- Kormendy, J., & Richstone, D. 1995, *ARAA*, 33, 581
- Koss, M., Mushotzky, R., Treister, E., et al. 2011, *ApJL*, 735, L42
- Kovacs, G. 1981, *APSS*, 78, 175

- Kovačević, A. B., Pérez-Hernández, E., Popović, L. Č., et al. 2018, *MNRAS*, 475, 2051
- Kozłowski, S. 2016, *MNRAS*, 459, 2787
- Kozłowski, S., Kochanek, C. S., Udalski, A., et al. 2010, *ApJ*, 708, 927
- Kramer, M., & Champion, D. J. 2013, *Classical and Quantum Gravity*, 30, 224009
- Kun, E., Frey, S., Gabányi, K. É., et al. 2015, *MNRAS*, 454, 1290
- Law, N. M., Kulkarni, S. R., Dekany, R. G., et al. 2009, *PASP*, 121, 1395
- Lehto, H. J., & Valtonen, M. J. 1996, *ApJ*, 460, 207
- Lentati, L., Taylor, S. R., Mingarelli, C. M. F., et al. 2015, *MNRAS*, 453, 2576
- Liu, T., Gezari, S., & Miller, M. C. 2018, *ApJL*, 859, L12
- Liu, T., Gezari, S., Heinis, S., et al. 2015, *ApJL*, 803, L16
- Liu, T., Gezari, S., Burgett, W., et al. 2016, *ApJ*, 833, 6
- Liu, X., Shen, Y., Strauss, M. A., & Greene, J. E. 2010, *ApJ*, 708, 427
- Lobanov, A. P., & Roland, J. 2005, *A&A*, 431, 831
- Lomb, N. R. 1976, *APSS*, 39, 447
- Lu, J.-F., & Zhou, B.-Y. 2005, *ApJL*, 635, L17
- MacFadyen, A. I., & Milosavljević, M. 2008, *ApJ*, 672, 83
- MacLeod, C. L., Ivezić, Ž., Kochanek, C. S., et al. 2010, *ApJ*, 721, 1014
- Magnier, E. 2006, in *The Advanced Maui Optical and Space Surveillance Technologies Conference*, E50
- Magnier, E. A., Schlafly, E., Finkbeiner, D., et al. 2013, *ApJS*, 205, 20
- Magorrian, J., Tremaine, S., Richstone, D., et al. 1998, *AJ*, 115, 2285
- Maness, H. L., Taylor, G. B., Zavala, R. T., Peck, A. B., & Pollack, L. K. 2004, *ApJ*, 602, 123
- Martini, P. 2004, *Coevolution of Black Holes and Galaxies*, 169
- Matthews, T. A., & Sandage, A. R. 1963, *ApJ*, 138, 30
- McConnell, N. J., & Ma, C.-P. 2013, *ApJ*, 764, 184
- McHardy, I. 2010, *The Jet Paradigm: From Microquasars to Quasars*, ed. T. Belloni (Berlin, Heidelberg: Springer Berlin Heidelberg), 203–232

- McLaughlin, M. A. 2013, *Classical and Quantum Gravity*, 30, 224008
- McLure, R. J., & Dunlop, J. S. 2004, *MNRAS*, 352, 1390
- McLure, R. J., & Jarvis, M. J. 2002, *MNRAS*, 337, 109
- Miller, L., Turner, T. J., Reeves, J. N., et al. 2010, *MNRAS*, 403, 196
- Milosavljević, M., & Merritt, D. 2003, in *American Institute of Physics Conference Series*, Vol. 686, *The Astrophysics of Gravitational Wave Sources*, ed. J. M. Centrella, 201–210
- Moore, C. J., Taylor, S. R., & Gair, J. R. 2015, *Classical and Quantum Gravity*, 32, 055004
- Morganson, E., Burgett, W. S., Chambers, K. C., et al. 2014, *ApJ*, 784, 92
- Mushotzky, R. F., Edelson, R., Baumgartner, W., & Gandhi, P. 2011, *ApJL*, 743, L12
- Noble, S. C., Mundim, B. C., Nakano, H., et al. 2012, *ApJ*, 755, 51
- Oh, K., Koss, M., Markwardt, C. B., et al. 2018, *ApJS*, 235, 4
- Padmanabhan, N., Schlegel, D. J., Finkbeiner, D. P., et al. 2008, *ApJ*, 674, 1217
- Peng, C. Y., Impey, C. D., Ho, L. C., Barton, E. J., & Rix, H.-W. 2006, *ApJ*, 640, 114
- Perera, B. B. P., Stappers, B. W., Babak, S., et al. 2018, *MNRAS*, arXiv:1804.10571
- Peters, P. C. 1964, *Physical Review*, 136, 1224
- Peterson, B. M. 2001, in *Advanced Lectures on the Starburst-AGN*, ed. I. Aretxaga, D. Kunth, & R. Mújica, 3
- Pihajoki, P. 2016, *MNRAS*, 457, 1145
- Pojmanski, G. 1997, *ACTAA*, 47, 467
- Press, W. H. 1978, *Comments on Astrophysics*, 7, 103
- Reardon, D. J., Hobbs, G., Coles, W., et al. 2016, *MNRAS*, 455, 1751
- Richards, G. T., Fan, X., Newberg, H. J., et al. 2002, *AJ*, 123, 2945
- Richards, G. T., Lacy, M., Storrie-Lombardi, L. J., et al. 2006a, *ApJS*, 166, 470
- Richards, G. T., Strauss, M. A., Fan, X., et al. 2006b, *AJ*, 131, 2766
- Rodriguez, C., Taylor, G. B., Zavala, R. T., et al. 2006, *ApJ*, 646, 49

- Roedig, C., Krolik, J. H., & Miller, M. C. 2014, *ApJ*, 785, 115
- Rosado, P. A., Sesana, A., & Gair, J. 2015, *MNRAS*, 451, 2417
- Ross, N. P., McGreer, I. D., White, M., et al. 2013, *ApJ*, 773, 14
- Runnoe, J. C., Eracleous, M., Mathes, G., et al. 2015, *ApJS*, 221, 7
- Runnoe, J. C., Eracleous, M., Pennell, A., et al. 2017, *MNRAS*, 468, 1683
- Sazhin, M. V. 1978, *Sov. Ast.*, 22, 36
- Scargle, J. D. 1982, *ApJ*, 263, 835
- Schlaafly, E. F., & Finkbeiner, D. P. 2011, *ApJ*, 737, 103
- Schlaafly, E. F., Finkbeiner, D. P., Jurić, M., et al. 2012, *ApJ*, 756, 158
- Schmidt, K. B., Marshall, P. J., Rix, H.-W., et al. 2010, *ApJ*, 714, 1194
- Sesana, A., Haiman, Z., Kocsis, B., & Kelley, L. Z. 2017, *ArXiv e-prints*, arXiv:1703.10611
- Sesana, A., Vecchio, A., & Volonteri, M. 2009, *MNRAS*, 394, 2255
- Sesar, B., Stuart, J. S., Ivezić, Ž., et al. 2011, *AJ*, 142, 190
- Sesar, B., Ivezić, Ž., Lupton, R. H., et al. 2007, *AJ*, 134, 2236
- Severgnini, P., Cicone, C., Della Ceca, R., et al. 2018, *MNRAS*, arXiv:1806.10150
- Shannon, R. M., Ravi, V., Lentati, L. T., et al. 2015, *Science*, 349, 1522
- Shappee, B. J., Prieto, J. L., Grupe, D., et al. 2014, *ApJ*, 788, 48
- Shen, Y., Greene, J. E., Strauss, M. A., Richards, G. T., & Schneider, D. P. 2008, *ApJ*, 680, 169
- Shen, Y., & Loeb, A. 2010, *ApJ*, 725, 249
- Shi, J.-M., & Krolik, J. H. 2015, *ApJ*, 807, 131
- Shi, J.-M., Krolik, J. H., Lubow, S. H., & Hawley, J. F. 2012, *ApJ*, 749, 118
- Sillanpaa, A., Haarala, S., Valtonen, M. J., Sundelius, B., & Byrd, G. G. 1988, *ApJ*, 325, 628
- Simm, T., Salvato, M., Saglia, R., et al. 2016, *AAP*, 585, A129
- Smith, K. L., Mushotzky, R. F., Boyd, P. T., et al. 2018a, *ArXiv e-prints*, arXiv:1803.06436

- Smith, K. L., Mushotzky, R. F., Boyd, P. T., & Wagoner, R. V. 2018b, *ApJL*, 860, L10
- Smith, K. L., Shields, G. A., Bonning, E. W., et al. 2010, *ApJ*, 716, 866
- Snodgrass, C., & Carry, B. 2013, *The Messenger*, 152, 14
- Springel, V., White, S. D. M., Jenkins, A., et al. 2005, *Nature*, 435, 629
- Sudou, H., Iguchi, S., Murata, Y., & Taniguchi, Y. 2003, *Science*, 300, 1263
- Tang, Y., Haiman, Z., & MacFadyen, A. 2018, *MNRAS*, 476, 2249
- Tang, Y., MacFadyen, A., & Haiman, Z. 2017, *MNRAS*, 469, 4258
- The NANOGrav Collaboration, Arzoumanian, Z., Brazier, A., et al. 2015, *ApJ*, 813, 65
- Timmer, J., & Koenig, M. 1995, *AAP*, 300, 707
- Tonry, J. L., Stubbs, C. W., Kilic, M., et al. 2012a, *ApJ*, 745, 42
- Tonry, J. L., Stubbs, C. W., Lykke, K. R., et al. 2012b, *ApJ*, 750, 99
- Ulrich, M.-H., Maraschi, L., & Urry, C. M. 1997, *ARAA*, 35, 445
- Valtonen, M. J., Lehto, H. J., Takalo, L. O., & Sillanpää, A. 2011, *ApJ*, 729, 33
- Valtonen, M. J., Lehto, H. J., Nilsson, K., et al. 2008, *Nature*, 452, 851
- Valtonen, M. J., Zola, S., Ciprini, S., et al. 2016, *ApJL*, 819, L37
- Vanden Berk, D. E., Richards, G. T., Bauer, A., et al. 2001, *AJ*, 122, 549
- Vanden Berk, D. E., Wilhite, B. C., Kron, R. G., et al. 2004, *ApJ*, 601, 692
- Vasiliev, E., Antonini, F., & Merritt, D. 2015, *ApJ*, 810, 49
- Vaughan, S., & Uttley, P. 2006, *Advances in Space Research*, 38, 1405
- Vaughan, S., Uttley, P., Markowitz, A. G., et al. 2016, *MNRAS*, 461, 3145
- Vestergaard, M., & Peterson, B. M. 2006, *ApJ*, 641, 689
- Vestergaard, M., & Wilkes, B. J. 2001, *ApJS*, 134, 1
- Volonteri, M., Haardt, F., & Madau, P. 2003, *ApJ*, 582, 559
- Volonteri, M., Miller, J. M., & Dotti, M. 2009, *ApJL*, 703, L86
- Wang, J.-M., Chen, Y.-M., Hu, C., et al. 2009, *ApJL*, 705, L76
- White, R. L., Becker, R. H., Helfand, D. J., & Gregg, M. D. 1997, *ApJ*, 475, 479

- White, S. D. M., & Rees, M. J. 1978, MNRAS, 183, 341
- Wright, E. L. 2006, PASP, 118, 1711
- York, D. G., Adelman, J., Anderson, Jr., J. E., et al. 2000, AJ, 120, 1579
- Zheng, Z.-Y., Butler, N. R., Shen, Y., et al. 2016, ApJ, 827, 56
- Zhu, X.-J., Hobbs, G., Wen, L., et al. 2014, MNRAS, 444, 3709
- Zoghbi, A., Reynolds, C., & Cackett, E. M. 2013, ApJ, 777, 24